THÈSE POUR OBTENIR LE GRADE DE DOCTEUR DE MONTPELLIER SUPAGRO

En Génie des Procédés

École doctorale GAIA – Biodiversité, Agriculture, Alimentation, Environnement, Terre, Eau

Unité de recherche : Laboratoire de Biotechnologie et de l'Environnement, INRAE Narbonne

Exploring minimum conditions allowing the development of oxygenic photogranules

Exploration des conditions minimales permettant la formation de photogranules

présentée par Esmee Desirée JOOSTEN
le 18 mars 2021

Sous la direction de Jérôme HAMELIN

et Kim MILFERSTEDT

Devant le jury composé de

Jean-François HUMBERT, DR, Sorbonne Université, iEES Paris	*Rapporteur*
Tania FERNANDES, CR, Netherlands Institute of Ecology, Wageningen, Pays-Bas	*Rapportrice*
Raeid ABED, Professeur, Sultan Qaboos University, Muscat, Oman	*Examinateur*
Muriel GUGGER, CR, Institut Pasteur, Paris	*Examinatrice*
Thierry RUIZ, Professeur, Université de Montpellier	*Président du jury*
Jérôme HAMELIN, DR, INRAE Occitanie-Montpellier	*Directeur de thèse*
Kim MILFERSTEDT, CR, INRAE Occitanie-Montpellier	*Co-encadrant*

UNIVERSITÉ DE MONTPELLIER

Montpellier SupAgro

Acknowledgements

I could not have written my dissertation without the support and love of many people. I am grateful to all of you for your help and inspiration and the beautiful moments that we shared together during this journey. Your activities and involvement that led to this result mean more to me than I could ever express here in words.

Kim and Jérôme, thank you for believing in me starting this adventure together. Thank you that I could always run into your offices when I needed help, thank you for sharing your knowledge with me and for the interesting discussions we had. Thank you for your efforts challenging me and supporting me into becoming an independent researcher. **Kim**, thank your curiosity-driven questions, for your advices regarding experimental setups, data processing and manuscripts, for keeping track of my progress and stimulating activities that let me grow, for always being on the lookout for programs and tools that made your life easier, and therewith mine, for your creativity and illustrator skills, for your hospitality, enthusiasm and jokes. **Jérôme**, thank you for sharing your broad knowledge on microbial ecosystems, for your critical questions that pushed me to put my work into perspective, for challenging me to discuss science in French, for helping out with administrative and language-related issues, for keeping calm when I got stressed, for your interest in my family matter, for your thoughtfulness and celebrating my first first-author paper with a personal mug that reminds me of the good times I had in the photogranule team.

Hicham, my partner in crime. We started this adventure together, you mostly modelling, me experiments, super motivated to join forces to unravel the photogranulation phenomenon. And here we are, three years later, close to the end of our PhD projects. Our work resulted maybe in more questions than answers, but what a great time we had. I am glad I had you by my side along this journey. Thank you for always having my back, for taking time to discuss science, for helping out with experimental measurements, IT or administrative issues, for your hunt to articles and our fun chats and activities. It is my first week without you in the lab and I already miss you.

Anaïs, merci d'avoir toujours été là pour moi. Technicienne, collègue de bureau, traductrice et amie: tout en un! Une vraie star! Merci pour ton aide dans les incubations hydrostatiques et les méthodes de biologie moléculaire, pour avoir partagé ton bureau avec moi, pour avoir pris des cours d'anglais (et un peu de néerlandais), pour avoir amélioré mon français, et pour avoir vérifié beaucoup de mes courriers et documents écrits en français. Mais surtout: merci pour tous les beaux moments que nous avons partagés ensemble, où j'ai pu t'épancher mon cœur, toutes les fois où nous avons parlé et ri. Merci d'être ma meilleure amie! Je me suis éclatée et ça va me manquer. Je suis heureuse de t'avoir rencontrée.

Raffaello, thanks for your cheerfulness. Thanks to you, I was no longer working alone in the photogranule room and did I have someone to discuss my observations with. Thank you for your commitment and motivation to contribute to my PhD project. Thank you for being my friend.

Elie and **Nicolas**, thank you for your input and advice. **Chul** and **Ahmed** thank you for the collaboration and scientific discussions. **Thierry,** thank you for your interesting questions, enthusiasm and for making me feel like I could do it. **Dinithi, Valentin, Karina, Anissa, Hando** and **Mokwon**, thank you for sharing your fresh ideas on photogranulation. **Robert,** bedankt voor het bestellen van de cyanobacteriële stam die de start van het omslagpunt in mijn PhD markeert en voor onze wetenschappelijk discussies. **Charlotte** et **Sahima**, je vous remercie de m'avoir

enseigné et aidé à isoler les cyanobactéries des photogranules. Je suis reconnaissante d'avoir pu vous rencontrer et d'avoir eu l'occasion d'obtenir des souches de mes propres photogranules. **Elisabeth** et **Claire-Emmanuelle**, je vous remercie de votre collaboration, de vos efforts et du temps que vous avez consacré à guider Raffaello et à modifier votre protocole d'extraction de l'EPS selon nos souhaits. **Claire**, merci d'avoir réalisé les nombreuses réactions de qPCR. **ED GAIA** et **ANR**, je vous remercie d'avoir rendu mon projet financièrement possible.

Je suis reconnaissante d'avoir eu l'opportunité de faire mon doctorat dans un laboratoire avec tant de personnes merveilleuses qui sont motivées pour s'entraider. Le début de mon doctorat n'a pas toujours été facile étant donné mon mauvais français. Je suis reconnaissante à tous ceux qui m'ont aidé à traduire et à intégrer. Je suis heureuse d'avoir fait partie de la famille LBE et je tiens à remercier tous ceux qui ont rendu mon projet et ma vie meilleurs.

Gaëlle, merci d'avoir rendu possible les nombreuses réactions de qPCR, **Philippe**, merci d'avoir expliqué les protocoles et équipements analytiques, les dépannages et nos discussions, **Guillaume**, merci d'avoir construit une grille pour positionner les flacons sur le scanner, **Dennis**, merci d'avoir installé une minuterie pour régler la lumière et d'avoir commandé des produits chimiques, **Valérie**, **Annie**, **Nadine**, merci d'avoir commandé des consommables et des produits de laboratoire plus exotiques, **Sylvie**, merci d'avoir validé mes heures de travail et surtout, de m'avoir trouvé un appartement, **Alexandra**, merci d'avoir validé et organisé mes déplacements aux conférences.

I also would like to thank those of you that enriched my life outside the walls of the lab. Thank you for all the beautiful moments we shared together. For the times we spent drinking beers at l'Echoppe, eating tapas at Centaurée, barbecuing at home, picnicking and playing volleyball on the beach, hiking and mushroom hunting in the forest, skiing and sledding in the snow, and everything else.

Ahmed, thank you for being my neighbor and best friend when I arrived in Narbonne and for making me feel directly at home, **Noémie**, for taking care of me and organizing presents and activities for everyone, **Lucia,** for your smile and dance moves, **Pablo**, for your worldwide knowledge and for always having veggies on the BBQ, **Farouk**, for your heartwarming kindness, **Julien**, for being team phototrophs en voor je gezelligheid en die van **Romain**, **Julie,** for bridging the language gap and involving me right from the start, **Clément**, for your crazy jokes and organizing skills, **Yolanda,** for being the sweetest person, **Felipe,** for your amazing stories, thank you both for your hospitality, **Roland**, for always being interested in how I am doing, **Marie**, for translating for me during your internship, and for your funny forward rolls, **Virginie**, for not being afraid to share your feelings, **Kévin** for your phyloseq discoveries, **Florian,** for involving me from even before my PhD, taking me to the fête de la musique, **Kévin** for our many talks at lunch, **Céline** for your patience with my French and enthusiasm, **Alexandre,** for your cheerfulness, **Kévin,** for your own kind of magic, **Morand**, for your funny stories and parties at "la coloc", **Gaetano,** for your research interest and wild research suggestions, **Fernanda**, for you radiating calmness, **Lucie**, for our hikes, **Noémie,** for our cross country skiing adventures. And to all who have come and gone, or have just arrived, and enriched my life.

Cynthia, merci de m'avoir appris la langue française et les habitudes françaises. J'ai souvent été heureuse que vous m'avez appris à des choses que je ne pensais pas utiliser, mais qui semblaient très utiles. Merci aussi d'avoir organisé des activités pour nous, c'était génial!

Dominique et **Jean-Marc**, merci de m'avoir loué votre appartement. Ce fut un plaisir de vivre dans votre propriété. Qui était censé être mon refuge pour un seul mois, est devenu ma maison pendant toute la durée de mon doctorat. Vous étiez toujours là pour moi quand j'avais besoin d'aide. Merci pour votre hospitalité et votre gentillesse, pour m'avoir donné une famille ici.

I would like to thank my friends and family back home for their love and for always having my back.

Nina, Lory, Sharina, Leanne, Fleur, Milan, Ingrid, Linda, Agnita, Xavier, Els, **Loes, Maureen, Danny, Maaike, Tom, Oscar, Laura, Eleonoor,** het is een feestje met jullie in mijn leven! Videobellen, quizen, teken challenges, theeleuten, zangwedstijden, en wat al niet meer. Bedankt. Bedankt ook voor jullie bezoekjes aan het koude en regenachtige Narbonne, **Nina**, en het hete en droge Narbonne, **Leanne**, en voor het slaapfeestje tijdens de conferentie in Delft. Dankjewel **Agnita** voor onze gezellige dagen in Barcelona.

Tom, dankjewel voor je liefde en steun om mij dit avontuur aan te laten gaan. Het was niet altijd makkelijk, maar we hebben het gedaan! Dankjewel voor je maandelijkse bezoekjes aan Narbonne, voor de leuke uitstapjes die we hebben gemaakt, voor het luisteren naar mijn gebrabbel over cyanobacteriën als ik mijn gedachten moest ordenen, dank ook voor je creatieve verhalen over de avonturen van de cyanobacteriën, dankjewel dat je het drie jaar lang volgehouden hebt met mij op afstand. Nu weer snel samenwonen! Je bent de leukste en de liefste. Ik ben heel erg blij met jou!

Koen, Tineke, Cor, bedankt voor jullie steun en voor jullie gezelligheid als ik thuis was. **Birgitta,** bedankt voor je liefde en interesse. Ook dank aan alle familieleden die mij hebben gesteund.

Jolanda en **Jan-Piet**. Dankjulliewel voor jullie onvoorwaardelijk liefde. Bedankt dat jullie er altijd voor me zijn en dat ik jullie altijd kan bellen, of ik nou blij of verdrietig ben. Bedankt dat jullie me de vrijheid geven om mijn dromen achterna te jagen, ookal komen die niet overeen met jullie droom om mij in de buurt te hebben. Ik ben dankbaar en gelukkig met ons gezin, en dat ik jullie dochter ben. Ik heb erg genoten van de moment dat we samen waren, jullie hier en ik daar. Liefste mamsie, ik ben harstikke trots op jouw kracht en doorzettingsvermogen. Lieve papsie, ik bewonder jou om hoe hard je werkt en hoe je alles voor ons over hebt. Liefste mamsie en papsie, jullie zijn mijn helden.

Mijn grote, kleine zusje **Jasmijn**. Dankjewel dat je zo lief en zorgzaam bent, schattig en grappig (ookal vind je zelf van niet). Ik bewonder hoeveel liefde jij kunt geven en hoe jij je inzet voor anderen. Ik ben trots op hoe jij je leven hebt ingericht en wat een knappe dochter Sjors en jij hebben. Ik ben heel blij dat ik Jipps tante ben. **Sjors**, dankjewel voor je bezoek aan Narbonne, je grappige verhalen en gezellige etentjes als ik een weekendje thuis was.

Contents

List of figures

List of tables

Summary

Photogranules are found in a variety of environments, including glacier surfaces, marine tidal waters, tropical lagoons and sulfide-rich hot springs. Recently, it was demonstrated that similar structures in the laboratory can be produced from activated sludge used in wastewater treatment. When transferred to a vial, this sludge transforms into a roughly spherical aggregate over the course of several weeks. Photogranules with a similar morphology can be produced in bioreactors. Their syntrophic community and their high settleability make photogranules interesting candidates for biotechnological application. Meanwhile, it has already been demonstrated that photogranules can efficiently treat wastewater without external aeration. The produced photogranular biomass is rich in biopolymers and may be valorized, turning wastewater into a resource. Biological and ecological principles of photogranulation, i.e., how microbial communities assemble and self-organize into a spherical ecosystem, are currently unknown, but may advance potential biotechnological applications.

For the optimal application of photogranules in biotechnological processes, it desirable to have a good understanding of what factors drive photogranulation. Contrary to aerobic and anaerobic granules, photogranules do not need hydrodynamic shear force and washout for their development, because they can also form in the absence of these factors that are commonly postulated as driving forces for granulation. We therefore believe that photogranulation results from an intrinsic property of the ecosystem, i.e., the microbial community. Because it is difficult to monitor the development of individual photogranules in a turbulently mixed bioreactor, we study the temporal and spatial development of photogranules in hydrostatic batch cultivations. In these closed vials, the activated sludge inoculum and incoming light are the resources from which the photogranules are ultimately produced. Initially low abundant filamentous cyanobacteria are enriched with the development of the spherical structure, along with an increase in extracellular polymeric substances (EPS).

The aim of my thesis is to find out what is minimally needed in the complex activated sludge matrix to produce a photogranule. By studying the literature, I learnt that naturally occurring photogranules have a photoactive surface layer. Cryoconite granules on glacier surfaces, modern microbialites in tidal waters and tropical lagoons, and clumps in hot springs all appear to result from the gliding and entanglement of filamentous cyanobacteria, that are embedded in an auto-produced matrix of EPS and trap and bind organic matter and mineral particles. Gliding filamentous cyanobacteria are also highly abundant in outer layers of photogranules produced from activated sludge. Non-phototrophic bacteria are present on the cyanobacterial trichomes and most abundant in the interior. Their role in photogranulation has not yet been elucidated. I hypothesize that gliding filamentous cyanobacteria can self-aggregate to form photogranules under defined physicochemical conditions.

My initial objectives evolved during my thesis. I ended up having the following three main objectives aimed at better understanding the minimum (microbial) requirements for photogranulation: i) develop a high-throughput time-lapse imaging assay, ii) elucidate the relationship between microbial community structure and ecosystem spatial organization, and iii) asses how the spatial self-organization of the ecosystem is affected by cyanobacterial augmentations of the initial activated sludge.

I developed a high-throughput time-lapse imaging tool to capture the temporal development of photogranules in terms of biomass contraction seen through the bottom of a vial (**Chapter 3**). This allowed me to systematically test how a modification of the initial conditions affected the onset and speed of contraction and the final photogranule diameter. Having a standardized method, I could measure contraction in a large number of vials simultaneously and compare results between cultivation sets and experimental conditions.

While photogranulation was demonstrated for different sludge sources worldwide and appeared to be a robust phenomenon when I started my PhD, it became apparent that a distribution of spatial structures could be produced from the same activated sludge inoculum. To find out if the spatial organization of the ecosystem depends on the underlying microbial community, I compared final community structures between five distinct final morphotypes produced in twenty-six cultivation sets over a period of three years (**Chapter 4**). Differences in community structure between morphotypes may indicate key players in the formation of the respective spatial structures. Cyanobacterial growth was needed to form a coherent structure. Spatialization increased with increasing cyanobacterial to algal abundance and increasing number of bacterial OTUs. Contrary to what I expected, morphotypes could not be discriminated by their final community structures. Spatialization must therefore depend on earlier events, e.g., cyanobacterial succession. Final cyanobacterial communities may have converged across different morphotypes because of a high selection pressure, e.g., constant high light intensity. Most abundant microbes in the final morphotypes were the Subsection III cyanobacteria *Tychonema* and *Planktothrix*, the alga Chlorella, and the non-phototrophic bacteria *Hydrogenophaga*, *Luteimonas*, *Porphyrobacter* and *Sediminibacterium*.

Despite not detecting a difference in the final communities, I expected that a difference in the cyanobacterial communities had led to the different spatial structures. I hypothesized that I could increase the number of photogranules produced per cultivation set by augmenting the initial activated sludge with cyanobacteria from photogranules (**Chapter 5**). This was based on the assumption that cyanobacteria in the outer layer of a mature photogranule possess the trait to form the spherical photogranule structure. With the help and training of Charlotte Duval and Sahima Hamlaoui of the group of Cécile Bernard at the Muséum National d'Histoire Naturelle (Paris, France), I isolated gliding filamentous cyanobacteria from mature photogranules. Sufficiently large cyanobacterial augmentations steered morphotype development into the direction of the morphotype formed by the added strain. Photogranule-forming strains *Oscillatoria* and *Kamptonema* marked the final morphotype, but not the final community structure because they were outcompeted by mat-forming strains, i.e., *Tychonema*. The observed photogranule-forming strains are phylogenetically closer to each other than the mat-forming strains. Only a limited number of the isolated strains steered photogranulation which suggests that the ability to photogranule is not shared by all Subsection III members and not an as widespread phenomenon as initially believed.

With my thesis, I bridged the research fields of microbial ecology and process engineering. Photogranulation in semi-stagnant environments was known in nature, but never applied in biotechnology. A photogranule-forming cyanobacterium in a synthetic medium is the minimum requirement for photogranulation. Even though formation of photogranules by cyanobacterial strains is nothing new to scientists working with cyanobacteria, their potential in photogranule microbiomes for biotechnology has not been valued before. Formation of a photogranule from a single cyanobacterial strain gives opportunity to ecological engineering. For example,

photogranule-forming strains can serve as an eco-chassis to which ecosystem functions can be added. Hydrostatic photogranulation can be used as a model system to study spatialization using a xenic cyanobacterial strain in synthetic medium. This can provide insight into the trait responsible for spatial structure formation and the role of heterotrophic bacteria that are associated with cyanobacterial filaments. The photogranule ecosystem may furthermore be used to test ecological concepts, e.g., the role of an ecosystem engineer. Our model ecosystem is able to generate data at the microscale, e.g., from microelectrodes and microscopy, enabling us to further explore the development of spatial structures using mathematical modeling. Spatialization is an important but often disregarded feature of many microbial ecosystems. Continuum spatial models to compute physicochemical gradients, paired with individual based models capturing the behavior of gliding filamentous cyanobacteria, will provide insights in the assembly of this phototrophic ecosystem and consequences for ecosystem function.

Résumé etendu

Introduction

La photogranulation est un phénomène microbien qui aboutit à un agrégat phototrophe plus ou moins sphérique de plusieurs millimètres. Les photogranules contiennent une couche externe dense et photoactive qui ressemble à un tapis microbien, avec une géométrie très particulière. Ces agrégats ont été observés dans plusieurs habitats naturels : cryoconites à la surface des glaciers, microbialites dans les milieux océaniques et lagunes tropicales. Les principes biologiques et écologiques de la photogranulation peuvent être appliqués en biotechnologie pour orienter la fonction des écosystèmes vers des propriétés intéressantes, tels que le traitement des eaux usées sans apport externe d'oxygène, du fait de la propriété photosynthétique et de la bonne décantabilité des photogranules.

Les photogranules peuvent être produits en conditions de laboratoire en cultures batch non agitées ou en réacteur sous agitation. Pour les cultures batch, de la boue activée provenant d'un bassin d'aération d'une station d'épuration des eaux usées est incubée dans un tube clôt en présence de lumière. En quelques semaines, la boue activée se transforme en un photogranule. La communauté microbienne principalement hétérotrophe se transforme en communauté syntrophique avec la dominance d'au moins une cyanobactérie filamenteuse mobile appartenant à la Subsection III (selon Castenholz et al.'s dans Bergey's Manual of Systematics of Archaea and Bacteria) et des bactéries hétérotrophes. Les facteurs nécessaires à la mise en place de cet assemblage microbien et au développement d'une structure sphérique sont inconnus. Lors de ce travail de thèse, j'ai exploré les conditions minimales permettant le développement de photogranules avec un regard d'écologue microbien.

J'ai fait l'hypothèse que les cyanobactérie filamenteuses mobiles pouvaient s'auto-agréger sous forme de photogranules lorsqu'elles étaient placées dans des conditions physico-chimiques définies. J'ai simplifié la matrice de boue activée jusqu'à obtenir les ingrédients minimaux nécessaires à la formation de photogranules, par exemple en modifiant la taille des flocs de la boue activée, la disponibilité en nutriments, ou l'élimination d'un type de microorganismes de la communauté microbienne initiale. Mon premier objectif a été de développer un système haut débit d'imagerie pour quantifier la dynamique de la photogranulation and de comparer plusieurs séries de cultures (**Chapter 3**).

J'ai observé cependant que des réplicas ne formaient pas toujours des photogranules. Une diversité de morphotypes pouvait se former à partir d'une même boue activée dans des conditions expérimentales très standardisées. La boue pouvait rester floculée, compactée pour former un tapis microbien, partiellement contractée pour former un hémisphère, ou bien former un photogranule non cohésif qui se désagrège après agitation. Un tapis couvre l'entière surface du fond du tube, un hémisphère couvre moins le fond du tube et possède une surface bombée, un photogranule ressemble à une sphère et a une plus petite surface de contact avec le fond du tube que le diamètre de l'agrégat. Un photogranule résiste à une agitation forte.

J'ai fait l'hypothèse que les différences morphologiques se retrouvaient à l'échelle de la communauté microbienne, en particulier la présence et l'abondance de cyanobactéries filamenteuses mobiles. Une boue activée contient typiquement des traces de cyanobactéries, qui sont réparties de façon hétérogènes. Ces microorganismes rares peuvent être enrichis

initialement afin de favoriser le processus écologique de photogranulation, induisant la formation de différents morphotypes de l'écosystème. Ceci a amené mon second objectif de thèse : l'identification des espèces microbiennes clés dans le processus de photogranulation en étudiant les différences dans les communautés microbiennes pour des morphotypes distincts (**Chapter 4**).

Mon troisième objectif était d'augmenter le taux de succès de la photogranulation par bioaugmentation avec des suspensions enrichies en cyanobactéries d'intérêt (**Chapter 5**). Les sous-objectifs étaient (i) d'isoler des cyanobactéries filamenteuses mobiles à partir de photogranules matures et (ii) de vérifier la capacité de ses souches à former des photogranules en milieu synthétique ou améliorer la photogranulation d'une boue activée.

Mes questions de recherche initiales sur les conditions minimales permettant le développement de photogranules étaient très ambitieuses (rôle de la matrice, des conditions physico-chimique et des microorganismes), et ont été réévaluées pour m'intéresser uniquement au rôle des cyanobactéries filamenteuses mobiles.

Simple time-lapse imaging for quantifying the hydrostatic production of oxygenic photogranules (**Chapter 3**)

J'ai développé un dispositif d'imagerie séquentiel multiplexé permettant de quantifier la dynamique de formation des photogranules en batch non agités et de comparer les résultats de plusieurs séries d'expériences. Il est par exemple possible de tester plusieurs inoculums ou plusieurs conditions opératoires en parallèle. L'évolution de la réaction est quantifiée par la mesure de la contraction de la biomasse, la réduction du diamètre occupé par la biomasse au fond du tube au cours du temps. Des tubes clôts inoculés avec de la boue activée ont été éclairés et placés sur un scanner programmé pour collecter des images à intervalles réguliers. Des scripts dédiés pour ImageJ et R ont permis de calculer les diamètres et représenter leur évolution au cours du temps. Une réduction de moitié est typiquement attendue pour un photogranule. Le taux de succès est variable selon les expériences et peut dépendre de l'inoculum ou des conditions expérimentales (température, intensité de lumière, etc.). Cette variabilité est encore inexpliquée et fait l'objet de recherche en utilisant le protocole développé ici.

Cyanobacterial climax populations converge independent of ecosystem morphology (**Chapter 4**)

Les microorganismes s'organisent souvent en biofilms, représentant des communautés attachées à un substrat grâce à la production de substances polymériques extracellulaires (EPS) servant de colle. La matrice d'EPS forme une structure spatiale tridimensionnelle dans laquelle les cellules interagissent (quorum sensing, échange de métabolites). La proximité des cellules est un facteur de succès des interactions. Le réseau d'interactions microbiennes est donc tributaire de l'organisation spatiale, bien que cette propriété soit sous-étudiée en écologie microbienne.

En utilisant le dispositif multiplexé de photogranulation développé au cours de cette thèse (chapitre 3), une diversité de morphotypes peut être produite à partir d'une même boue activée incubée dans les mêmes conditions environnementales. J'ai profité de cette observation pour tester si on retrouvait bien une relation entre la structure de la communauté microbienne finale et le morphotype. Notamment, des différences infimes dans la distribution initiale des cyanobactéries pourrait induire des trajectoires fondamentalement différentes en termes de structures spatiales, et aboutir au final à des morphotypes distincts.

Durant ces trois ans, 21 séries de cultures ont été inoculées avec des boues activées de Narbonne et Ornaisons (village avoisinant). Pour chaque tube, le morphotype formé a été noté : biomasse floculée, tapis microbien, hémisphère, photogranule non cohésif, photogranule. Il n'a jamais été observé de transition d'un morphotype à un autre, une fois l'écosystème phototrophe installé. Les communautés microbiennes ont été analysées par PCR quantitative et séquençage des gènes d'ARN ribosomiques 16S et 23S pour 14 boues activées initiales et 186 morphotypes obtenus après incubation. Les analyses bioinformatiques ont été réalisées avec Mothur et R (phyloseq, vegan).

La transition d'un écosystème typiquement hétérotrophe (boue activée) à un écosystème syntrophique basé sur l'activité phototrophe (morphotypes finaux) est visible aussi à l'échelle microscopique. La densité cellulaire a été divisée par deux en moyenne par rapport à l'inoculum, quel que soit le morphotype final. Le recyclage de la biomasse, principalement les bactéries hétérotrophes typiques des boues activées représentant 99±0.6% des cellules au départ, a pu servir à produire des EPS servant à la structuration spatiale de l'écosystème. Sans surprise, la densité en cyanobactéries a augmenté pour représenter jusqu'à 38±13% des cellules en fin d'expérimentation alors que la densité en algues eucaryotes (typiquement *Chlorella*) était stable. Les cyanobactéries les plus fréquentes étaient affiliées à *Planktothrix* et *Tychonema*. Comme attendu, ce sont bien des cyanobactéries filamenteuses mobiles appartenant à la Subsection III. Les bactéries hétérotrophes majoritaires en fin d'expérience étaient *Hydrogenophaga*, *Luteimonas* et *Porphyrobacter.* La moitié des morphotypes finaux contenaient des abondances élevées de *Sediminibacterium*. L'indice de diversité de Shannon n'a pas changé entre la boue activée initiale et les morphotypes finaux pour les cyanobactéries, a diminué pour les algues (enrichissement en *Chlorella*) et pour les bactéries non-phototrophes (deux fois moins d'OTUs).

Nous avons recherché quels facteurs expérimentaux pouvaient expliquer les différences de communautés microbiennes entre morphotypes : les séries d'expériences, l'origine de l'inoculum, la saisonnalité, le volume de l'inoculum, la durée des cultures. Une analyse de redondance sous contrainte basée sur une matrice de distance obtenue à partir de la structure des communautés a permis d'expliquer 35%, 40% et 38% des différences entre cyanobactéries, algues et bactéries hétérotrophes respectivement. Les séries d'expériences expliquaient à elles seules 27%, 37% et 32% des différences entre cyanobactéries, algues et bactéries hétérotrophes respectivement. Les morphotypes pouvaient expliquer seulement 5%, 4% et 3% des différences entre cyanobactéries, algues et bactéries hétérotrophes respectivement. Les morphotypes n'ont pas pu être différenciés statistiquement sur la base des communautés microbiennes, contrairement à l'hypothèse de départ. Il n'est donc pas possible de prédire le morphotype en se basant sur les communautés microbiennes.

Bien qu'il nous ait été impossible de détecter des différences de structure de communautés entre morphotypes, ni sur la taille de la communauté, les populations de cyanobactéries des photogranules étaient plus abondantes que pour les photogranules non cohésifs ou les tapis microbiens et particulièrement pour les biomasses floculées. Curieusement, les algues étaient plus nombreuses que les cyanobactéries dans 40 morphotypes sur les 186 analysés, correspondant à 13% des hémisphères, 14% des photogranules, 25% des tapis microbiens, 33% des photogranules non cohésifs et 88% des biomasses floculées. Il semble que l'abondance relative des cyanobactéries parmi les populations phototrophes augmente avec la structuration spatiale du morphotype.

Planktothrix était abundant dans les tapis microbiens, hémisphères, photogranules et photogranules non cohésifs, *Tychonema* dans les hémisphères et photogranules, *Limnothrix* dans les hémisphères et photogranules non cohésifs, et *Nostocales* dans les photogranules. *Chlorella* était l'algue la plus représentée dans tous les morphotypes. Concernant les bactéries non-phototrophes, *Hydrogenophaga*, *Luteimonas* et *Porphyrobacter* étaient très abondants dans tous les morphotypes. Une Gammaproteobacteria non identifiée était plus abondante dans les tapis microbiens, hémisphères et photogranules ; *Terrimonas* dans les photogranules et photogranules non cohésifs ; *Salinimonas* dans les tapis microbiens, photogranules non cohésifs et biomasses floculées ; une *Rhodobacteraceae* non identifiée dans les photogranules non cohésifs et biomasses floculées ; *Sediminibacterium* dans les photogranules non cohésifs ; une *Sphingomadaceae* non identifiée dans les biomasses floculées.

La diversité de Shannon des cyanobactéries était plus faible dans les photogranules par rapport aux hémisphères et aux tapis microbiens. La diversité de Shannon des bactéries non-phototrophes était au contraire plus importante dans les photogranules que dans les hémisphères, les tapis microbiens et tout particulièrement les biomasses floculées. La diversité de Shannon des bactéries hétérotrophes semble augmenter avec la spatialisation du morphotype, principalement à cause du nombre plus élevé d'OTUs. Une explication possible est qu'une plus grande spatialisation offre plus d'opportunités de niches écologiques, comme pour les photogranules avec des gradients de redox plus prononcés que pour les tapis microbiens.

Initial type and abundance of cyanobacteria determine morphotype development of phototrophic ecosystems (**Chapter 5**)

Les cyanobactéries filamenteuses mobiles appartenant à la Subsection III qui sont retrouvées dans la couche externe des photogranules doivent posséder les propriétés nécessaires à la photogranulation, alors qu'elles sont typiquement rares dans les boues activées. Des différences d'abondances initiales aléatoires sont très probables lors de l'ensemencement des tubes avec de la boue activée, simplement par effet statistique d'échantillonnage. Ceci peut expliquer les résultats non reproductibles observés en termes de morphotypes produits. Nous avons fait l'hypothèse qu'il était possible de modifier la distribution des morphotypes observées vers une plus grande proportion de photogranules en ajoutant ces cyanobactéries à la boue activée initiale.

Nous avons réalisé 5 expériences indépendantes où des boues activées ont été bioaugmentées avec des concentrations croissantes de cyanobactéries, provenant soit de photogranules entiers (iii, ix), de couches externes de photogranules (i,ii), d'isolats axéniques (v,vi,vii,viii) ou une souche de collection *Oscillatoria lutea* SAG 1459-3 (iv). *Tychonema* était dominante dans les bioaugmentations (i,ii,ix) et *Pantanalinema* était dominante pour (iii). Les souches isolées étaient affiliées à *Kamptonema* (v), *Planktothrix* (vi), *Nodosilinea* (vii) et à une cyanobactérie non affiliée (viii). La mobilité a été vérifiée sur boite et par observation microscopique.

Nous avons testé comment la dose initiale de cyanobactérie influençait la communauté microbienne finale et la structure spatiale. Les morphotypes produits ont été observés en fin d'expérience et les communautés microbiennes ont été analysées par PCR quantitative et séquençage des gènes d'ARN ribosomiques 16S et 23S.

Les boues activées utilisées comme inoculum étaient composées quasiment exclusivement de bactéries non-phototrophe (98.6±0.8%) avec 0.3±0.4% de cyanobactéries et 1.0±0.5% d'algues. Aucun OTU de bactéries non-phototrophes n'a été substantiellement enrichie durant l'incubation,

avec des OTUs ne représentant jamais plus de 5.2±6.4% de l'abondance totale. En revanche, les cyanobactéries ont été enrichies durant l'incubation pour atteindre en moyenne 35±15%, avec l'OTU majoritaire de cyanobactérie pouvant représenter 32±19% de l'abondance totale. C'est pour cette raison que nous avons focalisé notre analyse sur les cyanobactéries.

Pour les expériences contrôle avec les cinq boues non enrichies en cyanobactéries, la distribution des morphotypes a été collectée. Trois boues ne produisaient qu'un seul morphotype, des photogranules pour les boues 1 & 2, des tapis microbiens pour la boue 4. Deux boues produisaient des proportions variables des différents morphotypes, la boue 3 produisant majoritairement des tapis microbiens alors que la boue 5 produisait autant de chaque morphotype.

Lors des experiences de bioaugmentation avec des cyanobactéries, il a été possible de modifier la fréquence des morphotypes normalement attendus pour une boue témoin. Des ajouts massifs de *Tychonema* (i,ii) induisait la formation de tapis microbiens pour une boue qui formait naturellement des photogranules. L'ajout de *Pantanalinema* (iii) augmentait aussi la proportion de morphotypes tapis microbiens. L'ajout de la souche de collection *Oscillatoria lutea* (iv) à une boue qui produisait des tapis microbiens orientait la morphogénèse vers des photogranules.

Aussi bien *Kamptonema* que *Oscillatoria lutea* sont capables de former des photogranules sur milieu synthétique. *Planktothrix* produit des hémisphères. *Nodosilinea* forme des tapis microbiens avec des piliers émergeant de la surface du biofilm. *Tychonema* forme un biofilm à l'interface air-liquide. Les souches formant des tapis microbiens sont globalement plus distantes phylogénétiquement entre elles que les souches formant des photogranules.

Le morphotype caractéristique d'une souche a bien été propagé aux boues activées lors des expériences de bioaugmentation lorsque la dose initiale de cyanobactéries était suffisante. Par exemple, l'ajout de *Kamptonema* ou *Oscillatoria lutea* a bien provoqué la formation majoritaire de photogranules, l'ajout de *Planktothrix* a bien favorisé la formation d'hémisphères, et l'ajout de *Nodosilinea* ou de *Tychonema* a bien favorisé la formation de tapis microbiens.

On peut conclure que l'ajout de cyanobactéries à une boue activée a un impact global à l'échelle de l'écosystème et que cet impact est proportionnel à la dose initiale. Plus la dose était élevée, plus on retrouve le morphotype correspondant à celui observé pour la souche seule cultivée en milieu synthétique. L'effet dose diot provenir du fait que la cyanobactérie introduite entre en compétition avec les cyanobactéries résidente, même si elles sont en très faible quantité initialement.

Discussion et Conclusion

L'objectif de mon travail de thèse était d'examiner les critères minimaux de formation des photogranules du point de vue d'une écologue microbienne. Une perspective est de se servir des résultats obtenus et proposer des stratégies de maitrise de la photogranulation en biotechnologie. Ce chapitre donne a aperçu de mes résultats principaux et comment ils contribuent à mieux comprendre l'assemblage des communautés et la morphogénèse lors de la photogranulation.

Durant ma thèse, les boues activées placées dans des conditions appropriées ne se sont pas systématiquement transformées en photogranules, comme c'était le cas avant le début mon travail. J'ai travaillé avec des boues activées qui produisaient des morphotypes variés. Comme le système semblait produire systématiquement des photogranules avant mon travail de thèse, le travail de collecte d'information sur les boues initiales était moins poussé que ce que j'ai pu réaliser durant ma thèse. Il est donc difficile d'identifier a posteriori les différences. En se basant sur les

données de bioaugmentation du **Chapter 5**, ce changement de comportement des boues activées pourrait être dû à des différences d'abondance des cyanobactéries formant soit des tapis microbiens, des hémisphères ou des photogranules. Ces différents groupes fonctionnels de cyanobactéries interagissent et entrent en compétition, déterminant ensuite le type de structures spatiales formées.

Je comptais en début de thèse modifier les paramètres d'inoculation de la boue activée et mesurer comment cela affecterait la dynamique de la photogranulation et le diamètre final du photogranule. J'ai donc développé et publié un protocole haut-débit d'imagerie présenté dans le **Chapter 3**. Il est possible grâce à ce dispositif de de mesurer la dynamique de contraction de la biomasse de de nombreux tubes en parallèle sans avoir à les déplacer et à modifier les conditions environnementales. Cette approche originale a été moins productive que prévu vu le faible taux de succès de la photogranulation et la diversité des morphotypes observés pour certaines boues activées testées.

J'ai ensuite analysé un grand nombre d'expérimentations indépendantes et échantillonné toutes les structures spatiales distinctes que j'ai pu observer durant trois ans (biomasse floculée, tapis microbien, hémisphère, photogranule non-cohésif, photogranule). J'ai cherché à corréler des différences de structures de communautés microbiennes avec les morphotypes, avec l'objectif d'identifier les espèces clé pour la photogranulation (**Chapter 4**). Contrairement à ce que j'attendais, je n'ai pas pu identifier de corrélation statistique. Mon hypothèse est que la morphogénèse doit dépendre d'événement précoces au sein de la communauté lors de la transformation de la boue activée. Une succession de microorganismes doit intervenir jusqu'à la formation des photogranules et la communauté finale qui a été échantillonnée ne reflète pas totalement cette succession. J'ai pu observer que le ratio cyanobactérie/algue était plus important dans les photogranules que pour les autres morphotypes, là où la structure spatiale est la plus hétérogène. Les fortes intensités lumineuses appliquées durant les incubations, et la lumière en continu, ont pu sélectionner un type de cyanobactérie qui aurait pris le dessus au cours des semaines d'incubation, malgré le rôle potentiellement crucial de certaines espèces de cyanobactéries lors des étapes initiales de la morphogénèse. Une hypothèse qui pourrait expliquer la formation de photogranule est l'agencement spécifique en couches concentriques pour se protéger de l'excès de lumière, les filaments les plus externe faisant de l'ombre aux cellules plus à l'intérieur, les protégeant ainsi de la photo-inhibition comme cela a été décrit pour les photogranules observés dans l'environnement. La couche externe était formée ici de filaments épais et robustes de cyanobactéries (*Tychonema* et *Planktothrix*) qui formaient une couche dense de filaments et d'EPS, protégeant les espèces plus fragiles au cœur du photogranule.

Les bactéries non-phototrophes étaient plus abondantes et les populations plus nombreuses dans les morphotypes plus spatialisés. Les photogranules ont un ratio surface/volume plus petits que les autres morphotypes, et par là même proportionnellement moins de couche phototrophe. Les bactéries sont aussi distribuées le long de gradients d'oxygène, de redox et de nutriments plus marqués que pour les autres morphotypes, surtout si on compare aux tapis microbiens plats. Cela doit avoir une conséquence sur la distribution des niches écologiques et sur la composition de la communauté microbienne. Par ailleurs, les bactéries non-phototrophes dominantes dans les divers morphotypes (*Hydrogenophaga*, *Luteimonas* et *Sediminibacterium*) étaient similaires à celles retrouvées associées aux cultures monoclonales de cyanobactéries. Cela suggère que ces microorganismes doivent vivre en proximité et peuvent avoir des relations syntrophiques.

J'ai appris grâce aux expériences de bioaugmentation du **Chapter 5** qu'il était possible de piloter la morphogénèse de l'écosystème par l'ajout de cyanobactéries si la dose était suffisante. Les souches introduites entrainaient la formation de tapis microbiens, d'hémisphères ou de photogranules, alors que la communauté microbienne finale était toujours dominée en fin d'incubation par *Tychonema*, plus compétitive et connue pour induire la formation de tapis microbiens. Il semble que la présence de cyanobactéries favorisant la formation de photogranules soit seulement utile lors des phases initiales de la photogranulation, mais pas pour le maintien de la forme sphérique.

La question est maintenant de savoir quand la cyanobactérie formant des photogranules, *Kamptonema*, disparait de l'écosystème. J'ai fait l'hypothèse que *Kamptonema* pouvait être fonctionnel au début de l'incubation mais qu'il n'était plus compétitif vis-à-vis des autres souches lors de la croissance. *Kamptonema* peut produire une matrice initiale composée de gaines vides et d'autres polymères qui serviraient de structure pour initier la formation du photogranule.

J'ai isolé à partir de photogranules matures beaucoup plus de cyanobactéries favorisant les tapis microbiens que des cyanobactéries qui favorisent la formation de photogranules. Ça pouvait paraître curieux initialement mais après analyse des communautés microbiennes de photogranules matures, nous nous sommes aperçus que les cyanobactéries favorisant les tapis microbiens étaient les plus abondantes dans les photogranules matures. Les cyanobactéries favorisant la formation de photogranules semblent phylogénétiquement assez proches. Cela peut vouloir dire que la propriété de photogranulation n'est peut-être pas aussi répandue que se qu'on avait imaginé avant. Maintenant que nous avons en main des souches produisant tous les morphotypes, il nous est possible de tester systématiquement les différences entre ces souches (croissance, mobilité, propriétés de surface, etc.).

Un moment clé de ma thèse a été de me focaliser sur l'isolement de souches de cyanobactéries et l'utilisation de souches de collection. Le fait d'observer des photogranules avec certaines souches cultivées sur milieu minimum m'a prouvé qu'il était possible d'obtenir des photogranules sans matrice biologique initiale. Contrairement aux granules issus de boue activée, ces photogranules formés sur milieu minimum ne possèdent pas de cœur formé de biomasse non consolidée. A partir d'observations microscopiques, le cœur semble au contraire constitué de résidus de l'activité des cyanobactéries (gaines de cyanobactéries vides, EPS). Les cyanobactéries peuvent donc produire leur propre matrice pour initier la formation de photogranules. Je ne sais pas par contre la contribution des bactéries hétérotrophes associées à la production d'EPS. Il faudrait pour cela utiliser des souches de cyanobactéries axéniques.

Lors de ma thèse, j'ai travaillé à l'interface entre les domaines de l'écologie microbienne et l'ingénierie des procédés. Le phénomène de photogranulation était connu dans les environnements naturels avec des eaux semi-stagnantes, mais jamais dans un contexte de biotechnologie. J'ai acquis une meilleure compréhension des conditions minimales permettant la photogranulation : une cyanobactérie adaptée dans un milieu minimum synthétique suffit. Mes travaux pourront servir de base à de futures recherches sur la formation des granules en photobioréacteurs et sur l'ingénierie écologique de photogranules pour introduire de nouvelles propriétés biotechnologiques.


BN
C
CN
B

1

Introduction

Photogranulation describes the microbially-driven formation of dense, roughly spherical, phototrophic aggregates of several millimeters in diameter. Oxygenic photogranules (OPGs) have a photoactive layer of filamentous cyanobacteria and extracellular polymeric substances (EPS) that resembles a microbial mat, however, with a strikingly different geometry. Photogranules can be produced in the laboratory in hydrostatic batch cultivations from activated sludge of a wastewater treatment plant, or in turbulently mixed reactors (Milferstedt et al., 2017). Heterotrophic bacteria live in close association with the cyanobacteria in the outer layer, and form the interior of the photogranule. They interact syntrophically with the cyanobacteria exchanging organic carbon, CO_2 and oxygen (**Figure 1.1**). Because of this syntrophic relationship and their high settleability, photogranules have the potential to be applied in biotechnological applications such as aeration-free wastewater treatment and biomass valorization (Abouhend et al., 2018; Quijano et al., 2017). Aggregates similar to photogranules can be found in nature in a variety of habitats, e.g., cryoconite granules on glacier surfaces (Takeuchi et al., 2001), modern microbialites in marine waters (Brehm et al., 2003) and in tropical lagoons (Abed et al., 2003). Factors driving community assembly and the development of the three-dimensional (3D) photogranule structure are today largely unknown. The aim of my thesis is to investigate the minimum requirements for the formation of oxygenic photogranules from a microbial ecological angle.

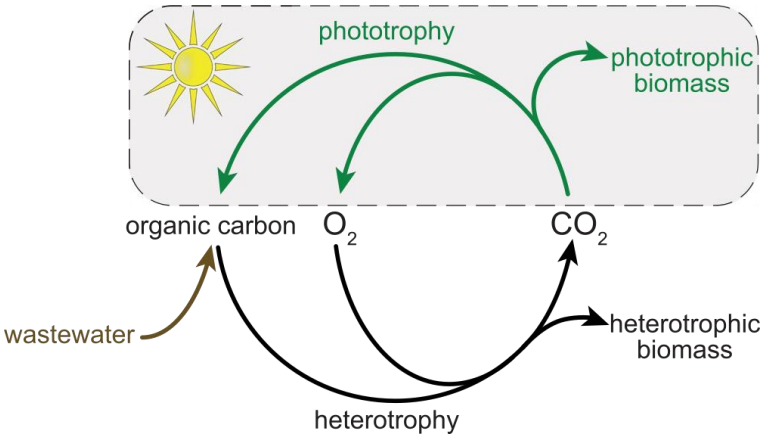

Figure 1.1. Syntrophic relationship in oxygenic photogranules. The lower part of the figure represents the conventional activated sludge process. Tight coupling of photoautotrophic (upper part) and heterotrophic activities may close CO_2 and O_2 cycles in wastewater treatment. Figure from Milferstedt et al. (2017b).

1.1 Cyanobacteria in photogranules: lessons to be learnt from microbial mats

The outer layer of a photogranule resembles a spherical microbial mat densely populated by filamentous cyanobacteria. To better understand the requirements for photogranulation, I studied the role of cyanobacteria in naturally occurring mats.

1.1.1 *Phototrophic microbial mats*

Microbial mats are macroscopic structures of multiple layers of microbial populations that are horizontally arranged (**Figure 1.2**a) (Prieto-Barajas et al., 2018). This stratification arises from steep and fluctuating physical and chemical microscale gradients, specifically of light, oxygen, redox, pH and sulfide (Stal, 1995). Microorganisms in a microbial mat are embedded in a matrix of EPS that glues the cells together and provides them protection. The photogranule outer layer resembles the structure of a microbial mat (**Figure 1.2**b).

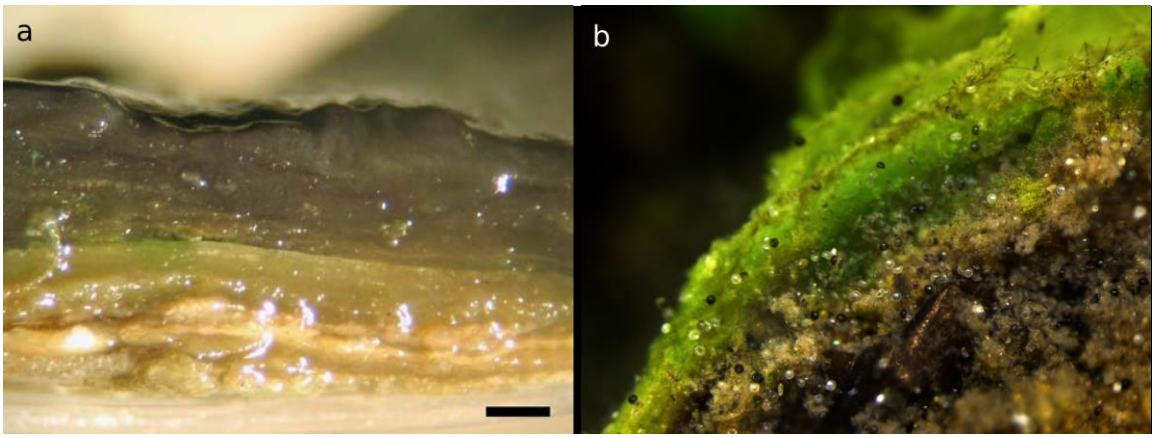

Figure 1.2. Microbial mat structure. (a) Typical microbial mat structure (millimeters to centimeters) with multiple layers of microorganisms embedded in an EPS matrix. Scale bar indicates 1 mm. Figure from (Roeselers et al., 2008). (b) Cross section of a photogranule showing the phototrophic layer and non-phototrophic interior. Image taken by the author.

Microbial mat formation involves several steps that may overlap: (i) initial cell-to-substratum attachment by adsorption, (ii) formation of a monolayer by strong adhesion and surface colonization, (iii) formation of microcolonies by cell aggregation and EPS production, (iv) formation of macrocolonies (maturation), and (iv) dispersal (Guzmán-Soto et al., 2021). Cyanobacteria are the main builders of microbial mats worldwide (Stal et al., 1985). They are often the primary colonizers of a substratum and initiate the formation of a microbial mat. Cyanobacteria are the first contributors to EPS synthesis and produce an EPS matrix that favors formation of microbial associations (Rossi and De Philippis, 2015). EPS bridges cells and can partially overcome cells' negative surface charge to enable coagulation. These polymers contribute to a structurally-stable and hydrated microenvironment, and offers protection from abiotic stress and predation.

Cyanobacteria are the principal primary producers of mat ecosystems (Stal, 1995). Cyanobacteria are found in the top layers of the microbial mat, because they need light for CO_2 fixation into organic substrates. The photosynthetically produced organic matter is decomposed by heterotrophic bacteria as energy and carbon source for heterotrophic respiration. Heterotrophs are closely associated with cyanobacteria. They can live and feed on the mucilaginous EPS layers surrounding the cyanobacterial cells. Microorganisms move from or to the surface of a mat in response to or in anticipation of changes in environmental conditions. Filamentous cyanobacteria exhibit the ability to actively move across physicochemical gradients in microbial mats to optimize their position and obtain resources (Park et al., 2003; Tamulonis et al., 2011).

1.1.2 *Gliding motility*

Filamentous cyanobacteria consist of chains of cells that form trichomes. If the trichome is surrounded by a mucilaginous sheath, or coating, it is called a filament. Sheaths are condensed fractions of polysaccharides forming thin layers surrounding the cells (De Philippis and Vincenzini, 1998). They protect cells from environmental stresses, such desiccation, grazing by predators and ultraviolet radiation (Stal, 1995).

Many filamentous cyanobacteria exhibit gliding motility. This is a type of cell movement in which the trichome moves in the direction of its long axis when in contact with a (semi)solid surface (Hoiczyk, 2000). Cyanobacteria secrete slime through a set of pores which propels the cells forward while gliding. Some cyanobacteria move forward along their long axis, while others rotate

along their long axis as they move forward (Stal, 1995). Cells coordinate their gliding direction through an electrical potential that induces a “head” and a “tail”. Trichomes usually reverse their motility randomly with an average period in the order of minutes to hours (Häder, 1987). Trichomes can change their reversal frequency and speed of gliding based on light and chemical stimuli.

1.1.3 *Photoresponses and chemotaxis*

Light seems to be the major factor triggering cyanobacterial gliding motility (Hoiczyk, 2000). Filamentous cyanobacteria can move in response to environmental stimuli to find a niche suitable for survival and growth (Castenholz, 1982). Photomovements may provide a means to optimize photosynthetic performance and to avoid photodamage or burial by sedimentation (Garcia-Pichel & Castenholz, 2001; Pentecost, 1984). Phototrophs have three motility responses to light: phototactic, photokinetic, and photophobic responses (Castenholz, 1982; Häder, 1987). In phototaxis, the direction of movement is dependent on the direction of incident light. Cyanobacteria move either towards (positive phototaxis) or away from the light (negative phototaxis) using a light sensing mechanism or by trial and error. Photokinesis depends on the intensity of light: gliding speed increases with irradiance because of the increased energy supply. In photophobic responses, the direction of movement is dependent on the detection of abrupt changes in light intensity: cyanobacteria can cluster in areas of lower (step-up photophobic response) or higher light intensity (step-down response) (Kruschel and Castenholz, 1998; Pentecost, 1984). Photomovement thus help cyanobacteria to actively position themselves with great accuracy in their environment. Phototaxis is mostly useful for phototrophs living at the sediment surface (Garcia-Pichel & Castenholz, 2001), and photophobic responses for cyanobacteria within the microbial mat where light is uniformly distributed through light scattering (Stal, 1995).

Cyanobacteria often reduce their movement when conditions are optimal so that they can remain in a favorable spot and use their energy for other processes. For example, *Microcoleus chthonoplastes* minimizes its movement when light conditions are favorable (Ramsing and Prufert-Bebout, 1994). The filamentous cyanobacterium moves less frequently, increases its reversal frequency and bends its trichomes. The bending of trichomes results in the formation of bundles in which motility is restricted. This eventually leads to the production of a microbial mat. In contrast, *Oscillatoria terebriformis* forms an interwoven network of filaments in response to suboptimal light conditions, i.e., high light intensity (Richardson and Castenholz, 1989).

Cyanobacteria can also move in response to chemical gradients to optimize uptake of nutrients or to avoid harmful environments (Chet and Mitchell, 1976). Chemotactic behavior of cyanobacteria has been less extensively studied than their movements to light, but a couple of examples are described in the literature. *Microcoleus chthonoplastes* shows a positive response to oxygen (aerotaxis) (Whale and Walsby, 1984) and *Oscillatoria* sp. towards oxygen, CO_2 and bicarbonate (Malin and Walsby, 1985). *Oscillatoria terebriformis* shows a negative chemokinetic response to sulfide (Richardson and Castenholz, 1987). *Oscillatoria* sp. in deserts soils shows hydrotactic motility: cyanobacteria actively move up to the surface, or down into the soil, depending on wetting and drying events (Garcia-Pichel & Pringault, 2001).

1.1.4 *Macroscopic structure formation*

The formation of a range of macroscopic structures observed in nature can be directly linked to the activities of gliding filamentous cyanobacteria (Andersen et al., 2011). Gliding filamentous cyanobacteria produce columnar and conical structures in microbial mats and laboratory cultures through photomovement (Walter et al., 1976). Cyanobacterial metabolism leads to the formation of small conical stromatolites (Petroff et al., 2010). Assembly dynamics of *Trichodesmium* also depends on the nutrient status of the cells. *Trichodesmium* can self-assemble into fusiform “tufts” when its trichomes are aligned in parallel, and spherical “puffs” when they are aligned radially (Prufert-Bebout et al., 1993). *Pseudanabaena geleta* forms comets (Castenholz, 1982) that resemble *Trichodesmium* tufts.

At sufficient trichome density, *Anabaena cylindrica* and *Pseudanabaena* can form clumps through random gliding movements (Shepard and Sumner, 2010; Tamulonis and Kaandorp, 2014; Walsby, 1968). When moving randomly, trichomes collide and entangle and become part of multiple smaller aggregates. The trichomes in an aggregate continue to move, pulling different parts of a filaments in different directions. Tension on the filaments then pulls the small aggregates together to form one big clump. The same phenomenon was observed for an *Oscillatoria terebriformis* population that was removed from a mat and dispersed into water from the hot spring (**Figure 1.3**a). It rapidly aggregated to form a ball (**Figure 1.3**b) (Garcia-Pichel & Castenholz, 2001). When filaments glide and collide, they coil and tangle to form rope-like strands (Castenholz, 1967). Through flexional movements, these strands bend laterally to contract the biomass. Aggregation does not happen when filaments are immotile (Castenholz, 1967).

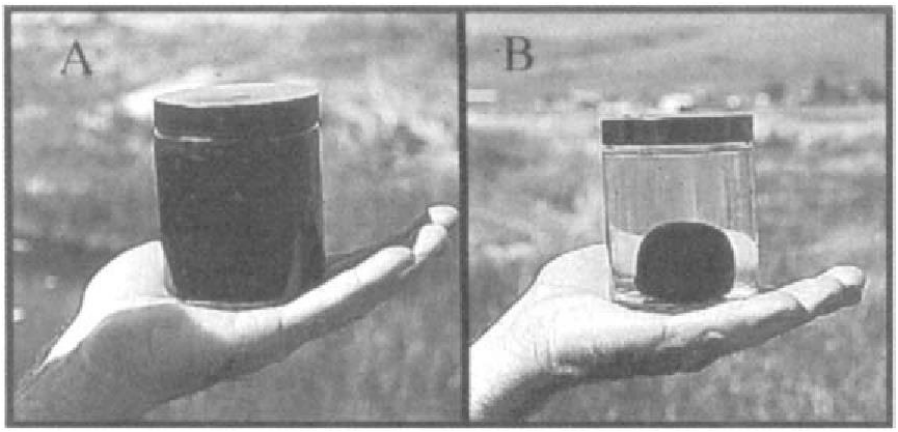

Figure 1.3. Aggregation of *Oscillatoria cf. terebriformis*. (a) Population of *Oscillatoria cf. terebriformis* trichomes from a benthic mat from Hunter's Hot Springs (Oregon, USA) dispersed in spring water transforms into (b) a ball as a resulting of gliding motility after 5 minutes in the light. Temperature was approximately 40°C. Figure from Garcia-Pichel & Castenholz (2001).

Shepard and Sumner (2010) showed that dense cyanobacterial cultures formed macroscopic structures on different substrates, such as sand and glass, and that trichomes did not respond to differences in light intensity. The authors therefore concluded that these structures do not form as a response to external stimuli. They hypothesized that if trichomes would respond to an external signal, they would move into the same direction, preventing the colliding and coiling that is needed for clump formation. They indicated, however, that physicochemical conditions that affect gliding motility also (indirectly) affect aggregation. They furthermore explained that clumps can also form from less dense cyanobacterial cultures, but that cyanobacterial growth and division are then needed to reach sufficiently high trichome densities for clump formation. This growth-dependent

aggregation is obviously more affected by environmental conditions than direct aggregation of initially sufficiently dense cultures. In a mathematical model, Tamulonis and Kaandorp (2014) demonstrated that random gliding movements of long and flexible trichomes at high density are sufficient to form reticulate patterns, i.e., a two-dimensional structure. Dense clumps were formed when cohesion exceed gliding motility.

Other studies, on the other hand, showed that formation of spherical aggregates results from directed cyanobacterial movements controlled by external stimuli e.g., light or chemical stimuli. For example, *Oscillatoria terebriformis*-dominated photogranules develop as response to high light intensity or suboptimal temperature in sulfide-rich hot springs (Castenholz, 1968). *Phormidium*-dominated photogranules form in response to signal molecules released by heterotrophic bacteria in marine waters (Brehm et al., 2003). Photogranules can also be produced at elevated oxygen concentrations, whereas flat microbial mats form at lower oxygen concentrations (Sim et al., 2012).

1.2 Lessons to be learnt from photogranules in nature

Even though microbial mats and macroscopic cyanobacterial structures are commonly observed worldwide, the formation of spherical aggregates seems to occur less often. Spherical phototrophic aggregates are nevertheless found across a wide range of habitats, including hot springs (Hanada et al., 1995), salt marshes (Wilbanks et al., 2014), high-altitude lakes (Soejima et al., 2009), freshwater lakes (Fang et al., 2014) and marine waters (Berrendero et al., 2008; Sihvonen et al., 2007). These spherical aggregates are dominated by various different phototrophic communities of, respectively, (i) filamentous, anoxygenic photosynthetic bacteria, (ii) sulfate-oxidizing purple sulfur bacteria and sulfate-reducing bacteria, (iii) filamentous eukaryotic algae, (iv) unicellular cyanobacteria and (iv) branched filamentous heterocystous cyanobacteria. This shows that not only cyanobacteria can form photogranular structures. My focus is, however, on ecosystems that are dominated by filamentous, non-heterocystous cyanobacteria, because they are predominantly present in photogranules produced from activated sludge in the laboratory (Milferstedt et al., 2017). Naturally occurring photogranules similar to laboratory photogranules include cryoconite granules on glacier surfaces and microbialites in marine waters and tropical lagoons. In the following paragraphs, I describe the main characteristics of these ecosystems to derive lessons from them to better understand photogranulation in the laboratory. Other photogranular types that I found in the literature, but are not discussed in detail are those in permanently frozen lakes (Paerl and Priscu, 1998), marine and freshwaters (Paerl et al., 1989), submerged sinkholes (Biddanda et al., 2015) and sulfide-rich hot springs (Richardson and Castenholz, 1989).

1.2.1 *Cryoconite granules on glacier surfaces*

One specific type of naturally occurring photogranules is cryoconite. Cryoconite granules are dark-colored, millimeter-sized, roughly spherical aggregates composed of microorganisms, mineral particles and organic matter (**Figure 1.4**a) (Takeuchi et al., 2001). They form on glacier surfaces in polar and temperate regions worldwide (Wharton et al., 1985). Dark-colored wind-blown dust collects on a glacier or ice sheath, absorbs heat from the sun, and vertically melts centimeter-deep holes into the glacier called cryoconite holes (Gerdel and Drouet, 1960). The dust particles provide a source of microbial cells and nutrients. The cryoconite holes provide a semi-stagnant aquatic habitat for microbial growth because they trap nutrient-rich particles and prevent washout by meltwater streams (Takeuchi et al., 2001).

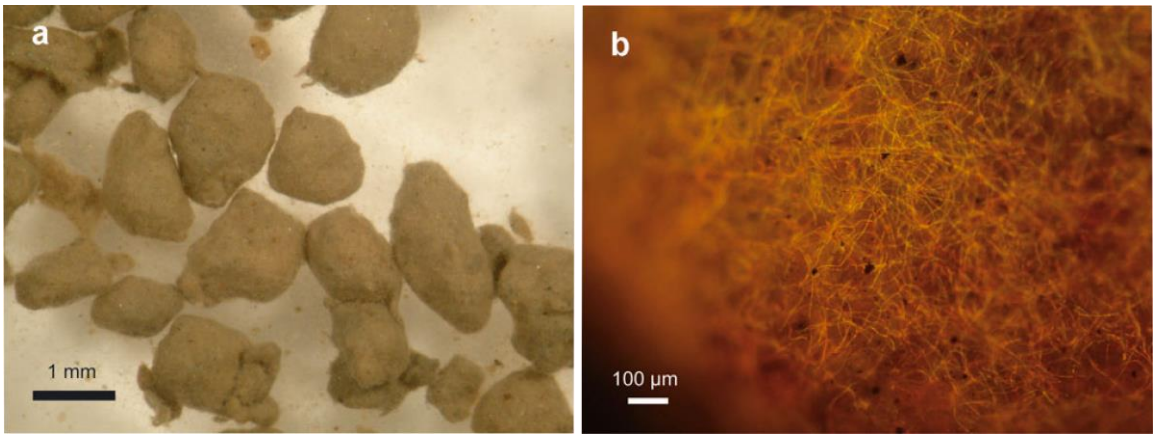

Figure 1.4. Top and close-up view of filamentous cyanobacterial cryoconite surface layer. (a) Microscopic view of brown, roughly spherical cryoconite granules collected from Ürümqi glacier No. 1. (b) Dense network of filamentous cyanobacteria on the surface of the cryoconite granule, as observed with fluorescence microscopy. Figures from Takeuchi et al. (2010).

Filamentous cyanobacteria are universally found in cryoconite ecosystems (Christner et al., 2003; Porazinska et al., 2004; Takeuchi et al., 2001). They are considered ecosystem engineers in cryoconite granules because they physically structure the aggregate (Edwards et al., 2014) and change physicochemical conditions by production and accumulation of organic matter (Anesio et al., 2017). The outer layer of the cryoconite is a living mat-like network of filamentous cyanobacteria of tenths of micrometers in thickness (Langford et al., 2010; Takeuchi et al., 2010, 2001) that holds the organic and mineral particles together in a dense sphere (**Figure 1.4**b). Cyanobacteria produce EPS that chemically trap and bind mineral and organic particles, forming microaggregates (Langford et al., 2010; Paerl and Priscu, 1998; Takeuchi et al., 2001). These microaggregates are physically bound by abundant filamentous cyanobacteria to form cryoconite granules.

Cryoconite granules do not have a physical internal structure at the initiation of their formation (**Figure 1.5**a). Each summer, the granules grow by the activity of filamentous cyanobacteria that create concentric layers of dense organic matter (**Figure 1.5**a) (Takeuchi et al., 2010). This cyanobacterial layering corresponds to oxygenic photogranules that develop in bioreactors (**Figure 1.10**). Granule size may be physically limited, e.g., by the binding ability of filamentous cyanobacteria and adhesive organic matter (Takeuchi et al., 2001), heterotrophic consumption of carbohydrates, a reduction in photosynthetic activity, or transport or freezing events (Takeuchi et al., 2010). Cryoconite stability can be maintained because cyanobacterial sheaths are recalcitrant to mineralization (De Winder et al., 1999). Takeuchi et al. (2010) hypothesized that cryoconite movement by meltwater flow is needed to maintain the spherical shape. They expect cyanobacteria to spread horizontally over a surface and form a flat microbial mat when the granule is retained on that same surface over months, but never observed mat formation on glaciers. To my knowledge, the role of gliding motility in the formation of cryoconite granules has not been discussed in the literature.

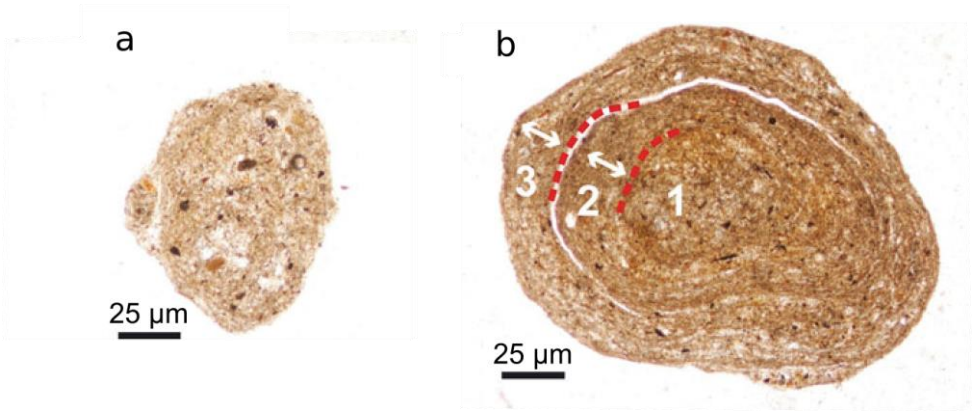

Figure 1.5. Cross sections of cryoconite granules. (a) Unstructured cryoconite granule. (b) Cryoconite granule with three concentric layers of organic matter. Figure adapted from Takeuchi et al. (2010).

Due to structural heterogeneity, different microenvironments exist across the diameter of the cryoconite granule (Edwards et al., 2013), allowing growth and activity of diverse microbial communities (Edwards et al., 2011; Hodson et al., 2008; Zarsky et al., 2013). Cyanobacteria in the cryoconite outer layer often belong to Subsection III (Cameron et al., 2012; Christner et al., 2003; Langford et al., 2010; Segawa and Takeuchi, 2010; Zarsky et al., 2013) according to Castenholz et al.'s description in Bergey's Manual of Systematics of Archaea and Bacteria (Castenholz et al., 2015). These cyanobacteria are characterized by a filamentous morphology and often gliding motility. Heterotrophic bacteria, mostly *Alpha*- and *Betaproteobacteria*, *Bacteroidetes* and *Actinobacteria* (Edwards et al., 2013, 2011; Stibal et al., 2015; Xiang et al., 2009; Zarsky et al., 2013; Zeng et al., 2013), are heterogeneously distributed over the granule, but often cluster in areas with phototrophic activity and organic matter availability. Unicellular cyanobacteria and eukaryotic algae are low abundant in cryoconite granules (Langford et al., 2010). Through photosynthesis and heterotrophic respiration, carbon is recycled in cryoconite granules by carbon fixation (Hodson et al., 2010). Atmospheric CO_2 is the major carbon source of cryoconite granules (Stibal et al., 2012). Cryoconite granules provide a source of organic carbon to the glacier ecosystem (Takeuchi et al., 2001).

1.2.2 *Modern microbialites*

Takeuchi et al. (2001) indicated that the development of cryoconite granules and their layered structure resembles that of stromatolites. Stromatolites are well-laminated microbialites, which are organosedimentary structures. Stromatolites are formed by filamentous cyanobacteria within a microbial mat that trap, bind and lithify sediment particles (Andres and Reid, 2006; Moore and Burne, 1987). Stromatolites typically consist of layers of filamentous cyanobacteria, empty sheaths and other polymers, and carbonate minerals (Kühl et al., 2003). Stromatolites can have diverse microbial communities that are dominated by cyanobacteria and proteobacteria (Havemann and Foster, 2008). Gliding filamentous cyanobacteria are the pioneers that colonize sandy sediments. The sediment accretes through cyanobacterial proliferation and associated excretion of EPS that trap and bind soil particles (Reid et al., 2000). The resulting dense network provides structural integrity to the stromatolite (Foster et al., 2009). Cyanobacterial sheaths, that are resistant to degradation, furthermore contribute to the thickness of the mat. Their repetitive layering is formed by a combination of microbial activities and calcium carbonate precipitation (Fenchel and Kühl, 2000; Reid et al., 2000). Differences in stromatolite spatial organization originate from metabolic processes associated with their development (Havemann & Foster,

2008). Phototactic motility and light-dependent EPS production are considered to be essential for stromatolite formation (Foster et al., 2009). It is, however, not known whether the spatial organization of cyanobacteria arises from photoresponses or from a geometric limitation related to filament reproduction (Fenchel and Kühl, 2000).

1.2.3 *Modern microbialites in marine waters*

Modern microbialites with a diameter of 0.8 to 3 mm have been observed in North Sea microbial mats (**Figure 1.6**) (Brehm et al., 2003). They contain a symbiotic community of filamentous cyanobacteria (i.e., *Phormidium* sp. according to the classification of Rippka et al. (1979)), diatoms (i.e., *Navicula perminota*) and motile chemoorganotrophic bacteria. Stratification of these granules corresponds to that of benthic biofilms. Cyanobacteria are the dominant microorganisms regulating the formation of the macroscopic structure. Several stages were distinguished during the development of these granules in the laboratory. Firstly, motile chemoorganotrophic bacteria formed a spherical envelope of 1 to 3 µm in thickness. Diatoms were trapped within the envelope and multiplied until they filled up the entire sphere. Subsequently, bacteria or diatoms produced signal molecules that attracted gliding filamentous cyanobacteria to colonize the sphere. Finally, as a chemotactic response, cyanobacteria penetrated the bacterial envelope and aligned inside it to form a tightly interwoven mat. In the first weeks of growth, only cyanobacteria could enter and leave the spherical envelope. They moved actively in and out of the sphere to optimize their position, which is visible as tapered bundles of trichomes at the macroscale (**Figure 1.6**). This is a morphotype that I describe as a filamentous photogranule, macroscopically highly similar to what we observed in continuously operated bioreactors (**Figure 1.11**b). Mature granules can remain stable for several months, even when the trapped diatoms are released. Carbonate precipitation on cyanobacterial sheaths in concentric layers around the granule core subsequently produces the microbialite (Brehm et al., 2006, 2004). Calcium carbonate precipitation happens with increased pH as a result of microbial activities, e.g., oxygenic photosynthesis, because uptake of CO_2 and (or) bicarbonate increases the saturation level with respect to the solubility product of calcite (Kühl et al., 2003).

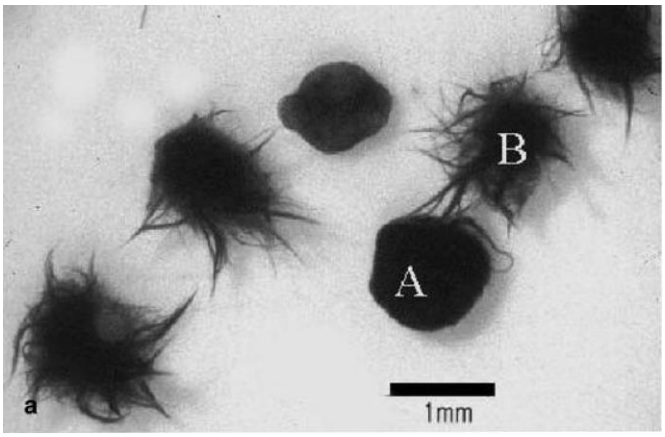

Figure 1.6. Spherical phototrophic aggregates in the North Sea. Microbial spheres of filamentous cyanobacteria (*Phormidium* sp.), diatoms (*Navicula perminota*) and motile chemoorganotrophic bacteria. (A) indicates a smooth granule and (B) a filamentous granule. Figure from Brehm et al. (2003).

1.2.4 *Modern microbialites in tropical lagoons*

Macroscopic structures in tropical coastal areas are formed by benthic filamentous cyanobacteria that cover sediment on the lagoon floor, i.e., microbial mats, hanging gelatinous masses and compact spherical colonies (Abed et al., 2003), the latter presenting similarities with photogranules. Spherical colonies can by formed by a variety of cyanobacteria (**Figure 1.7**a-c). *Hydrocoleum* of Subsection III is the most common cyanobacterium in tropical oceans (Palińska et al., 2015), followed by *Symploca, Leptolyngbya, Lyngbya*, *Oscillatoria,* and *Phormidium,* and heterocystous *Anabaena* of Subsection IV (Charpy et al., 2012, 2010; Zubia et al., 2019, 2016). Spherical colonies are formed by cyanobacterial growth and gliding movements. Filaments that move to surface of the colony leave their sheath behind in the interior of the colony. The sheaths then provide a matrix for entrapment of sediment particles and serve as a site for carbonate precipitation (Sprachta et al., 2001). This results in the formation of a modern microbialite (Moore and Burne, 1987). Benthic cyanobacteria are responsible for the formation of microbialites in terms of organic input and structural integrity (Golubic et al., 2000).

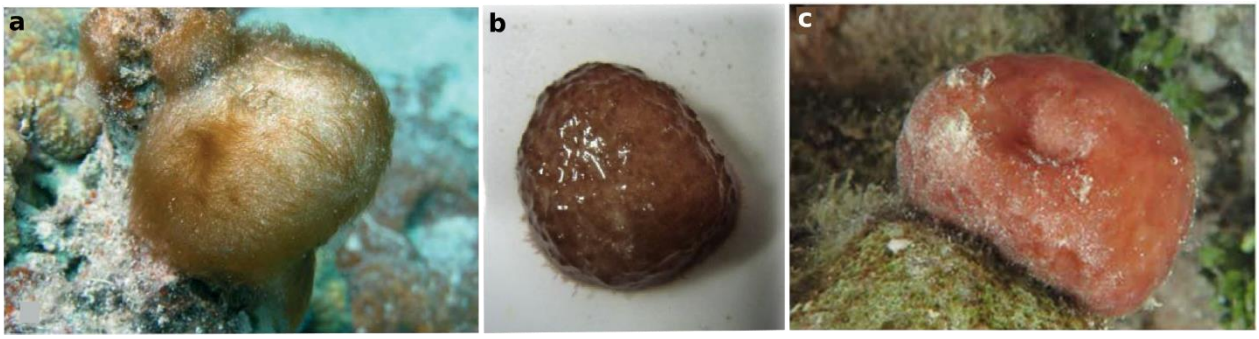

Figure 1.7. Spherical cyanobacterial aggregates from tropical lagoons. (a) *Hydrocoleum cantharidosmum* on the reef, New Caledonia lagoon. Figure from Charpy et al. (2007). (b) *Schizothrix minuta* on coral reefs of Moorea Island. Figure from Zubia et al. (2019) (size not mentioned for a, b). (c) *Homoeothrix rubra* (2 cm in diameter). Figure from Zubia et al. (2016).

1.2.5 *Why do granular aggregates form?*

Filamentous cyanobacteria generally form biofilms and aggregates to sense stimuli over larger distances and respond more efficiently to changing conditions than individual filaments could (Castenholz, 1968). Cells are therefore more likely to move to an area with optimized physicochemical conditions, e.g., it allows *Oscillatoria* to measure light between more distant points, which prevents it from falling into small sub-optimal light traps (Tamulonis et al., 2011). Different hypotheses exist as to why spherical aggregates would form. It has been proposed that photogranules form in nutrient-poor environments, e.g., on glacier surfaces, because they provide a means for cyanobacteria to keep their nutrients close (Takeuchi et al., 2001; Togashi et al., 2014). Brehm et al. (2006) hypothesized that the spatial structural of a spherical aggregate provides a better organization of light, nutrients and other resources, but they did not further explain this. Paerl & Priscu (1998) explained that the formation of spherical aggregates is an efficient way of establishing close spatial and temporal coupling of producers and consumers of organic matter, i.e., phototrophs, heterotrophs and diazotrophs, along a physicochemical gradient. Clumps are promoted in oxic media (**Figure 1.8**a) in which high oxygen concentrations reduce photosynthesis efficiency and promote glycolate excretion (Sim et al., 2012). Clumping is then beneficial to accumulate carbon inside the spheres. Oxic media furthermore increase cyanobacterial frequency and filament bending, making it less likely for a filament to migrate away from the clump. In oxygen-limited conditions (**Figure 1.8**a), cyanobacteria organize themselves as flat mats with a higher oxygen concentration at the surface than in clumps to have sufficient

oxygen and organic substrates for heterotrophic respiration. Oxygen and carbon cycles in clumps are tightly coupled (**Figure 1.8**b). Brehm et al. (2006) hypothesized that the sphere provides an advantage for the microorganisms living in the interior, because they are protected from grazing and harsh environmental conditions. It may equally help slow-growing microorganisms to remain in the environment. Another possibility is that photogranulation is a response to high light intensities, whereby self-shading can minimize photodamage (Castenholz, 1968, 1967).

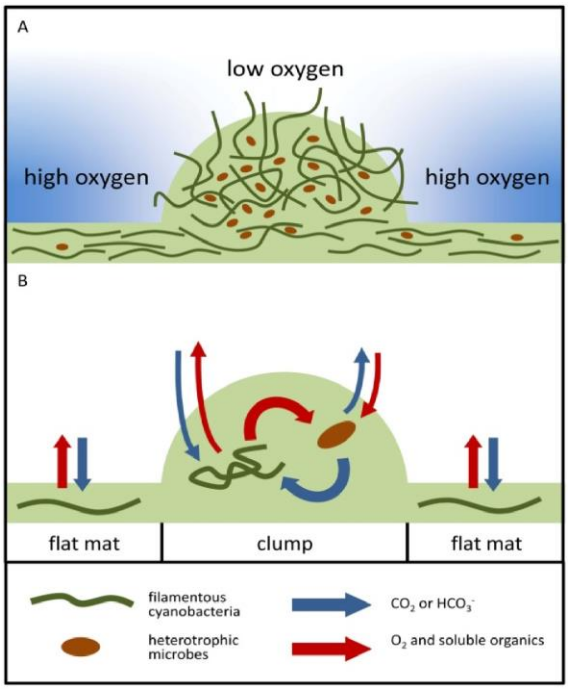

Figure 1.8. Clump formation is beneficial in oxic environments. (a) Distribution of heterotrophic microbes and filamentous cyanobacteria in clumps and flat mats. Higher density of microbes in clumps than in flat mats. (b) Carbon and oxygen cycling in clumps and flat mats. Spatial coupling between photosynthesis and heterotrophic respiration in clumps. Figure from Sim et al. (2012).

1.3 Production of photogranules in the laboratory

Some of the photogranules observed in nature have been successfully reproduced in the laboratory, such as those found in sulfide-rich hot springs (Castenholz, 1968, 1967) and submerged sinkholes (Biddanda et al., 2015). Microbialites were successfully reproduced by Brehm et al. (2003) in hydrostatic cultivations over a period of eight to ten weeks. Havemann & Foster (2008) successfully produced artificial microbialites from natural with highly similar macroscopic and microbial structures. There have been, however, also failed attempts to produce photogranules in the laboratory, such as for cryoconite granules resulting in the development of flat microbial mats (Takeuchi et al., 2001). In my thesis, I choose hydrostatic photogranulation as a model system to study community assembly and formation of the spherical structure.

1.3.1 *Photogranules in hydrostatic batch cultivations*

Photogranules can be produced in hydrostatic batch cultivations. Activated sludge from the aeration basin of a wastewater treatment plant is transferred into vials that are closed and hydrostatically incubated under light illumination. The sludge transforms into a single photogranule per vial over the course of several weeks. During this transformation, the mostly heterotrophic activated sludge community transforms into a syntrophic community of mostly filamentous

cyanobacteria and heterotrophic bacteria. In the hydrostatic batch environment, resources are heterogeneously distributed, creating ecological niches. The overall biomass concentration is fixed and element cycles are closed. The only incoming energy is light for oxygenic photosynthesis. Photogranule development is therefore dependent on the initially available ingredients, e.g., microbial community structure and carbon and nutrient availability. Photogranule size is limited by the initial carbon availability. By increasing the initial sludge volume, the size of the produced photogranule can be increased. Size is, however, limited by the maximum thickness of the phototrophic layer that has to be sufficiently strong to englobe the biomass. We typically work with 10 ml vials with an inner diameter of 16 mm in which photogranules of up to 10 mm in diameter develop. These granules have a sphere-like morphology. Their outer layer englobes unconsolidated organic matter and mineral particles (**Figure 1.9**a-a'). The mat-like layer gives resistance when a cross section of the photogranule is made and can be peeled away as a coherent layer: it provides structural stability to the 3D structure (**Figure 1.9**b-b'). The phototrophic layer develops by growth and entanglement of gliding filamentous cyanobacteria (**Figure 1.9**c) that form a dense interwoven network (**Figure 1.9**d), reinforced by EPS. There is no visible physical structure in the non-phototrophic interior (**Figure 1.9**b-b'). There must, however, be some kind of structure at the microscale induced by physicochemical gradients that provides ecological niches.

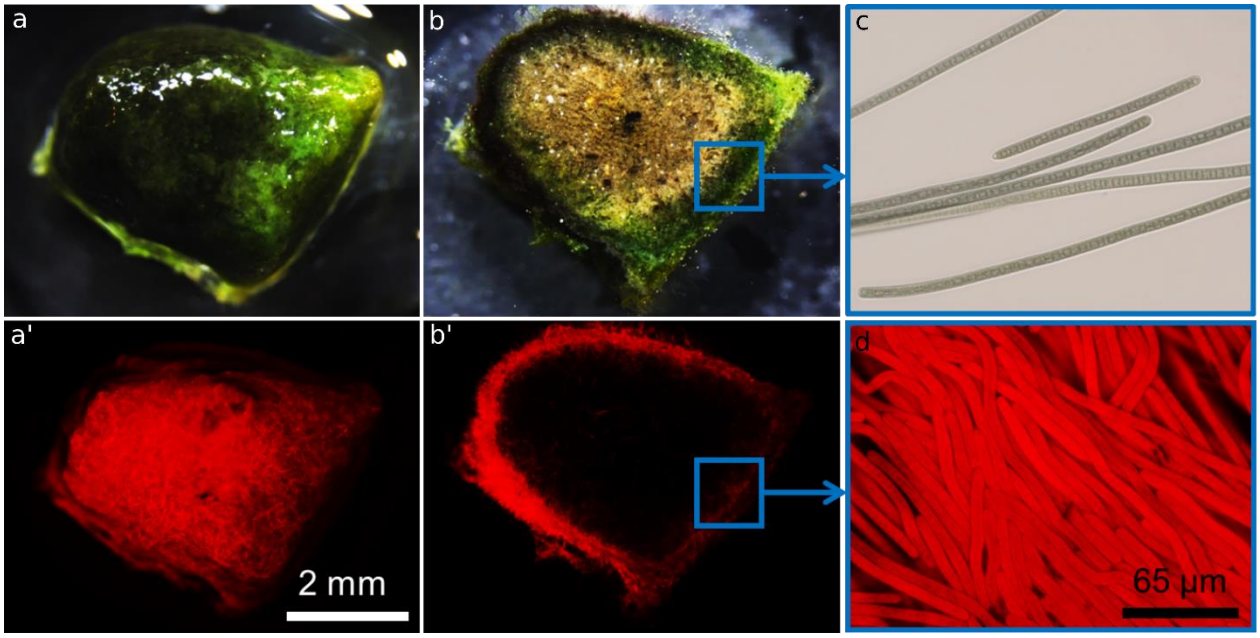

Figure 1.9. Structure of hydrostatically produced photogranules. Top images viewed by white-light microscopy and bottom images by fluorescence microscopy with a phycocyanin filter. (a,a') top view of photogranule; (b,b') cross section of the same photogranule; (c) gliding filamentous cyanobacteria taken from the phototrophic outer layer; (d) section of an outer layer showing the network of filamentous cyanobacteria.

1.3.2 *Comparison between photogranules in nature and the laboratory*

Even though there are differences in production of naturally occurring and laboratory photogranules, production of photogranules in the laboratory may be analogous to the formation of photogranules in natural environments. Lessons from nature may be applied to photogranulation in the laboratory, and *vice versa*. In hydrostatic photogranulation, the ingredients that will form the interior of the photogranule are present from the start, while they may be supplied over time in nature. Organic and mineral particles seem to serve as an immobilization structure

for microorganisms at the onset of hydrostatic photogranulation. From modern microbialites in tropical lagoons, it appears that cyanobacteria can also form part of the interior structure themselves, e.g., by empty cyanobacterial sheaths and other EPS (Sprachta et al., 2001). The syntrophic relationship between photoautotrophs and heterotrophs seems to be important for nutrient-recycling in nutrient-poor environments in which naturally occurring photogranules are found. It is currently unknown whether the benefit of sharing metabolites contributes to the development of the spherical structure. In most studies with axenic isolates from naturally occurring photogranules, granulation could not be demonstrated, except for Castenholz (1967). The phototrophic outer layer that englobes the biomass is formed by a dense network of interwoven gliding filamentous cyanobacteria that are considered to shape the ecosystem. Cyanobacteria have the capability to form complex structures and actively place themselves at a favorable spot. From the literature, it appears that both random and directed gliding movements can result in photogranulation. It is currently unknown what triggers the transformation of activated sludge into photogranules. The relative importance of cyanobacterial growth and gliding motility for hydrostatic photogranulation are also unknown. The primary stimulus for photogranulation may be a change in physicochemical factors that subsequently induce a change in growth and activity of microbial groups. Physicochemical changes can be induced in the system, e.g., increase in pH through carbon depletion by oxygenic photosynthesis, or bought to the system, e.g., change in amount or intensity of light that a cell receives. A physicochemical change may affect photogranulation when it changes for example cyanobacterial gliding motility, interspecies interactions or biomass contraction dynamics.

1.3.3 *Photogranules in biotechnology*

The ultimate interest of acquiring a deeper understanding of the formation of photogranules is their application in biotechnology. The application that has been most extensively studied so far is the use of photogranules in light-driven, aeration-free wastewater treatment (Abouhend et al., 2018; Brockmann et al., 2021; Tiron et al., 2015). Over the past few years, there has been a great deal of interest in the use of phototrophic biomass in aeration-free wastewater treatment, for example in the form of microalgal-bacterial flocs (Gutzeit et al., 2005; Van Den Hende et al., 2014). However, harvesting the floccular biomass from the effluent presented a limitation for its industrial-scale application (Quijano et al., 2017). Activated algae granules can overcome this harvesting barrier (Tiron et al., 2017). They can be effectively separated from the bulk because of their high settleability. A photogranule-based wastewater treatment process in which oxygen is produced saves energy for aeration of the activated sludge process, which is the highest energy demand of modern biological wastewater treatment (Longo et al., 2016). Light energy is, however, needed for oxygenic photosynthesis. Carbon and nitrogen removal rates of an OPG-driven process are consistent with activated sludge removal rates (Abouhend et al., 2018; Arcila and Buitrón, 2017, 2016). Biomass yields are up to three times higher than for activated sludge (Abouhend et al., 2018). Part of the produced biomass is reused in the wastewater treatment process and the excess is often transformed into energy and organic fertilizer by anaerobic digestion. The sustainability of the photogranule process can be improved by valorizing this excess biomass. Photogranules are rich in biopolymers (Abouhend et al., 2019; Ansari et al., 2019; Trebuch et al., 2020), which may serve as thickening or suspending agents, emulsifying agents or cation-chelating compounds depending on their physicochemical characteristics (De Philippis et al., 2001; Kumar et al., 2019). Phycobiliproteins could be used as pigment, antioxidant, animal feed and cosmetics (Galetovic et al., 2020; Grewe and Pulz, 2012). By coupling wastewater treatment

to biomass valorization, photogranules can turn a waste into a resource. Mathematical modelling can contribute to finding the optimum between a stable wastewater treatment process with high removal efficiencies and biomass production with good physicochemical characteristics for product valorization.

1.3.4 *Photogranules in turbulently mixed reactors*

For a biotechnological process, photogranules are suspended in bioreactors. These reactors are typically seeded with mature photogranules to reduce the reactor start-up period (Ansari et al., 2019). In such an open reactor, atmospheric CO_2 diffuses into the bulk and resources are supplied with the incoming (synthetic) wastewater. Photogranules grow in size and number during reactor operation because of the incoming carbon that is fixed in the biomass. Photogranules become larger through cyanobacterial growth, that is visible as concentric rings when looking at a cross section of a granule (**Figure 1.10**). There is a limit to the thickness of the phototrophic layer. For photogranules smaller than 2.5 mm in diameter, light penetrates all the way to the core, producing photogranules that almost entirely consists of phototrophic biomass (**Figure 1.10**) (Abouhend et al., 2019). When the photogranule size exceeds 2.5 mm, a non-phototrophic core develops (**Figure 1.10**). Biomass growth is most likely not limited by carbon availability, because organic matter and CO_2 are constantly supplied with the incoming wastewater and air. Photogranules in bioreactors are up to 5 mm in diameter (Abouhend et al., 2018). Their size is controlled by hydrodynamic shear force. Shear force is believed to be one of the most decisive factors in granule formation under hydrodynamic conditions (Tay et al., 2001). Steps involved in the formation of aggregates include (i) cell-to-cell or cell-to-substratum adhesion by physical forces, (ii) micro-aggregate formation by attractive forces, (iii) structure reinforcement by microbial forces, e.g., EPS production, and (iv) maturation by hydrodynamic shear forces (Liu and Tay, 2002; Sarma et al., 2017). In a fifth step, the biofilm or aggregate may disintegrate.

Light, oxygen, redox and pH gradients across the granule diameter create ecological niches for microbial growth and activities. The distribution of microbial activities across the granule diameter depends on granule size and age, and reactor operating conditions. Several microbial processes have been shown to take place in photogranules. Cyanobacteria and eukaryotic algae in the surface layer fix atmospheric carbon and produce oxygen. Oxygen partially diffuses away in the medium and partially penetrates into the photogranule for degradation of organic matter by heterotrophic bacteria. Heterotrophs use organic compounds as an energy source and supply CO_2 for autotrophic carbon fixation. They live in close association with the cyanobacteria (Ouazaite et al., 2021). Nitrifying bacteria are also found in photogranules. In the presence of oxygen, these bacteria convert ammonium into nitrite and nitrate (Abouhend et al., 2018; Huang et al., 2015; Tiron et al., & Postolache, 2015). The equally present denitrifying bacteria convert nitrite and nitrate into nitrogen gas in the absence of oxygen. Polyphosphate-accumulating bacteria (PAO) remove phosphorous in cycles of anaerobic and aerobic phases (Cai et al., 2019; Trebuch et al., 2020). By adjusting the light intensity, the oxygen concentration in the bulk and therewith the oxygen penetration into the photogranule can be modified (Ouazaite et al., n.d.). This affects the presence and size of an anoxic zone within the photogranule that allows nitrification and denitrification and other redox-depending processes to take place. These results, derived from microscale measurements across the photogranule diameter using microelectrodes coupled to mathematical modeling, are useful to optimize the removal efficiencies and operating costs for wastewater treatment.

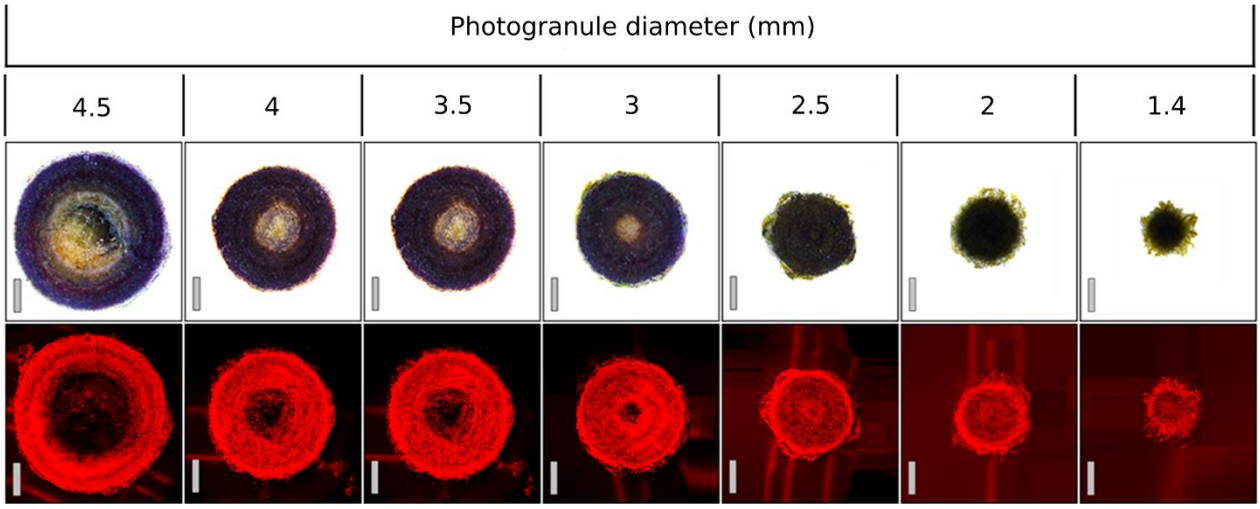

Figure 1.10. Concentric layers in photogranules produced in a bioreactor. Cross section of photogranules viewed by white-light microscopy (top) and fluorescence microscopy with phycocyanin filter (bottom) with increasing granule size. Thickness of the phototrophic layer is limited and a non-phototrophic core develops with increasing granule size. Scale bar for all panels is 1 mm. Figure from Abouhend et al. (2019).

In bioreactors, two distinct photogranule morphologies have been observed: a smooth or sphere-like (**Figure 1.11**a) and a hairy or filamentous morphology (**Figure 1.11**b). These morphologies most likely influence their respective physiological activities and therewith reactor performance (Ouazaite et al., 2021). Because monitoring the development of individual photogranules is challenging in turbulently mixed environment, we do not know whether these morphological forms are successive states. Sphere-like photogranules are typically more calcified, indicating a later developmental stage. I observed a similar development from filamentous to sphere-like photogranules in agitated xenic cyanobacterial cultures. In static cyanobacterial cultures, however, filamentous cyanobacteria have been shown to radiate from the photogranules after a sphere-like photogranule has formed (Biddanda et al., 2015; Brehm et al., 2003; Castenholz, 1967). Obtaining insights into the successive stages of photogranulation from the initiation to formation and eventual disintegration, and the removal activities that are linked to these stages, is important for successful implementation and troubleshooting of OPG-driven biotechnological processes.

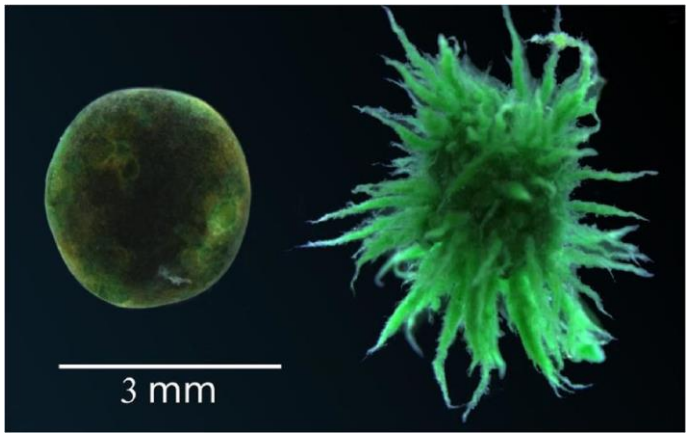

Figure 1.11. Photogranule morphologies produced in a bioreactor viewed by white-light microscopy. (a) Sphere-like and (b) filamentous morphology. Figure from Ouazaite et al. (2020).

1.3.5 *Comparison between hydrostatic and hydrodynamic photogranule production*

We have two laboratory ecosystems in which we can produce photogranules with a similar morphology. Photogranules in turbulently mixed applications are ideal for biotechnological applications, but are less suitable for studying the formation of individual photogranules. Hydrostatic photogranulation is better suited for monitoring the temporal and spatial development of individual photogranules. Ecological principles of photogranulation acquired from hydrostatic batch cultivations may be applied to control the formation and maintenance of photogranules in bioreactors. Even though photogranules look morphologically similar, we not know to what extent they share the mechanisms of formation. Hydrodynamic shear force is most likely a major factor driving photogranulation in turbulently mixed reactors, such as for the formation of aerobic and anaerobic granules. In hydrostatic photogranulation, spatialization originates from an internal driving source, i.e., activities of the microbial community. Individual properties or behavior of filamentous cyanobacteria may therefore be more important in hydrostatic batch cultivations. Gliding motility may promote initial contact with the substratum and movement along the surface (Pratt and Kolter, 1998), cell hydrophobicity (Fattom and Shilo, 1984) and trichome interweaving may contribute to microaggregate formation, and EPS production may contribute to the structural integrity of the granule (Christensen, 1989). The initial community and resources largely determine the outcome, whereas resources and microbes are constantly supplied by the incoming wastewater and air in bioreactors. The amount of biomass that is fixed in the closed batch system therefore increases in bioreactors. Both systems additionally have different gradients of oxygen and redox. Because the ultimate goal beyond my thesis work is to control and stir photogranulation in biotechnological applications, a next logical step would be to investigate how community assembly rules obtained from hydrostatic bath cultivations apply to bioreactors.

1.4 Experimental approaches to monitor photogranulation

There is a lack of understanding of how microbial communities assemble and the spherical structure forms during photogranulation. When we know how photogranules form, we can better understand the requirements for their initiation and ecological role in nature. We could furthermore apply the assembly rules to ecological engineering of photogranules for sustainable bioprocesses, e.g., using a minimal photogranule-forming matrix as eco-chassis to which novel ecosystem functions can be added, such as methane removal or micropollutant conversion. With my thesis, I aim to acquire a deeper understanding of the minimum requirements for photogranulation by studying the photogranulation phenomenon using a microbial ecological approach.

I followed the temporal and spatial development of photogranules by macroscopic observations. The final spherical structure and organization of filamentous cyanobacteria at the exterior of the photogranule were visualized by stereomicroscopy. I used the phycocyanin filter to identify cyanobacteria. Phycocyanin is a pigment protein that is unique to cyanobacteria and gives them their blue-green color. I observed the interior structure and the thickness of the phototrophic layer by making cross sections of the photogranules. Gliding motility of filaments taken from an photogranule was assessed by upright microscopy.

1.4.1 *Temporal and spatial progression of photogranulation*

Several stages that often overlap can be distinguished during photogranule development: compaction, contraction, phototroph enrichment and maturation (**Figure 1.12**) (Kuo-Dahab et al., 2018). The initial activated sludge is brown and consists of unconsolidated, fluffy flocs (**Figure 1.12**, day 0). When transferred into a vial, the biomass immediately starts to settle, resulting in a reduction of the sludge bed height, what we call compaction (**Figure 1.12**, day 0 to 5). There is most likely an anoxic period just after the start, when all oxygen has been consumed and the amount of phototrophs is still low. The biomass further compacts and starts to contract, i.e., it reduces in diameter (**Figure 1.12**, day 5 to15). Phototrophic colonies develop at the irregular biomass surface, and spread out until a mat is formed that covers the entire biomass surface (**Figure 1.12**, day 3 to 8). Gliding filamentous cyanobacteria form a network of interwoven filaments that forms the mat-like outer layer. Filamentous cyanobacteria that are low abundant in the activated sludge are enriched, making up the majority of cells in a mature photogranule community. The biomass jellifies through EPS production and the surface becomes more regular. The density of the biomass increases even further, eventually forming a dense sphere (**Figure 1.12**, day 21). Hydrostatically produced photogranules typically have a smooth surface. The network of entanglement filamentous cyanobacteria embedded in EPS provides structural stability to the photogranule. A mature photogranule is rigid and remains intact when the vial containing the granule is vigorously shaken. The 3D structure remains intact for months to years once it has formed. In **Figure 1.12**, the photogranule sits on the bottom of the vial. This is the developmental trajectory that I most often observed. Biomass can however also start to float because of gas bubbles that get trapped in the cyanobacterial filamentous network.

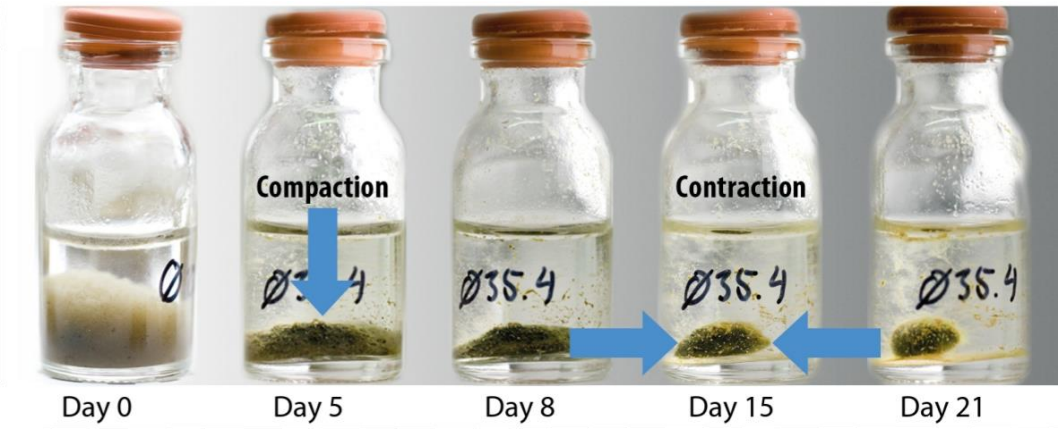

Figure 1.12. Typical course of photogranulation. Temporal progression of the transformation of loose activated sludge into a consolidated photogranule in a 10 ml serum bottle with an outer diameter of 24 mm. Arrows illustrate the terms compaction and contraction. Figure adapted from Milferstedt et al. (2017b).

1.4.2 *Microbial community analysis*

I studied the link between microbial communities and spatial structures with the objective to identify key microbial players in shaping the three-dimensional environment. Molecular methods that I use are based on conserved regions of the 16S and 23S rRNA genes. High-throughput sequencing was applied to assess the microbial community structure. Quantitative polymerase chain reaction (qPCR) was used to quantify bacterial and cyanobacterial gene copy numbers as a proxy for the number of, respectively, bacterial and cyanobacterial cells.

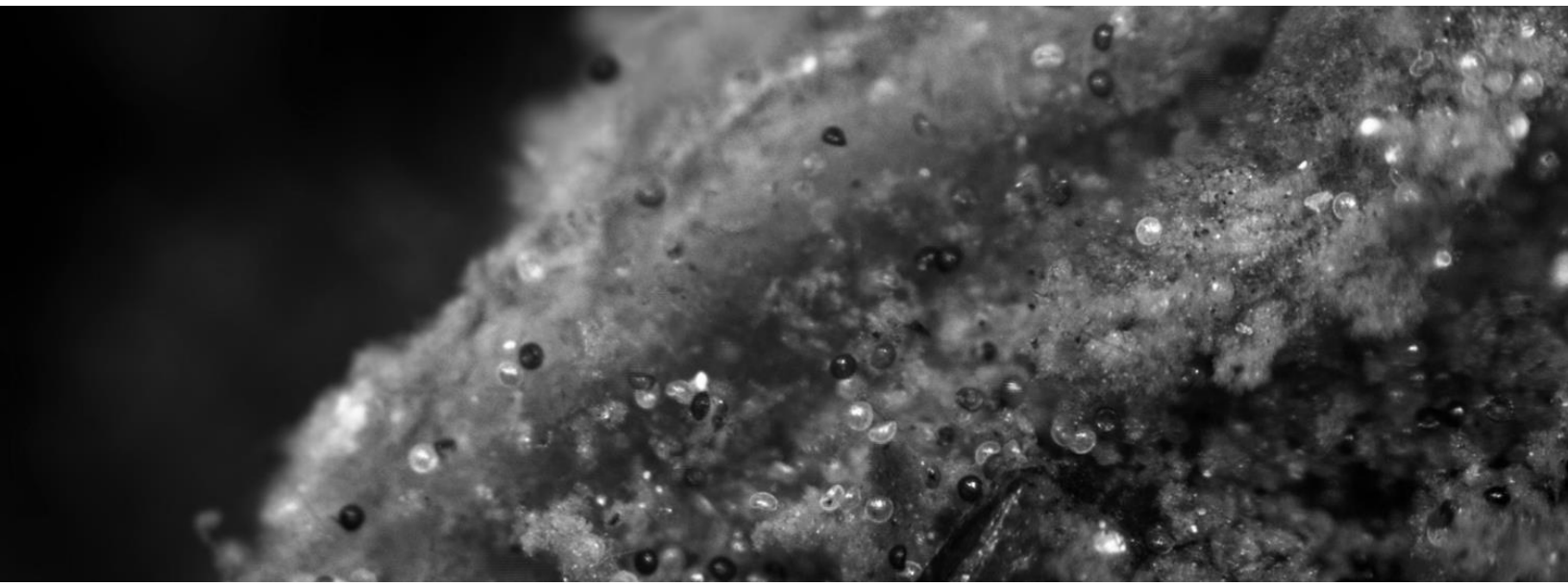

2

Research question, hypotheses and objectives

My research question is: **What are the minimum requirements for photogranulation?**

I hypothesize that the following components are required for photogranulation:

- An **immobilization matrix** for photogranulation;
- A **microbial community** minimally consisting of gliding filamentous cyanobacteria.
- **Physicochemical conditions** that promote cyanobacterial proliferation, gliding motility and EPS synthesis;

I hypothesize that gliding filamentous cyanobacteria can self-aggregate to form photogranules under defined physicochemical conditions. For this, they do not dependent on a pre-existing immobilization structure, because they can form this structure themselves. They are neither dependent on the activities of other microorganisms.

I simplified the activated sludge matrix to find out what is minimally needed to form a photogranule, e.g., by changing activated sludge floc size, availability of nutrients, or eliminating microbial groups from the microbial community. My first objective resulted from the need to compare results between cultivation sets when testing how modified parameters affect photogranulation:

- **Develop a high-throughput imaging assay** to quantify photogranulation (**Chapter 3**).

The untreated control did not produce repetitive results. Instead of only photogranules, a range of spatial structures was formed, making it impossible to monitor the effect of the modifications on photogranulation. I hypothesized that differences in morphotypes are represented at the microbial community level, notably as differences in presence and abundance of gliding filamentous cyanobacteria. This led to the second objective of my thesis:

- **Identify key species in photogranulation** by investigating differences in microbial community structure between morphotypes (**Chapter 4**).

Because photogranulation from activated sludge did not produce repetitive results and I believed that gliding filamentous cyanobacteria possess the trait to form the spherical structure, I wanted to study photogranulation from cyanobacterial strains. I isolated gliding filamentous cyanobacteria from the phototrophic outer layer of mature photogranules as a first step in achieving my last objectives:

- **Asses the granulation ability of cyanobacterial strains** when cultivated in culture medium and added to activated sludge (**Chapter 5**).
- **Increase the number of successfully produced photogranules** per cultivation set by cyanobacterial augmentation (**Chapter 5**).

My broad initial research question on the minimum requirements for photogranulation, i.e., the immobilization structure, physicochemical conditions and microbial community, was narrowed down to the role of the microbial community, with specific focus on the role of gliding filamentous cyanobacteria.

3

Simple time-lapse imaging for quantifying the hydrostatic production of oxygenic photogranules

This chapter has been published as: Joosten, E. D., Hamelin, J., & Milferstedt, K. (2020). Simple Time-lapse Imaging for Quantifying the Hydrostatic Production of Oxygenic Photogranules. Bio-protocol, 10(19), e3784-e3784.

3.1 Abstract

Oxygenic photogranules (OPGs) are dense, three-dimensional aggregates containing a syntrophic, light-driven microbial community. Their temporal and spatial development interests microbial ecologists working at the bioprocess engineering interface, as this knowledge can be used to optimize biotechnological applications, such as wastewater treatment and biomass valorization. The method presented here enables the high-throughput quantification of photogranulation. OPGs are produced from a loose sludge-like microbial matrix in hydrostatic batch cultures exposed to light. This matrix transforms into a consolidated, roughly spherical aggregate over time. Photogranulation is quantified by time-lapse imaging coupled to automated image analysis. This allows studying the development of many OPGs simultaneously and in a fully automated way to systematically test what factors drive photogranulation. The protocol can also be used to quantify other types of (a)biotic aggregation.

3.2 Background

OPGs are dense, roughly spherical aggregates with diameters of several millimeters containing a syntrophic community of heterotrophic and phototrophic microorganisms (Milferstedt et al., 2017). Microbial ecologists study photogranulation to understand what factors drive the formation of the three-dimensional (3D) structure. This knowledge can be applied to steer ecosystem function towards a desired function for biotechnological processes, such as wastewater treatment and the production of value-added products (Abouhend et al., 2018; Quijano et al., 2017). OPGs can be produced from a sludge-like microbial matrix, i.e., activated sludge from the aeration basin of a wastewater treatment plant (Milferstedt et al., 2017; Park, C. & Dolan, 2015). The transformation of this sludge takes place in closed, unagitated vials exposed to light. Over the course of several weeks, the sludge bed compacts (i.e., reduces in height) and contracts (i.e., reduces in diameter) and transforms into one consolidated, 3D aggregate per vial (**Figure 3.1**A). Experimental images are automatically acquired through the bottom of vials at a pre-set interval (**Figure 3.1**B) of multiple replicates simultaneously. Images are treated in ImageJ (Schneider et al., 2012), extending a macro developed for the quantification of naturally occurring OPGs called cryoconite granules (Irvine-Fynn et al., 2010). Dynamics of biomass contraction is calculated and plotted in the software environment R (R core development team, 2019). This protocol enables testing photogranulation in a large number of repetitions, e.g., using different sludge sources or environmental conditions to advance the understanding of photogranulation. The protocol can also be used to quantify other types of (a)biotic aggregation.

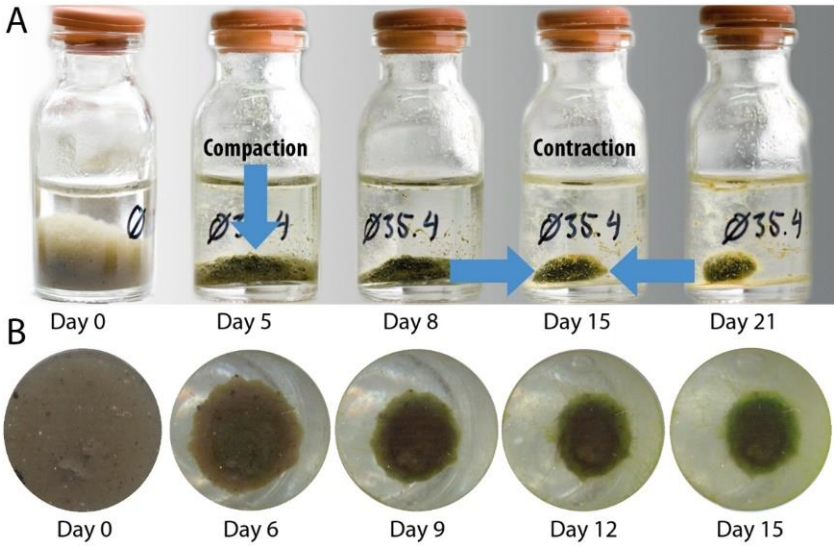

Figure 3.1. Typical course of photogranulation, including compaction and contraction. Note the displayed images are for illustration purposes and were not obtained with the protocol presented here. A. Temporal progression of the transformation of loose activated sludge into a consolidated OPG in a 10 ml serum bottle with an outer diameter of 24 mm (adapted from Milferstedt et al., 2017). Arrows illustrate the terms compaction and contraction; B. Temporal progression of biomass contraction seen through the bottom of one well of a 24-well microplate with an outer diameter of 16 mm.

3.3 Materials and Reagents

1. Fresh activated sludge from the aeration basin of a wastewater treatment plant
2. 0.5-5 ml pipette with tips (Thermo Fisher Scientific, Finnpipette™ F1, catalog number: 4641110N; 5 ml Finntip™, catalog number: 9402030)
3. Grid for aligning and spacing vials on scanner surface. Custom-made dark gray metal grid measuring 30.4 × 22.2 × 0.2 cm (L × W × thickness) (**Figure 3.2**A-B)
4. The grid should be sufficiently low so that it does not shadow the biomass from the side, *e.g.*, it should not be much higher than the thickness of the vial bottom (**Figure 3.3**A-B). The required cut-out where to place the vials can be produced using computer numerical control (CNC) metal milling or 3D printing. You can also make the grid out of other materials, such as paper.
5. Light-impermeable box for covering distance between vials and light source to prevent loss of light and uncontrolled illumination. Home-made cardboard box of the approximate dimensions of 65 × 35 × 65 cm (L × W × H), enclosing the scanner and the lighting device.

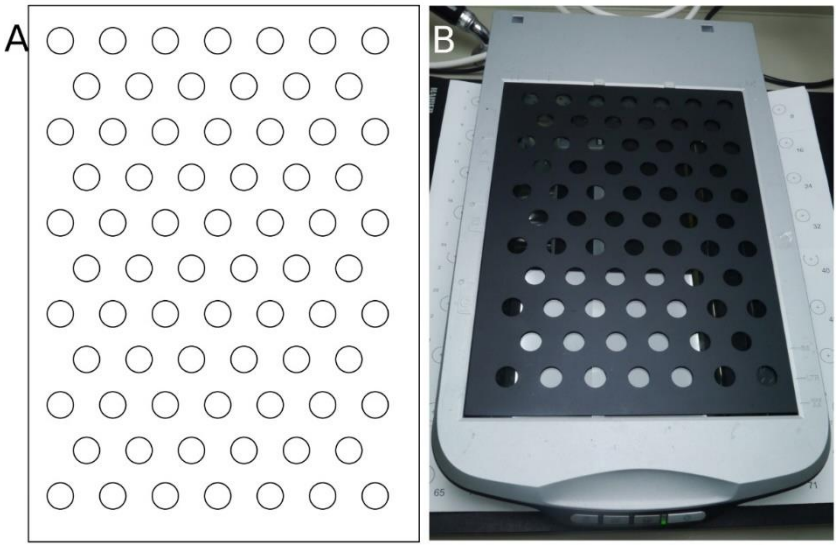

Figure 3.2 Grid. A. Grid design; B. Custom-made dark gray metal grid positioned on top of the scanner.

3.4 Equipment

1. 1 L break resistant bottle with a wide neck for sampling (Fisher Scientific, Gosselin, catalog number: 11728643)
2. 2 L polypropylene beaker for mixing (Thermo Fisher Scientific, Nalgene, catalog number: 1201-2000)
3. 4 ml clear glass vials measuring 15 mm × 45 mm × 8 mm (outer diameter × height × inner diameter) with a screw top for cultivations (Sigma-Aldrich, Supelco, catalog number: 27111) (**Figure 3.3**A)
4. A clear, smooth and flat bottom is critical for the success of this experiment (**Figure 3.3**C). We used glass vials here, and successfully used polystyrene vials previously.
5. Screw caps with a contrasting color to the biomass for image treatment (Agilent Technologies, catalog number: 5183-4305)
6. Magnetic stirrer and stir bar (Bioblock Scientific, AM AMC BBS 3000) to homogenize activated sludge so that differences in sample composition between vials are minimized
7. Holding device for mounting a light source, *e.g.*, copy stand with camera arm (Kaiser, RS1, RA1, catalog number: 205510)
8. Flat light source, *e.g.*, light emitting diode (LED) panel measuring 59.5 × 59.5 (cropped to 30) × 1.06 cm (L × W × H) (Rexel, LEDVANCE, PANEL LED 600, 40W, 6500K, 4000 lm, catalog number: 4058075000582)
9. We used cool white light (6,500 K) for this experiment, but other light temperatures were also successfully tested (*e.g.*, 5,600 and 6,000 K).
10. Photoactive synthetically radiation (PAR) quantum light sensor and display meter system (Skye Instruments Ltd, SKP 215/S 39520, SKP 200 39521)
11. Desktop scanner (Epson, Perfection V500 Photo, model: J251A)

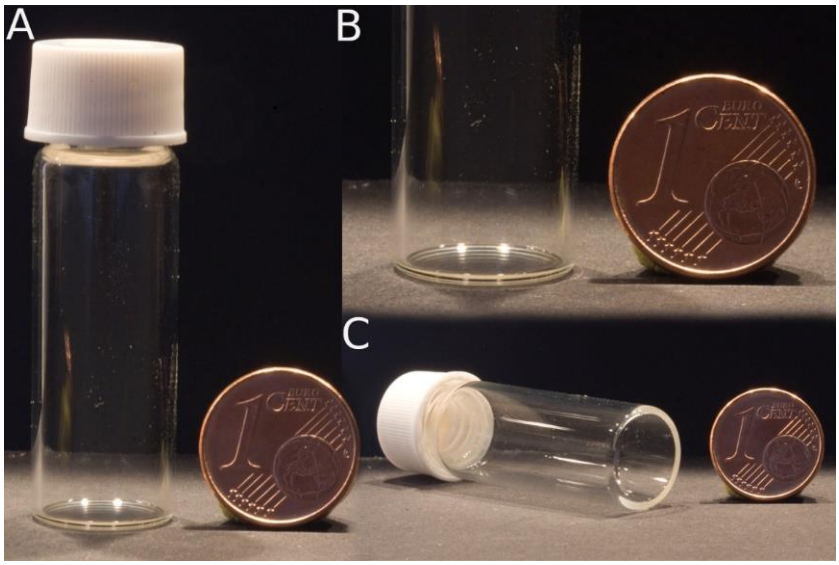

Figure 3.3 Vials. A. Glass vial with screw cap; B. Vial bottom thickness; C. Clear, smooth and flat vial bottom.

3.5 Software

1. Scanner driver allowing time-lapse acquisition of images using a desktop scanner, *e.g.*, VueScan version 9.5.51 (Hamrick Software, https://www.hamrick.com/)
2. Tool to read, write and edit meta information in batches of images, *e.g.*, ExifTool version 11.78 (Phil Harvey, https://exiftool.org/)
3. ImageJ version 1.52a (image processing program) (National Insitutes of Health (NIH), https://imagej.nih.gov/ij/) (Schneider et al., 2012)
   MorphoLibJ plugin to ImageJ version 1.4.0 (collection of mathematical morphology methods and plugins) (INRA-IJPB Modeling and Digital Imaging lab, https://imagej.net/MorphoLibJ) (Legland *et al.*, 2016).
4. R version 3.6.0 (software environment for statistical computing and graphics) (R Core Team, https://www.r-project.org/) (R core development team, 2019)
   exiftoolr package version 0.1.3 (O'Brien, 2020)
   ggplot2 package version 3.2.0 (Wickham, 2016)
   plyr package version 1.8.4 (Wickham, 2011)
   readr package version 1.3.1 (Wickham *et al.*, 2018)

3.6 Procedure

The steps below describe the production of OPGs in hydrostatic batch cultivations and the automated time-lapse acquisition of experimental images. The image analysis follows at "Data analysis".

A. Scanner setup (**Figure 3.4**A-B)

1. Connect a scanner to a computer and install scanner driver, *e.g.*, VueScan.
2. Set scanner settings and save program.
   a. 24-bit RGB image. 800 dots per inch (dpi) resolution yielding a pixel size of 32 µm. This resolution is sufficient to resolve the biological process and prevents the generation of excessively large files.

b. Make sure there is no automatic color correction because this will complicate subsequent data analysis.
c. Select the uncompressed Tagged Image File Format (TIFF) for saving images.
d. Assign TIFF file names, *e.g.*, YY-MM-DD_01+.tif and directory to save acquired scans.
e. Set acquisition interval. Eight hours were sufficient to capture the dynamics of photogranulation. The interval can be increased as the experiment progresses.

3. Take scanner image with a plain white sheet on top of the grid. This will be the background image for data analysis (**Figure 3.5**A).

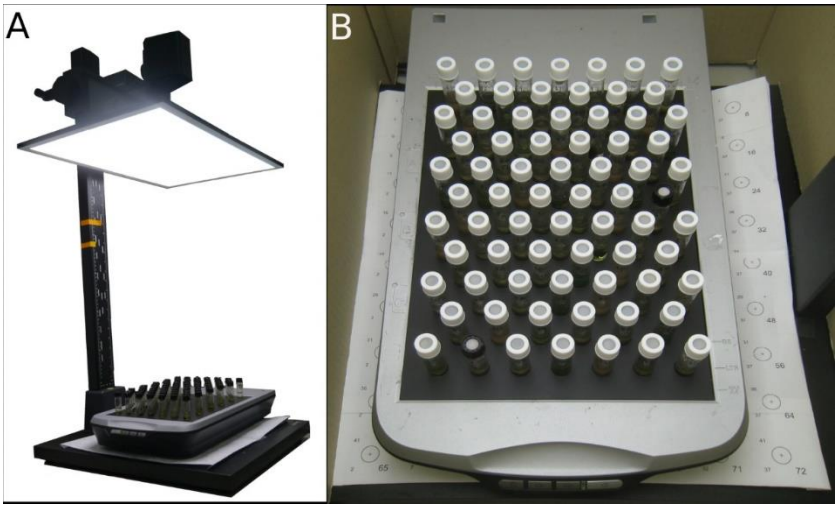

Figure 3.4 Experimental setup. A. Light source and scanner setup (Note the cardboard box is not shown); B. Close-up of scanner setup with vials positioned on the grid.

B. Light source setup (**Figure 3.4**A-B)

1. Install a flat light source above a scanner, preferably using a device that allows adjusting the distance between the light source and vials, for example by connecting it to the camera arm of a copy stand. A flexible distance makes it possible to adjust the light intensity that vials receive and allows easy placement and removal of vials.
2. Light intensity is typically not homogeneously distributed over a LED panel. To ensure that the local light conditions are known, you can map local PAR at different points on the scanner surface, draw a contour map and decide where to place the vials, *e.g.*, along contour lines of similar light intensities. You can design a grid with circles that indicate where to place the vials (**Figure 3.2**A). You can print the grid on paper, cut out the circles and place it on top of the desktop scanner for positioning the vials. If you want to use the grid regularly, you can make it out of a more solid material, *e.g.*, metal (**Figure 3.2**B) using CNC metal milling or 3D printing.
3. Adjust the distance between the vials and light source such that the light intensity at the vial positions corresponds to approximately 60 $\mu mol \cdot m^{2} \cdot s^{-1}$ PAR. This can be measured using a PAR quantum light sensor.

C. Activated sludge sampling and characterization

1. Sample 200 ml of activated sludge from the aeration basin of a wastewater treatment plant. This volume is largely sufficient for an experiment using 72 vials inoculated with 1.5 ml of activated sludge each, as described in the following. The sample volume needs to be

adapted if you are interested in characterizing the activated sludge, *e.g.*, total and volatile solids, chemical oxygen demand, nitrogen, phosphorus, pH, chlorophyll, microbial community.
2. It is useful to have available the measurement of total solids. This can be used to adjust the sludge concentration to a value comparable between experiments. We typically run an experiment with a concentration between 4 and 5 g/L of activated sludge.

D. Vial preparation and placement

1. Keep activated sludge in suspension upon arrival at the lab, *e.g.*, using a magnetic stirrer. *Note: Sludge can be stored at 4 °C when it cannot be used directly, but we recommend to use fresh activated sludge.*
2. Pipette 1.5 ml well-mixed activated sludge into 4 ml vials. Close vials with a screw cap. Our typical incubation set contains 72 vials.
3. Place vials unagitated at the assigned areas on top of desktop scanner under constant light illumination at ambient room temperature (22-26 °C) (**Figure 3.4**A-B).
4. Place a light-impermeable box around the scanner and light source to limit loss of light and uncontrolled illumination of your samples.

E. Vial incubation and time-lapse imaging

1. Start scanner software to take an image of the bottom of the vials at the desired interval. Make sure the scanner takes an image at time 0 and that images are taken at indicated intervals.
2. The unconsolidated sludge transforms into one OPG per vial that is typically situated at the bottom of the vial, unless it starts floating due to attached gas bubbles. Run the experiment until mature OPGs have been formed. A mature OPG is roughly spherical and remains its shape after vigorous shaking. Under the given experimental conditions, photogranulation can be expected to occur between three to six weeks. The experimental conditions, *e.g.*, light intensity and sludge characteristics, may influence the time needed for photogranulation.
3. Take a final scan before removing the vials from the scanner.

F. Photogranulation success

1. Note down whether OPGs are sitting on the bottom or floating for image analysis.
2. Take camera images of OPGs to remember later what they looked like.
3. Shake vials vigorously and note down in which vials a successful OPG has been formed. Photogranulation success is the percentage of successful OPGs among the total incubated vials.
4. Characterize OPGs depending on the factors you are interested in, *e.g.*, physicochemical parameters, microbial community.

3.7 Data analysis

For data analysis, we show the results of an experiment performed with 72 vials of a volume of 4 ml using two sludge sources, therefore having 36 replicates per condition. Some files are created as preparation for automatic data treatment (Procedures A-B). Experimental time-lapse images are treated in ImageJ (Schneider et al., 2012) using particle size analysis to measure particle characteristics including surface area (Procedures C-D). The surface area is subsequently transformed to equivalent diameters in the software environment R (R core development team,

2019) and plotted over time. The decrease in equivalent diameter per sample is a measure for proceeding photogranulation (Procedure E). Text in green are comments from the authors, text in red require user input, text in blue show files that will be imported into R (Procedure E).

A. Experimental conditions

1. Create a text file (experimental_conditions.txt) containing the vial positions and their respective experimental conditions in three columns, *i.e.*, Location, ExpCondition, ExpID. You can find an example of this file at https://doi.org/10.5281/zenodo.3938457.

B. Extract acquisition date/ time and remove scan resolution

1. The Exchangeable Image File (EXIF) data of the scanner images contains the filename and the creation date of the image. Both need to be available in a separate file for subsequent plotting of the data. You can automatically extract filename (*e.g.*, 2018-03-14-01.tif) and creation date/ time (*e.g.*, 2018:03:14 16:47:36) from EXIF data using the R script below.
2. The EXIF data may also contain the scan resolution. This resolution in dpi interferes with the particle size quantification using ImageJ. Remove scan resolution from EXIF data running ExifTool from within R so that ImageJ does not use dpi as a scaling factor. You can later assign a measurement unit to the images in ImageJ.
    a. Install ExifTool
    b. Open a new R script in an R editor, for example RStudio, by clicking on ‘file’, ‘new file’, ‘R script’.
    c. Copy the following script into the source window. Text in red require user input and adaptations.

```
##Packages --------------------------------------

require(exiftoolr) #(O'Brien, 2020)


##Working directory -----------------------------------

rm(list=ls())

directory <- ("/path-to-directory/")

setwd(directory)


##Extract acquisition date/ time and remove scan resolution ------------------
--------------------

image.vec <- list.files(directory, pattern = ".tif") #Generates a list of all
*.tif files in the directory

exif.images <- exif_read(path = image.vec) #Reads the EXIF data from the
specified *.tif images

image.data <- cbind(exif.images$FileName, exif.images$CreateDate)

colnames(image.data) <- c("Name", "DateTime")

write.csv(image.data, file = "image_acquisition.csv", quote = F, row.names = F)
#Writes the tags file name and creation date to a separate file to be used
```

```
later. You can find an example of this file at https://doi.org/10.5281/zenodo.3938457.

exiftool_cmd <- paste("exiftool -ResolutionUnit= -XResolution= -YResolution= ", "*.tif",sep='') #Defines the ExifTool command to erase the Resolution data in the EXIF data of all images with the *.tif extension

system(exiftool_cmd) #Executes ExifTool from within R. You can also run ExifTool outside R. Original scanner images are automatically saved as *.tif_original by ExifTool. Created images without scan resolution (*.tif) will be used for subsequent data analysis in this protocol.
```

The method presented below shows an example of how to define and measure regions of interest. ImageJ macros are adapted from Irvine-Fynn *et al.* (2010) who quantified granule geometry of cryoconite, microbial aggregates that share similarities with OPGs, under laboratory conditions. Extracting information from experimental time-lapse images is a means to an end and not the main interest of this protocol. Other methods may be used equally well to obtain particle characteristics, including area and X-, Y-coordinates.

C. Marker image

1. Here we convert the background image (**Figure 3.5**A) into a marker image (**Figure 3.5**B). The marker image will be used to determine the X-, Y-coordinates of areas that could possibly contain particles, *i.e.*, the circles that vials occupy. These data are used to assign measured particle characteristics to unique samples and their respective experimental conditions (Procedure E).
    a. Open an empty macro in ImageJ by clicking on ‘plugins’, ‘new’, ‘macro’.
    b. Copy the following script into the macro.txt window.

```
jobdirectory = getDirectory("Please choose a directory for saving result files and the marker image.");

waitForUser("Please open the background image. Then click ok.");

backgroundimage = getTitle();

run("Split Channels");

selectImage(backgroundimage + " (red)");

close();

selectImage(backgroundimage + " (green)");

close();

selectImage(backgroundimage + " (blue)");

//Converts RGB to grayscale image. Retains only the channel which presents most contrast between the areas on which vials are placed (white) and the grid (black).

run("Invert");

//Vial areas now appear black and the grid white.

setAutoThreshold("Default");

run("Threshold...");

waitForUser("Please set the threshold manually. Then press OK.");
```

```
setOption("BlackBackground", false);

run("Convert to Mask");

run("Close");

//Creates binary image from grayscale image: choose and apply cut-off value to divide image into foreground, i.e., vial areas, and background, i.e., grid. This works well when the grid is darker than the biomass. Otherwise you will have to setOption ("Black background", true).

run("Fill Holes (Binary/Gray)");

//Fills holes in areas occupied by vials to achieve a solid area (Legland et al., 2016).

run("Morphological Filters", "operation=Opening element=Disk radius=10");

//Removes isolated pixels and breaks connections between areas occupied by vials and the grid so that it becomes less likely that the grid is accidentally considered part of the vial area.

run("Morphological Filters", "operation=Erosion element=Disk radius=35");

      //Decreases the size of detected particles to exclude areas that are not part of the biomass, e.g., a ring corresponding to a vial that connects the biomass to the grid, resulting in a larger biomass particle than it actually is.

      //Note: You may adjust the parameter disk radius depending on your images and experiment.

saveAs("Tiff", jobdirectory + "marker.tif");

            run("Set Measurements...", "area centroid fit shape display redirect=None decimal=3");

//Specifies which measurements are recorded.

run("Analyze Particles...", " show=Overlay display exclude");

//Generates a result table containing information about each particle in the image, including a running number to label detected particles (i.e., the area that a vial occupies), the particle area and the centroid X-, Y-coordinates of the particles (Figure 3.6). It furthermore overlays the particle labels with the marker image to visually relate the particle characteristics in the table to the detected particles on the image.

saveAs("Results", jobdirectory + "results_marker.csv");

//You can find an example of this file at https://doi.org/10.5281/zenodo.3938457.
```

c. Run the macro by clicking on 'macros', 'run macro'. During execution of the macro, manually select the output directory to save the created marker image and open the background image. You can use your own background image or run a demo with the image that can be downloaded from https://doi.org/10.5281/zenodo.3938457.
d. Take a screenshot of the resulting marker image with particle labels overlaid that is not automatically saved running the macro (**Figure 3.5**B). We numbered vial locations 1 to 72 from top left to bottom right. The order in which ImageJ detected

the areas occupied by vials on the marker image does not necessarily correspond to this numbering as the particle analyzer in ImageJ scans the image until it finds an edge of an object, which becomes particle 1 (see number 1 in **Figure 3.5**B), which in this case also corresponds to location 1 according to our numbering. In the R script (Procedure E1b), we use the screenshot to relate ImageJ particle numbers (lines in result table) to our vial locations.

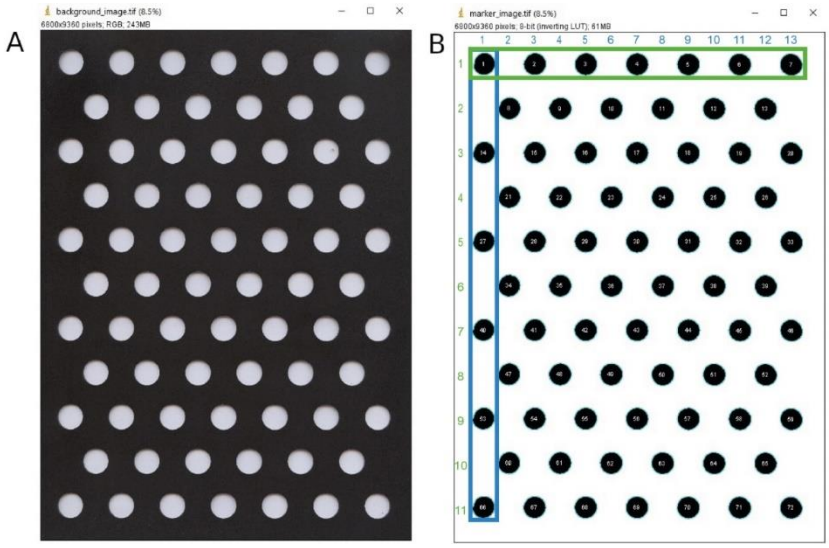

Figure 3.5 Marker image created from background image. Screenshots of A. the background image, that is converted into B. the marker image, here displayed with the particle label overlay. The images that are saved in the macro do not have the headers and overlay as displayed in this figure. Columns are indicated in blue and rows in green.

Results

File Edit Font Results

	Label	Area	X	Y	Major	Minor	Angle	Circ.	AR	Round	Solidity
1	marker_image.tif	123575	550.395	581.911	409.002	384.693	59.160	0.881	1.063	0.941	0.992
2	marker_image.tif	127173	1479.350	583.627	409.309	395.597	41.282	0.891	1.035	0.966	0.993
3	marker_image.tif	128059	2416.586	584.535	408.102	399.532	34.467	0.893	1.021	0.979	0.994
4	marker_image.tif	128921	3356.865	585.888	407.679	402.638	10.264	0.892	1.013	0.988	0.993
5	marker_image.tif	129140	4299.750	588.106	409.149	401.873	169.507	0.895	1.018	0.982	0.994
6	marker_image.tif	129302	5242.654	590.593	411.063	400.505	159.725	0.890	1.026	0.974	0.993
7	marker_image.tif	128118	6185.716	594.240	412.684	395.278	144.008	0.882	1.044	0.958	0.991
8	marker_image.tif	125235	1012.232	1396.957	409.081	389.786	51.402	0.887	1.050	0.953	0.993
9	marker_image.tif	127522	1946.099	1397.412	408.748	397.228	39.538	0.888	1.029	0.972	0.993
10	marker_image.tif	128929	2885.779	1398.364	408.507	401.847	21.075	0.888	1.017	0.984	0.993
11	marker_image.tif	129452	3827.864	1399.979	409.390	402.607	176.597	0.892	1.017	0.983	0.994
12	marker_image.tif	129192	4772.122	1402.374	410.199	401.007	164.326	0.892	1.023	0.978	0.994
13	marker_image.tif	129451	5716.275	1404.482	412.253	399.808	155.670	0.893	1.031	0.970	0.993
14	marker_image.tif	124386	544.065	2208.516	409.310	386.927	51.105	0.880	1.058	0.945	0.992

Figure 3.6 Result table of marker image. Screenshot of the result table showing characteristics of the first 15 out of 72 particles of the marker. This is not the result table that is saved in the macro, which is a comma-separated value (csv) file.

D. Experimental time-lapse images

1. Here we convert scanner color images to black and white binary images, displaying biomass particles in black and the grid in white. Characteristics of each particle will be saved in a corresponding result table. The grid for positioning the vials will be automatically removed from the images. Possible erratic particles that are not part of the OPGs are

equally removed during the process. The macro includes a manual thresholding step which is relatively time-consuming, but automatic thresholding may not always result in particles that reflect well the visual impression on the scanner images. In theory, we obtain 72 biomass particles per image for an incubation set of 72 vials. We acquired experimental images over a period of six weeks, resulting in 110 color images, each of a size of 182 MB. An image that is taken halfway through the experiment is shown as an example in **Figure 3.7**A.

a. An image containing the background (*i.e.*, areas that cannot possibly contain biomass, for example the grid) is required. This image needs to be a grayscale image in which the grid is white and the areas potentially containing particles during the experiment are black. In the simplest case, the image could be the marker image generated in Procedure C, or, for improved particle detection, a manually curated image based on either the background or an experimental image. During manual curation, the area available for photogranulation may be redrawn as disks with the inner diameter of the vials. A foreground limited to the potential areas where particles can be detected avoids artefacts interfering with image detection that can be caused by reflections of the vial walls or shadowing effects of the grid during scanning.
b. Open an empty macro in ImageJ by clicking on ‘plugins’, ‘new’, ‘macro’.
c. Copy the following script into the macro.txt window.

```
setBatchMode(false);
//Enters or remains in batch mode and hide active images during macro execution.
function action(input, output, filename){
                                                                    open(input        +
filename);
            jobname = getTitle();
jobnamemod = indexOf(jobname, ".");
            jobname = substring(jobname, 0, jobnamemod);
//The file paths and filenames entered when starting the macro are converted to
variables that become useable to the commands where they are used.
      run("Split Channels");
            selectImage(jobname + ".tif (blue)");
close();
            selectImage(jobname + ".tif (green)");
            close();
            selectImage(jobname + ".tif (red)");
            red_image = getTitle();
//Converts RGB to grayscale image. Retains only the channel which presents most
contrast between the areas on which vials are placed (white) and the grid
(black).
            open(path);
```

```
//Opens the grid image (e.g., the marker image) selected in Procedure D1a using the file specified below.

//Vial areas now appear blackish and the grid whitish.

grid = getTitle();

      imageCalculator("Add create", red_image, grid);

close("\\Others");

//Making grid appear as true white so that it will be detected as background in the subsequent binarization step.

      run("Set Scale...", "distance=0 known=0 pixel=1 unit=pixel");

//Removes spatial scale of active image so that measurement results (e.g., area measurements) have the unit pixel.

      run("Threshold...");

            waitForUser("Please set the threshold manually. Then press OK, or cancel to exit macro");

setOption("BlackBackground", false);

            run("Convert to Mask");

selectWindow("Threshold");

            run("Close");

//Creates binary image from grayscale image: choose and apply cut-off value to divide image into foreground, i.e., vial areas, and background, i.e., grid. Define your own criteria and try to treat each image of your dataset in the same way.

//Note: This can be tricky because we normally do not find a threshold that works ideally for every particle on an image. We recommend testing a small subset (e.g., first, middle and last images) to get an idea of what works well.

run("Fill Holes (Binary/Gray)");

//Fills holes in the areas occupied by vials to achieve a solid area (Legland et al., 2016).

//Note: This may fill up entire vial area when a biomass particle is surrounded by a ring corresponding to a vial. If this happens, you can reduce the size of the respective particle on the marker image using for example image editor Gimp and run the macro again (see also Procedure D1a).

      run("Morphological Filters", "operation=Opening element=Disk radius=10");

close("\\Others");

//Removes isolated pixels and breaks connections between areas occupied by vials and the grid so that it becomes less likely that the grid is accidentally considered part of the vial area.

            mask_image = getTitle();

//Created image becomes mask image.
```

```
            run("Morphological Filters", "operation=Erosion element=Disk
radius=40");
            marker_image = getTitle();
      //Drastically decreases the size of detected particles on the mask image
to create an image that will be used for morphological reconstruction.
      //Note: Images of small granules may be removed when the disk radius is
too large, you may adjust the parameter disk radius depending on your images
and experiment.
      print("The marker image name is " + marker_image);
            print("The mask image name is " + mask_image);
//Prints active marker and mask images.
run("Morphological Reconstruction", "marker=["+marker_image+"]
mask=["+mask_image+"] type=[By Dilation] connectivity=4");
//Keeps particles from the mask image that overlap with at least one pixel on
the marker image and remove other pixels. This step assures that only particles
are retained that overlap with vial areas and that possible erratic particles
that are not part of OPGs are removed.
      run("Set Measurements...", "area centroid fit shape display redirect=None
decimal=3");
      rename(jobname);
//Specifies which measurements are recorded.
      run("Analyze Particles...", "size=0-Infinity circularity=0.00-1.00
show=[Overlay Outlines] display exclude");
//Generates result table (see explanation at Procedure C).
            save(output + jobname + ".final.tif");
            close();
      saveAs("Results", output+ jobname + "_results.csv" );
run("Clear Results");
      selectWindow("Log");
            run("Close All");
}
//Erases any previous measurement results.
input = getDirectory("Choose an input directory with the raw images, please.");
output = getDirectory("Choose an output directory for result images and tables,
please.");
waitForUser("Please open the grid image. Then click ok.");
//Selects the grid image (e.g., the marker image) selected in Procedure D1a.
This image allows the removal of the grid from the scanner images.
grid = getTitle();
```

```
dir = getDirectory("image");

path = dir+grid;

close();

//Define input directory with experimental images and output directory to save
created images. Open the grid image selected in Procedure D1a. In the chronology
of the script, results from these commands will be displayed once when starting
the macro.

list = getFileList(input);

for (i = 0; i < list.length; i++)

            action(input, output, list[i]);

setBatchMode(false);

//Definition of a loop structure that will execute the macro function as many
times as there are images found in the input directory.
```

d. Run the macro by clicking on ‘macros’, ‘run macro’. During execution of the macro, manually select the input directory with experimental images, output directory to save created images and open the grid image selected in Procedure D1a. You can use your own experimental images and grid image or run a demo with exemplary images that can be downloaded from https://doi.org/10.5281/zenodo.3938457. Actions are automatically repeated for all images in the input directory.
   Note: Make sure to not have unrelated files in the folder as otherwise ImageJ attempts to treat them as images.
e. Manually check whether the particles on the obtained images (**Figure 3.7**B) correspond to what you visually detect on the raw images.
   Note: This sanity check is important because the automated analysis is supposed to mimic and automate the visual inspection but is not infallible. You can create a series of thumbnails by rescaling the original scanner images to a reduced size to browse more easily through the images.
f. Concatenate (combine) result tables into one csv file to simplify the analysis.
g. Open a new R script in an R editor, for example RStudio (R core development team, 2019), by clicking on ‘file’, ‘new file’, ‘R script’.
h. Copy the following script into the source window. Text in red require user input and adaptations.

```
##Packages ------------------------------------

require(plyr) #(Wickham, 2011)

require(readr) #(Wickham et al., 2018)


##Working directory ---------------------------------------

rm(list=ls())

directory <- ("/path-to-directory/")

setwd(directory)
```

```
##Concatenate result tables ---------------------------------------

results.df <- list.files(path = directory, pattern = "*.csv", full.names = T)
#Generates a list of all *.csv files in the directory

results.df <- ldply(results.df, read_csv) #Combines result tables of all images
into a single data frame

colnames(results.df)[1] <- "ObjNum" #Assigns name ObjNum to first column

write.csv(results.df, file = "results_scanner_images.csv", quote = F, row.names
= F) #Writes result tables of all images to a separate file to be used later.
You can find an example of this file at https://doi.org/10.5281/zenodo.3938457.
```

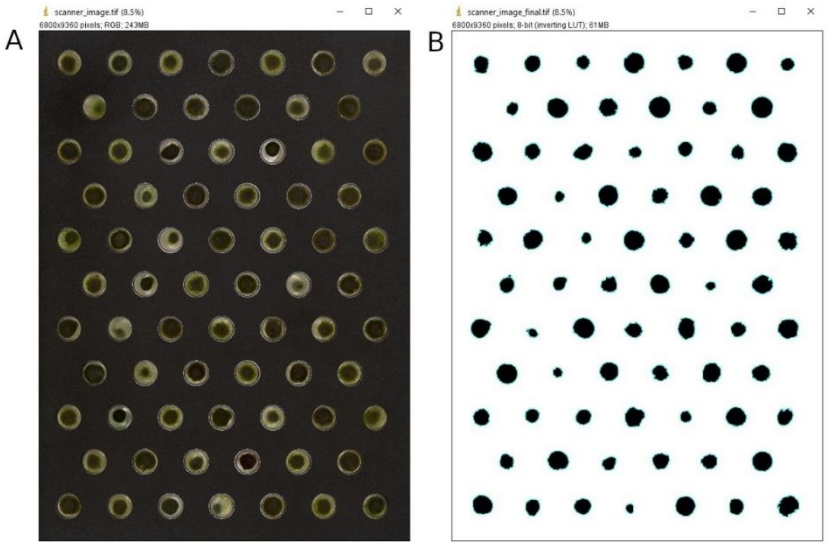

Figure 3.7 Result image created from scanner image. Screenshots of A. a scanner image taken halfway through the experiment, that is converted into B. the result image for which the particle characteristics are determined. The images show particles contracted to varying degrees for the two sludge sources. The images that are saved in the macro do not have the headers as displayed in this figure.

E. Quantification of photogranulation

1. The experimental results are now imported into the software environment R (R core development team, 2019). The challenge is to automatically convert the particle characterizations done per image into one time-series per vial. The steps of the R script are as follows:
   - Calculate average X-, Y-coordinates of vial areas identified on the marker image (**Figure 3.5**B);
   - Assign experimental time to all experimentally measured particles per image by adding a column with experimental time to the particle data obtained with ImageJ. This facilitates the plotting to temporal dynamics;
   - Identify particles from a vial at a specific physical location on each image using the X- and Y-coordinates of vial areas. Relate particles to their location by assigning a location number and match them to the appropriate experimental conditions;
   - Transform the detected surface area of particles into equivalent diameters;
   - Plot the average decrease in particle diameter per experimental condition over time.

a. Open a new R script in an R editor, for example RStudio, by clicking on ‘file, ‘new file’, ‘R script’.
b. Copy the following script into the source window. Text in red require user input and adaptations.

```
##Packages ------------------------------------

require(plyr) #(Wickham, 2011)

require(ggplot2) #(Wickham, 2016)


##Working directory ---------------------------------------

rm(list=ls())

directory <- ("/path-to-directory/")

setwd(directory)


##Start time ----------------------------------------

start.time <- c("2018:03:14 17:51:19")

#Manually enter start date/ time of the first image of the experiment. Experimental time will be calculated based on this time point, using the acquisition time of the scanner images.


##Scaling factor ------------------------------------

scaling.factor <- 475.417/1.5 #pixels/cm

#Manually enter the scale of the images, i.e., number of pixels to cover the diameter of a vial. This value can be easily measured in ImageJ.


##Margin -------------------------------------

margin.vial <- 212

#Manually enter average number of pixels between the center and edges of a particle as measured in ImageJ, typically the inner radius of the vials in pixel.


##Files to be imported -----------------------------------

#You can run a demo with the files presented at https://doi.org/10.5281/zenodo.3938457.

coordinates.name <- "results_marker.csv" #Information about each particle on marker image (generated using ImageJ).

raw.data.name <- "results_scanner_images.csv" #Joined result tables of scanner images (generated using ImageJ).

acquisition.time.name <- "image_acquisition.csv" #Filename and creation date of scanner images (generated using ExifTool from within R).
```

```
experimental.condition.name  <-  "experimental_conditions.txt"  #Experimental conditions per sample (manually generated).


##Loading files -------------------------------------

coordinates <- read.csv(coordinates.name, header=T, as.is =T)

raw.data <- read.csv(raw.data.name, header = T, as.is = T)

acquisition.time <- read.csv(acquisition.time.name, header = T, as.is = T)

experimental.condition <- read.delim(experimental.condition.name, header = T, as.is = T)


####Calculate average X-, Y-coordinates of vial areas identified on the marker image (Figure 3.5B).


##Average X-, Y-coordinates of vial areas ------------------------------------------

column.1 <- c(1,14,27,40,53,66) #Manually enter which particle label on the marker screenshot corresponds to which column, as indicated in blue (Figure 3.5B). The grid consists of columns alternating in starting position and size, e.g., the first particle detected corresponds to the first particle in the first column of the scanner grid, the fourteenth particle detected is situated on the grid in column 1, row 3, etc.

column.2 <- c(8,21,34,47,60)

column.3 <- c(2,15,28,41,54,67)

column.4 <- c(9,22,35,48,61)

column.5 <- c(3,16,29,42,55,68)

column.6 <- c(10,23,36,49,62)

column.7 <- c(4,17,30,43,56,69)

column.8 <- c(11,24,37,50,63)

column.9 <- c(5,18,31,44,57,70)

column.10 <- c(12,25,38,51,64)

column.11 <- c(6,19,32,45,58,71)

column.12 <- c(13,26,39,52,65)

column.13 <- c(7,20,33,46,59,72)


row.1 <- c(1,2,3,4,5,6,7) #Manually enter which particle label on the marker screenshot corresponds to which row, as indicated in green (Figure 3.5B). The grid consists of rows alternating in starting position and size, e.g., the first particle detected corresponds to the most left particle in the first row of the grid, etc.
```

```
row.2 <- c(8,9,10,11,12,13)
row.3 <- c(14,15,16,17,18,19,20)
row.4 <- c(21,22,23,24,25,26)
row.5 <- c(27,28,29,30,31,32,33)
row.6 <- c(34,35,36,37,38,39)
row.7 <- c(40,41,42,43,44,45,46)
row.8 <- c(47,48,49,50,51,52)
row.9 <- c(53,54,55,56,57,58,59)
row.10 <- c(60,61,62,63,64,65)
row.11 <- c(66,67,68,69,70,71,72)

pos.names <- c(row.1, row.2, row.3, row.4, row.5, row.6, row.7, row.8, row.9,
row.10, row.11)
#Order of particle numbers from top left to bottom right.

average.x.1 <- mean(coordinates$X[coordinates$X.1 %in% column.1])
average.x.2 <- mean(coordinates$X[coordinates$X.1 %in% column.2])
average.x.3 <- mean(coordinates$X[coordinates$X.1 %in% column.3])
average.x.4 <- mean(coordinates$X[coordinates$X.1 %in% column.4])
average.x.5 <- mean(coordinates$X[coordinates$X.1 %in% column.5])
average.x.6 <- mean(coordinates$X[coordinates$X.1 %in% column.6])
average.x.7 <- mean(coordinates$X[coordinates$X.1 %in% column.7])
average.x.8 <- mean(coordinates$X[coordinates$X.1 %in% column.8])
average.x.9 <- mean(coordinates$X[coordinates$X.1 %in% column.9])
average.x.10 <- mean(coordinates$X[coordinates$X.1 %in% column.10])
average.x.11 <- mean(coordinates$X[coordinates$X.1 %in% column.11])
average.x.12 <- mean(coordinates$X[coordinates$X.1 %in% column.12])
average.x.13 <- mean(coordinates$X[coordinates$X.1 %in% column.13])
#Calculates average X-coordinates.

average.y.1 <- mean(coordinates$Y[coordinates$X.1 %in% row.1])
average.y.2 <- mean(coordinates$Y[coordinates$X.1 %in% row.2])
average.y.3 <- mean(coordinates$Y[coordinates$X.1 %in% row.3])
average.y.4 <- mean(coordinates$Y[coordinates$X.1 %in% row.4])
average.y.5 <- mean(coordinates$Y[coordinates$X.1 %in% row.5])
```

```
average.y.6 <- mean(coordinates$Y[coordinates$X.1 %in% row.6])

average.y.7 <- mean(coordinates$Y[coordinates$X.1 %in% row.7])

average.y.8 <- mean(coordinates$Y[coordinates$X.1 %in% row.8])

average.y.9 <- mean(coordinates$Y[coordinates$X.1 %in% row.9])

average.y.10 <- mean(coordinates$Y[coordinates$X.1 %in% row.10])

average.y.11 <- mean(coordinates$Y[coordinates$X.1 %in% row.11])

#Calculates average Y-coordinates.


average.x.a    <-c(average.x.1,    average.x.3,    average.x.5,    average.x.7,
average.x.9, average.x.11, average.x.13)

average.x.b    <-    c(average.x.2,    average.x.4,    average.x.6,    average.x.8,
average.x.10, average.x.12)

#Calculates average Y-coordinates of rows having the same X-coordinate.

average.y.a    <-    c(average.y.1,    average.y.3,    average.y.5,    average.y.7,
average.y.9, average.y.11)

average.y.b    <-    c(average.y.2,    average.y.4,    average.y.6,    average.y.8,
average.y.10)

#Calculates average X-coordinates of rows having the same Y-coordinate.

first.half <- expand.grid(average.x.a, average.y.a)

second.half <- expand.grid(average.x.b, average.y.b)

#Couples X-, Y-coordinates for both a and b.

average.coordinates <- rbind(first.half, second.half)

colnames(average.coordinates) <- c("X","Y")

#Combines first.half and second.half by rows.

average.coordinates     <-     average.coordinates[order(average.coordinates$Y,
average.coordinates$X),]

#Arranges coordinates to be in the same order as the particle numbers that can
be found on the marker screenshot.

average.coordinates <- cbind(average.coordinates, pos.names, 1:72)

colnames(average.coordinates) <- c("X","Y", "ParticleLabel", "Location")

#Adds columns with order of particles numbers that can be found on the marker
screenshot and experimental vial locations (1 to 72 from top left to bottom
right).


####Assign experimental time to all experimentally measured particles per image
by adding a column with experimental time to the particle data obtained with
ImageJ. This facilitates the plotting to temporal dynamics.
```

```
##Experimental time ------------------------------------

start.time <- strptime(start.time, "%Y:%m:%d %H:%M:%S")

#Converts start time to date/ time representation.

date.time <- strptime(acquisition.time$DateTime, "%Y:%m:%d %H:%M:%S")

#Acquires acquisition time per image and converts it to a date/ time
representation.

exp.time <- round(-1*(as.numeric(start.time - date.time, units="hours")),3)

#Converts date/ time to experimental time.

acquisition.time <- cbind(acquisition.time, exp.time)

#Adds experimental time to acquisition time file.

colnames(acquisition.time) <- c("Name", "Date", "ExpTime")

acquisition.time$Name <- gsub(".tif", "", acquisition.time$Name)

#Removes *.tif from file names.

unique.images <- unique(raw.data$Label)

#Checks number of unique images.

ExpTime.vec <- rep(0, nrow(raw.data))

#Creates vector with as many zeros as there are rows in the raw data file (equals
number of particles per image times number of images).

for(i in 1:length(unique.images))

{time.i     <-     acquisition.time$ExpTime[which(acquisition.time$Name     ==
unique.images[i])]

indices.1 <- which(raw.data$Label == unique.images[i])

ExpTime.vec[indices.1] <- time.i}

raw.data  <-  cbind(raw.data,  ExpTime.vec,  rep(NA,  nrow(raw.data)),  rep(NA,
nrow(raw.data)), rep(NA, nrow(raw.data)))

colnames(raw.data)[(ncol(raw.data)-3):ncol(raw.data)]      <-      c("ExpTime",
"Location",
"ExpCondition", "ExpID")

raw.data <- raw.data[order(raw.data$ExpTime),]

#Loops over number of scanner images (i.e., 110 images), gives experimental time
of image in acquisition.time file that corresponds to image i. Gives rows that
correspond to image raw.data file that corresponds to image i (each image
typically has 72 particles). Replaces zeros in vector belonging to these rows
by experimental time belonging to image i.


####Identify particles from a vial at a specific physical location on each image
using the X-, Y-coordinates of vial areas. Relate particles to their location
by assigning a location number and match them to the appropriate experimental
conditions.
```

```
##Identify particles per location and add experimental conditions ------------
--------------------------

for(j in 1:nrow(average.coordinates) ){indices.2 <- which(

sqrt(((raw.data$X-      average.coordinates$X[j])^2)      +      ((raw.data$Y-
average.coordinates$Y[j])^2)) < margin.vial)

if(length(indices.2) == length(unique.images)){print(paste(c("All looks fine
for Location ", j, "."), sep = "", collapse = ""))}else{print(paste(c("Warning:
there is an issue for Location ", j, "."), sep = "", collapse = ""))}
#If there is an issue for Location j, go manually through the images and make
sure the issue is corrected. It may happen that a particle was not detected on
all images, e.g., because it started to float, or more than one particle has
been detected in the same well on one image, e.g., because there was a small
piece of loose biomass. In the latter case, you can manually remove the data
from the erroneous particle that is not a granule from the dataset.

raw.data$Location[indices.2] <- average.coordinates$Location[j]

indices.1         <-         which(experimental.condition$Location         ==
average.coordinates$Location[j])

raw.data$Location[indices.2] <- experimental.condition$Location[indices.1]

raw.data$ExpCondition[indices.2]                                          <-
experimental.condition$ExpCondition[indices.1]

raw.data$ExpID[indices.2] <- experimental.condition$ExpID[indices.1]}

if (length(which(raw.data$Location == 0)) == 0) {print("No 0s left and all
coordinates are assigned a location")} else {"Watch out! There are unidentified
particles left in the data."}

#Loops over number of rows in average.coordinates file (i.e., 72 rows for 72
particles). Returns the particle that falls within the X- , Y-coordinates for a
specific position, i.e., 110 particles for each location because there are 110
images. Note: small and not-centered particles may not be detected. Relates the
location number (i.e., 1 to 72) to the X, Y position so that the particle has
the same label on every image. Couples experimental conditions to locations.


####Transform the detected surface area of particles into equivalent diameters.


##Calculation of equivalent diameter from area ------------------------------
-------

raw.data <- cbind(raw.data, 2*sqrt(raw.data$Area/pi), rep(NA, nrow(raw.data)))

colnames(raw.data)[(ncol(raw.data)-1):ncol(raw.data)]   <-   c("EquivDiam_pix",
"EquivDiam_cm")

#Calculates diameter of particle area assuming that it represents a circle.

raw.data$EquivDiam_cm <- raw.data$EquivDiam_pix/scaling.factor

#Converts pixels to centimeters.
```

```
####Plot the average decrease in particle diameter per experimental condition over time.


##Plot diameter over experimental time per experimental condition ------------------------------

treated.final.data <- ddply(raw.data, c("ExpTime", "ExpID"), summarise,

average.diameter = mean(EquivDiam_cm), sd.diameter = sd(EquivDiam_cm),sem.diameter= sd(EquivDiam_cm)/sqrt(length(EquivDiam_cm)))


treated.final.data$ExpID <- as.character(treated.final.data$ExpID)

average.diameter <- treated.final.data$ average.diameter

sd <- treated.final.data$sd.diameter


p <- ggplot(treated.final.data, mapping = aes(x=ExpTime, y= average.diameter, shape=ExpID, color=ExpID))

p <- p + geom_point()

p <- p + scale_shape_discrete(name = "ExpID", breaks=c("1", "2"), labels=c("sludge1", "sludge2"))

p <- p + scale_color_discrete(name = "ExpID", breaks=c("1", "2"), labels=c("sludge1", "sludge2"))

p <- p + geom_errorbar(aes(ymin= average.diameter-sd, ymax= average.diameter+sd))

p <- p + labs(x = "Experimental time [h]", y = "Biomass diameter [cm]")

p #This is Figure 3.8.
```

c. You can use your own generated files or you can run a demo with the files presented at https://doi.org/10.5281/zenodo.3938457.
d. Run the script by clicking on 'Run'.
e. Verify whether the generated plot (**Figure 3.8**) matches with what you would expect based on the experimental time-lapse images.

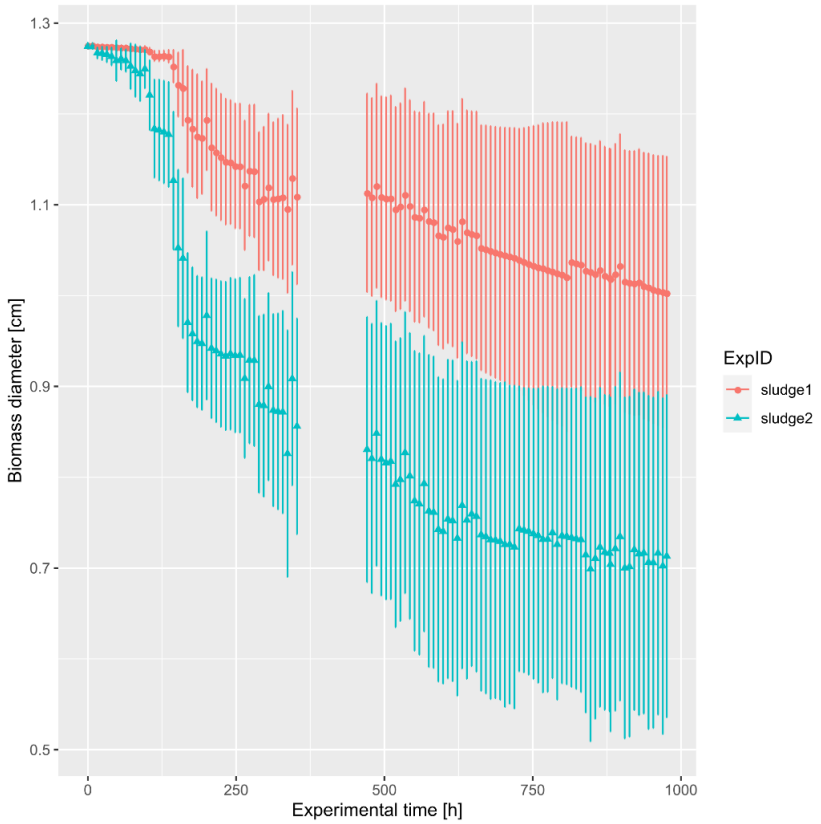

Figure 3.8 Progression of photogranulation. Photogranulation shown as biomass contraction, i.e., decrease in diameter. Hydrostatic batch cultivations were started with two different sludge sources, each containing 36 replicates. Error bars present standard deviations.

Progression of photogranulation as quantified by biomass contraction, *i.e.*, the decrease in diameter over time, is presented in **Figure 3.8** for two different sludge sources. Initially, the sludge bed covers the entire bottom and corresponds to the inner diameter of the vial, *i.e.*, 1.27 cm. During successful photogranulation, a final diameter of about half the initial value or less can be expected. Here the biomass did not granulate well in all 36 replicates per sludge source, and the formation of microbial mats was observed. This large variation in degree of contraction, *i.e.*, the formation of two very different morphotypes, is reflected by the large standard deviations around the average diameters. Despite this heterogeneity, sludge source 2 resulted in more compact OPGs with a smaller average diameter than sludge source 1. Data was not obtained between 354 and 472 hours due to a technical issue.

F. Data exclusion

Failed experiments (*e.g.*, overgrown vial bottoms, floating biomass, tipped vials) can be excluded manually from the analysis by removing the corresponding lines in the raw data or using a file specifying data points to be removed within the script (not described here).

G. Statistical analysis

Standard deviations around the average diameters of replicates are caculated at the end of the R script in Step 01a.

3.8 Notes

The biological phenomenon of photogranulation is not always reproducible: success rates greatly vary and may depend on the inoculum (*i.e.*, the activated sludge) or experimental conditions, *e.g.*, temperature, light intensity or light quality. This variability is subject of ongoing research using this protocol.

I developed a high-throughput time-lapse imaging assay to characterize and standardize measurements of photogranulation progression. When developing this assay, I observed for the first time the development of other spatial structures than photogranules from the same activated sludge source in the same experimental setup. I hypothesized that this is the result of small initial differences in the presence and abundance of cyanobacteria. The next chapter focusses on the link between the final ecosystem spatial structure and final microbial community structure.

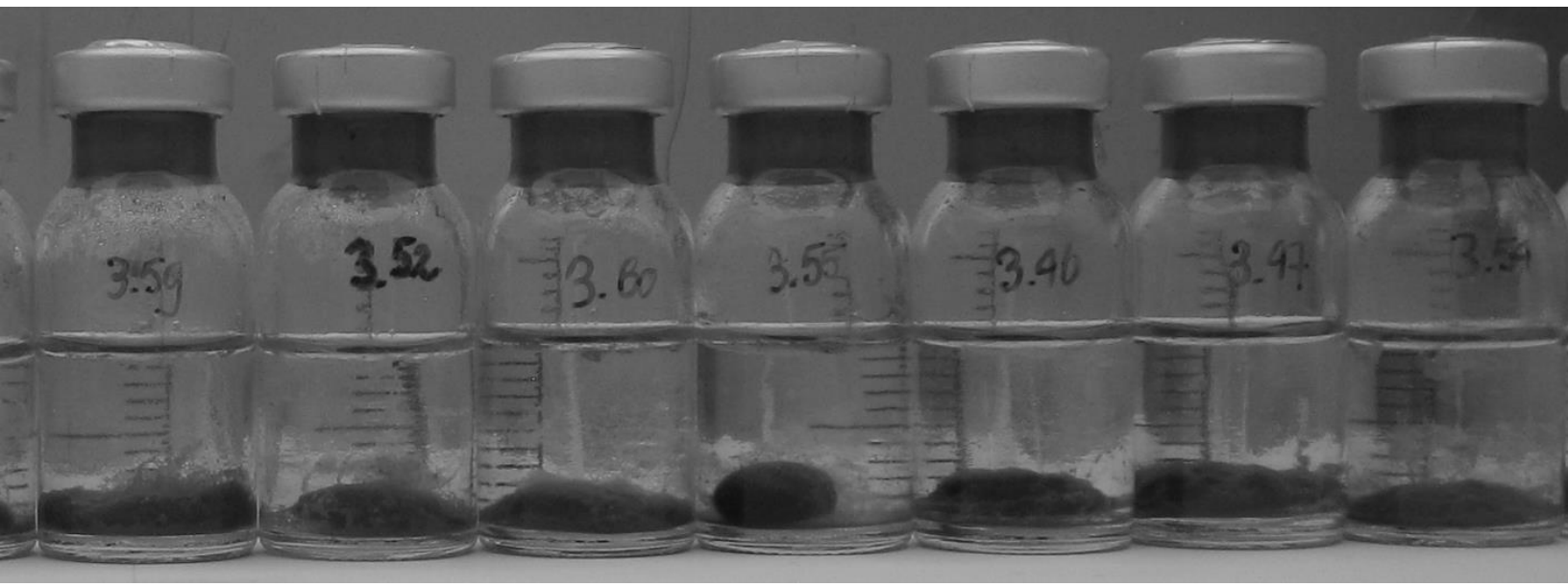
3.59
3.52
3.60
3.55
3.46
3.47
3.54

4

Cyanobacterial climax populations converge independent of ecosystem morphology

4.1 Abstract

Microbial communities are critical to ecosystem function but the relationship between microbial community structure and spatial organization remains poorly understood. When transforming activated sludge into a phototrophic ecosystem in hydrostatic batch cultivations, different morphotypes can be produced, i.e., unconsolidated biomass, microbial mat, hemispheroid, photogranule and a disrupted photogranule. We repeatedly produced distribution of these morphotypes from sludge sources sampled at two different wastewater treatment plants at nineteen time points over a period of 2.5 years. We coupled metabarcoding to qPCR for microbial community analysis. The cyanobacterial, eukaryotic algal and non-phototrophic bacterial populations present in the final morphotypes did not differ from each other. We could therefore not assign a specific role to these final communities in shaping the distinct morphotypes. The ecosystem engineer that determined the development of the final morphotype at an earlier stage may no longer be visible in the final communities. Understanding the role of the microbial community in shaping the ecosystem may contribute to an improved understanding of the development of natural and engineered spatial ecosystems.

4.2 Introduction

Microorganisms often thrive in biofilms attached to a substratum by a self-produced matrix of glue-like extracellular polymeric substances (EPS) (Flemming and Wingender, 2010). The EPS matrix forms a three-dimensional architecture in which cells interact with each other via quorum sensing and metabolic cooperation or competition (Elias and Banin, 2012). Bacterial cells secrete molecules that affect neighboring cells in a distance dependent manner (Alberghini et al., 2009; Yanni et al., 2019). Interaction networks within biofilms are therefore largely dependent on the spatial arrangement of cells (Nadell et al., 2016), i.e., the ecosystem spatial structure. Species properties, species interactions, ecological interactions (e.g., competition for limited resources and syntrophic cross-feeding) and environmental conditions affect biofilm community composition and its spatial structure (Bridier et al., 2017; Gupta et al., 2020; Konopka et al., 2007; Nadell et al., 2010). Despite being an important property of many ecosystems, spatial organization is an often neglected topic in microbial ecology (Widder et al., 2016).

Biofilms in nature can have highly different morphologies. We frequently observe flat, macroscopically mostly two-dimensional structures called microbial mats. However, another morphotype are spherical biofilms, often referred to as granules, that can be found in diverse environments, e.g., cryoconite granules on glacier surfaces (Takeuchi et al., 2001), modern microbialites in marine waters (Brehm et al., 2003) and in tropical lagoons (Abed et al., 2003). Here, we use the term photogranule for a photosynthetic granular morphotype. The outer layer of these photogranules is constituted of a mat-like network of filamentous cyanobacteria that produces EPS and binds mineral particles into a dense sphere (Langford et al., 2010; Reid et al., 2000). In the cited examples, filamentous cyanobacteria are considered ecosystem engineers because of their role in physically structuring the aggregates (Anesio et al., 2017; Edwards et al., 2014; Foster et al., 2009). The EPS-rich outer layer provides structural integrity to photogranules.

The requirements for the formation of photogranules are currently largely unknown, because we typically only observe these structures in nature when they have already formed. It is furthermore experimentally challenging to assess the contribution of environmental variables, such as pH, temperature, or meltwater flow, to microbial community assembly and the development of spatial structure in natural environments. Simplified and controlled microcosms in the laboratory were

developed to overcome this limitation (e.g., Brehm et al., 2003; Havemann and Foster, 2008). Using environmental samples as a starting point, the key features of the natural ecosystems, e.g., highly diverse communities, nutrient recycling and spatial structure, are preserved (Pagaling et al., 2014). These model systems enable us to study the spatial and temporal scales of microbial community assembly and structure development.

In the laboratory, photogranules can be produced in continuously operated laboratory-scale bioreactors (Abouhend et al., 2019) and hydrostatic batch incubations, i.e., from the transformation of activated sludge in closed, light-exposed, hydrostatically incubated vials (Joosten et al., 2020; Milferstedt et al., 2017) (**Chapter 3**). The syntrophic community that developed from the activated sludge community spatially structures itself into a sphere (Milferstedt et al., 2017). The resulting microbial communities had a high abundance of at least one type of gliding filamentous cyanobacteria of Subsection III after the description of Castenholz et al. (2015) in Bergey's Manual of Systematics of Archaea and Bacteria. Also here, the typical 3D photogranule structure and integrity are believed to be formed by filamentous cyanobacteria, reinforced by EPS (Kuo-Dahab et al., 2018). Milferstedt et al. (2017) concluded that photogranulation was a common phenomenon found in this type of ecosystem, catalyzed by Subsection III cyanobacteria.

The hydrostatic batch system is suited for following the temporal and spatial progression of photogranulation (Joosten et al., 2020). When trying to reproduce the results from Milferstedt et al. (2017) using this kind of set-up, we observed that photogranules are not always produced during the transformation of activated sludge. Instead, a wider range of morphotypes may form from the same activated sludge source, in the same standardized experimental setup and exposed to the same experimental conditions (Joosten et al., 2020). Sludge may either remain loose and unconsolidated, firmly compact to form a flat microbial mat, partially contract to form a hemispheroid, or form a fully developed photogranule. Furthermore, the photogranule morphotype can be further differentiated by its response to agitation when it either remains intact or disintegrates.

Even though the experiments started out with macroscopically the same source material exposed to the same environmental conditions, at the microscale, resources, including the initially rare cyanobacteria, may be distributed heterogeneously, creating specific ecological niches (Pagaling et al., 2014). This may lead to the formation of distinct morphotypes. We investigated here the relationship between ecosystem spatial organization and final community structure, under the assumption that the observed morphotypes were built by different microbial communities. Notably, small amounts of initially heterogeneously distributed cyanobacteria may set off the spatial development on different trajectories, eventually leading to distinct ecosystem morphotypes. Over the course of 2.5 years, we repeatedly produced different morphotypes from activated sludge in batch cultivations. Using metabarcoding and quantitative PCR, we analyzed how the microbial populations in climax communities, i.e., at the endpoint of spatial development, differed between the observed ecosystem morphotypes.

4.3 Materials and Methods

4.3.1 *Hydrostatic production of morphotypes*

We repeatedly incubated activated sludge in hydrostatic batch cultivations according to the procedure described in Milferstedt et al. (2017) and Joosten et al. (2020) (**Chapter 3**). Activated sludge was sampled from the aeration basin of the domestic wastewater treatment plants of

Narbonne and Ornaisons, France over a period of 2.5 years (April 2017-September 2019). Typically, a raw sample of 500 µl was stored at -20°C for DNA extraction. Incubations were done in four types of recipients: 24-well microplates, cuvettes, 4 ml and 10 ml vials. For 24-well microplates, cuvettes and 4 ml vials, we used a volume of 1.5 ml of well-mixed activated sludge as inoculum. They recipients were closed with their lid, parafilm, or a rubber stopper, respectively. For the 10 ml vials, 7 ml of activated sludge was used as inoculum and vials were closed with a rubber stopper. We calculated the required volume per recipient by respecting a ratio of height of the sludge bed to inner diameter of the vial of 1.1. This ratio had been used in earlier cultivation sets for 10 ml vials in which a photogranule formed in each incubated vial (Milferstedt et al., 2017). Containers were hydrostatically incubated under constant LED illumination at a photosynthetically active radiation (PAR) between 35 and 130 $\mu mol \cdot m^{2} \cdot s^{-1}$ at room temperature. Vials were illuminated from the top. The amount of light that the biomass received differed per recipient, depending on the LED panel's characteristics and the vials' position underneath it. Experiments lasted five to thirty-two weeks. Twenty-three cultivation sets were incubated from sludge sampled in Narbonne at sixteen time points, and three cultivation sets were done using sludge sampled in Ornaisons a single time point. Each vial yielded one morphotype at the end of cultivation, i.e., unconsolidated biomass, microbial mat, hemispheroid, photogranule or disrupted photogranule. Final spatial structures were checked for their integrity by shaking the vial. An image was taken from all 812 vials to document their final spatial structure and to assign the morphotypes. For each cultivation set, I selected different morphotypes for sequencing, which resulted in 176 samples. The number of samples per morphotype dependent on their abundance in the cultivation set. For 99 samples, mostly photogranules, biomass was used for stereomicroscopy of the exterior and a cross-section using white light and fluorescence stereomicroscopy. For part of the vials, a crycosectioned cross-section was made. For this, biomass was placed in a custom made-holder in which the lower half disappears and the upper half is visible. The upper half was poured over with Tissue-Tek O.C.T. Compound and the sample was incubated at -20°C. After 20 min, the sample was quickly placed under the stereomicroscope and the top half was immediately scraped off with a clean scalpel. The bottom half was directly used for stereomicroscopy. Both halves were collected in a tube and stored at -20°C until DNA extraction. We used a Leica M205FA stereomicroscope (Leica Microsystems SAS, Nanterre, France) equipped with a planapochromatic 0.63X objective, LED reflective illumination and fluorescence illumination using a metal-halide external light source (Leica EL6000) with a blue excitation filter (ET535/50x) and a red longpass filter (E590/LP) for the detection of phycocyanin autofluorescence.

4.3.2 *Microbial community analyses*

4.3.2.1 DNA extraction

DNA was extracted from activated sludge samples (500 µl, 14 samples) and a selection of morphotypes (total biomass per vial, 176 samples) using the DNeasy PowerWater Kit (Qiagen GmbH, Hilden, Germany) following manufacturer's instructions and eluted in 50 µl Solution EB. DNA concentrations and purity were determined by spectrophotometry (Tecan-Spark NanoQuant, M10, Infinite NanoQuant M200, Tecan, Männedorf, Switzerland). Extracted DNA was stored at -20°C.

4.3.2.2 Microbial quantification by qPCR

Bacterial and cyanobacterial (including chloroplasts) qPCR reactions were performed on all DNA extracts. DNA extracts were diluted to a concentration of 10 $ng \cdot \mu l^{-1}$ and sent to GeT-Trix platform

of GenoToul Genopole Toulouse, France (get.genotoul.fr) where further dilutions and qPCR reactions were performed on a Bravo automated liquid handling platform (Agilent, Santa Clara, CA, USA) and a ViiA 7 384-wells real-time PCR system (Applied Biosystems, Waltham, MA, USA).

Bacterial primers targeted the V3-V4 region of the 16S rDNA. Reaction mixtures contained 2.5 µl of SsoAdvanced™ Universal Probes Supermix (Bio-rad Laboratories, Hercules, CA, USA), 100 nM of forward primer BAC338F (5'-ACTCCTACGGGAGGCAG-3'), 250 nM of reverse primer BAC805R (5'-GACTACCAGGGTATCTAATCC-3') and 50 nM of probe BAC516F (5'-Yakima Yellow-TGCCAGCAGCCGCGGTAATAC-TAMRA-3') (Yu et al., 2005) and 1 µl of DNA (final volume of 5 µl). qPCR program consisted of 2 min at 95°C for pre-incubation of the DNA template, followed by 40 cycles at 95°C for 7 s for denaturation and 60°C for 25 s for annealing and amplification.

Cyanobacterial primers targeted regions of the 16S rDNA of cyanobacteria and chloroplasts. Reaction mixtures contained 12.5 µl of SsoAdvanced™ Universal Probes Supermix, 200 nM of forward primer CYAN 108F (5'- ACGGGTGAGTAACRCGTRA-3'), 200 nM of reverse primer CYAN 377R (5'- CCATGGCGGAAAATTCCC-3') (Nübel et al., 1997; Urbach et al., 1992) and 2 µl of DNA (final volume of 12.5 µl). qPCR program consisted of 2 min at 95°C for pre-incubation of the DNA template, followed by 40 cycles at 95°C for 15 s for denaturation and at 52°C for 60 s for annealing and amplification, followed by melting curve analysis.

4.3.2.3 Microbial community sequencing

The 16S rRNA V4-V5 region was PCR amplified using the primer pair 515U 5′-GTGYCAGCMGCCGCGGTA-3′ and 928U 5′-CCCCGYCAATTCMTTTRAGT-3′ (Wang and Qian, 2009) with their respective linkers over 30 cycles (annealing temperature 65°C). These primers target both bacterial (including cyanobacteria and chloroplasts) and archaeal 16S rRNA genes. The same DNA was amplified with the primer pair p23SrV_f1 5′-GGACAGAAAGACCCTATGAA-3′ and p23SrV_r1 5′-CAGCCTGTTATCCCTAGAG-3′ (Sherwood and Presting, 2007) with their respective linkers over 30 cycles (annealing temperature 59°C). These primers target a 23S rDNA plastid marker in cyanobacteria and eukaryotic algae.

DNA amplicons were submitted for sequencing of paired 300 bp reads according to manufacturer's instructions (Illumina MiSeq v3 chemistry, San Diego, CA, USA) to GeT-PlaGe sequencing platform of GenoToul Genopole Toulouse, France. We will submit the sequences to the SRA of NCBI to be publicly available.

Forward and reverse sequences were assembled using a modified version of the MiSeq Standard Operating Procedure (Kozich et al., 2013) in Mothur version 1.42.3 (Schloss et al., 2009). This included pre-clustering at four differences in nucleotides over the length of the amplicon and chimera checking using Uchime (Edgar et al., 2011). Rare unique sequences that appeared less than three times in the entire data set were removed. Taxonomic alignment of 16S and 23S sequences was done to the respective SILVA databases SSURef and LSURef, release 132 (Quast et al., 2013), as provided by Mothur. The alignment was screened to remove poorly aligned sequences (vertical = T, and trump =). 16S sequences were separated into bacterial (including cyanobacteria and plastids) and archaeal sequences, and 23S into cyanobacterial and chloroplast sequences based on their taxonomy. Unclassified bacteria were removed from 23S sequences.

We complemented our data set for comparison with ten samples from Milferstedt et al. (2017), publicly available as the SRA bioproject PRJNA393678. These were microbial communities of

hydrostatically produced photogranules from activated sludge from the same Narbonne wastewater treatment plant: Narbonne, June, 1 and Narbonne, June, 2, 2014. Their cultivations only resulted in the photogranule and mat morphotype.

Sequences with 97% similarity were clustered into operational taxonomic units (OTUs) using the average neighbor clustering algorithm (Nguyen et al., 2016). Clustering of OTUs at 97% did not change our findings compared to unique OTUs but drastically reduced the number of 16S OTUs from 16589 to 5861 and 23S OTUs from 5255 to 785.

4.3.2.4 Statistical analyses

16S relative sequence counts were transformed into qPCR-corrected absolute counts by multiplying the relative sequence counts by the sum of bacterial and phototrophic copy numbers. 23S relative sequences counts were multiplied by only phototrophic copy numbers. Copy numbers were normalized to sludge volume per vial so that we could compare between cultivation sets with different initial sludge volume.

The analyses of sequencing data were done in R version 4.0.3 (R core development team, 2019) using *phyloseq* package version 1.27.6 (McMurdie and Holmes, 2013). 16S amplicons from archaea were not considered because they were low in abundance in the final communities (most abundant in activated sludge). Sequences affiliated with the phylum Cyanobacteria were removed from the 16S sequences for analysis of the 16S bacterial communities. 23S sequences were used to study cyanobacterial and eukaryotic algal communities. We performed a BLAST search using nucleotide collection (nr/nt) database and megablast algorithm on sequences that could not be assigned a taxonomy using our standard operating procedure.

The Bray-Curtis dissimilarity metric was used to quantify the compositional dissimilarity between samples. We tested how community structure was related to a known environmental variable by constrained ordination of the Bray-Curtis distance matrix and fitting of the environmental variables (Anderson and Willis, 2003) using *capscale* in vegan package 2.5.6 (Oksanen et al., 2019). We used *anova* to test the significance of our findings.

Betadisper (vegan package 2.5.6) was performed on the Bray-Curtis distance matrix to test if groups of samples (i.e., morphotypes) were homogenously dispersed in relation to the species distribution in the samples (Masunga et al., 2013). *Betadisper* has to be non-significant, i.e., each group displays similar homogeneity of dispersion, as prerequisite for the valid interpretation of pairwise permutational multivariate analysis of variance (*adonis*). We used *adonis* (vegan package 2.5.6) on the Bray-Curtis distance matrix to test whether groups of samples (i.e., morphotypes) had significantly different community structures (Anderson, 2001).

To reveal which OTUs contribute most to the potential differentiation of communities between morphotypes, we performed Similarity Percentage (*SIMPER*) analysis (vegan 2.5.6) (Clarke, 1993). We subsequently determined with non-parametric Kruskal-Wallis rank sum tests which OTUs are significantly different between morphotypes using the Simper_pretty.R and R_krusk.R scripts by Asteinberger9 (doi: 10.5281/zenodo.4270481), which depend on *vegan* and *dplyr* (version 1.0.2, (Wickham et al., 2019)).

4.4 Results and Discussion

4.4.1 *Hydrostatic production of morphotypes*

The conversion of a heterotrophic matrix into a phototrophic ecosystem goes along with a new spatial organization of the developing ecosystem. The transformation typically takes several weeks and can be monitored in hydrostatically incubated closed vials exposed to light. A range of different spatial structures may emerge from the same inoculum, allowing us to investigate which parameter induces differences in ecosystem spatial organization. A total of twenty-four cultivation sets, each with between 3 and 48 replicated vials, were started from activated sludge sampled at nineteen time points from two wastewater treatment plants. The resulting spatial structures after each experiment were manually classified into five distinct morphotypes: unconsolidated, microbial mat, hemispheroid, photogranule and disrupted photogranule (**Figure 4.1**).

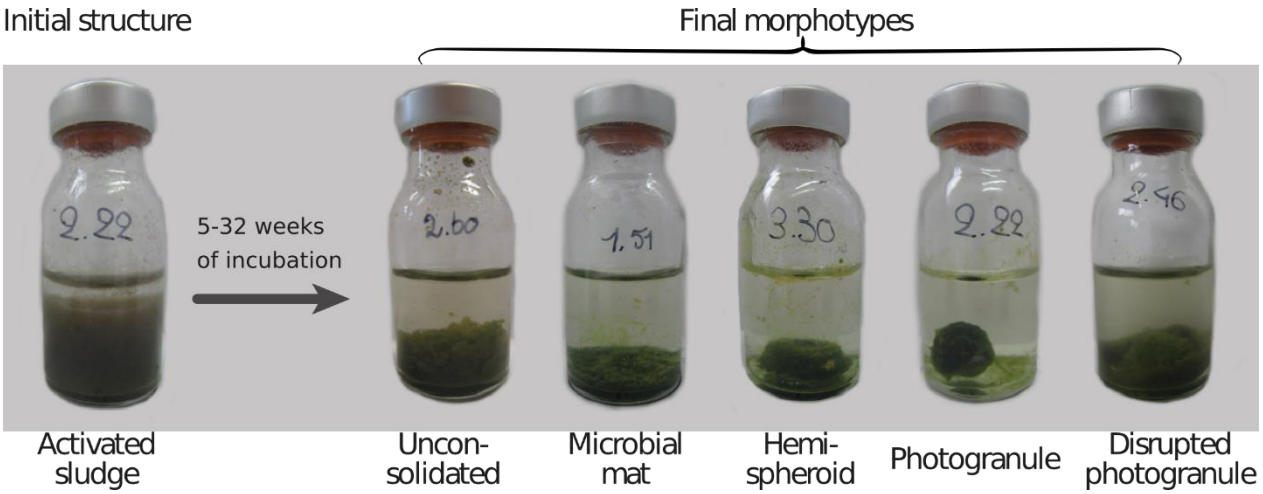

Figure 4.1. Examples of the five distinct final morphotypes resulting from transformation of activated sludge. Activated sludge transferred into a vial was hydrostatically incubated under a source of light and transformed over the course of five to thirty-two weeks into a spatial structure that was assigned one of the five final morphotypes.

In the unconsolidated morphotype the floc structure of the activated sludge is conserved, allowing resuspension when agitated. A flat microbial mat is defined by firm compaction of the activated sludge bed and increased cohesion between particles. Individual flocs cannot be differentiated any more. A mat covers most of the vial bottom. A hemispheroid is defined by a compacted and cohesive sludge bed that is additionally reduced in diameter, i.e., contracted, only covering a fraction of the vial bottom. When the sludge bed contracts even further and increases in height again to form a spherical aggregate, the spatial structure has the photogranule morphotype. A photogranule retains its structure when agitated. When the granule disintegrates upon agitation, the spatial structure is termed disrupted photogranule. We have never observed the transition of one morphotype into another, even when the biomass was incubated over periods longer than the duration of the experiments, i.e., up to one year. This justifies the use of the term of “final morphotypes”. The final samples, mostly photogranules, were examined microscopically. Microbial mats, hemispheroids, photogranules and disrupted photogranules contained a phototrophic layer. Underneath the phototropic layer, non-phototrophic microorganisms dominated. The unconsolidated morphotype also contained phototrophs as seen by the green color of the biomass. The relative abundance of the five morphotypes per cultivation set are shown in **Figure 4.2**. For each cultivation set, we obtained a different distribution of morphotypes. The

microbial mat morphotype was most often observed in most cultivation sets, whereas previously only photogranules were produced in this ecosystem (Milferstedt et al., 2017). Small differences in the initial activated sludge communities may have led to the different distributions of morphotypes per cultivation set.

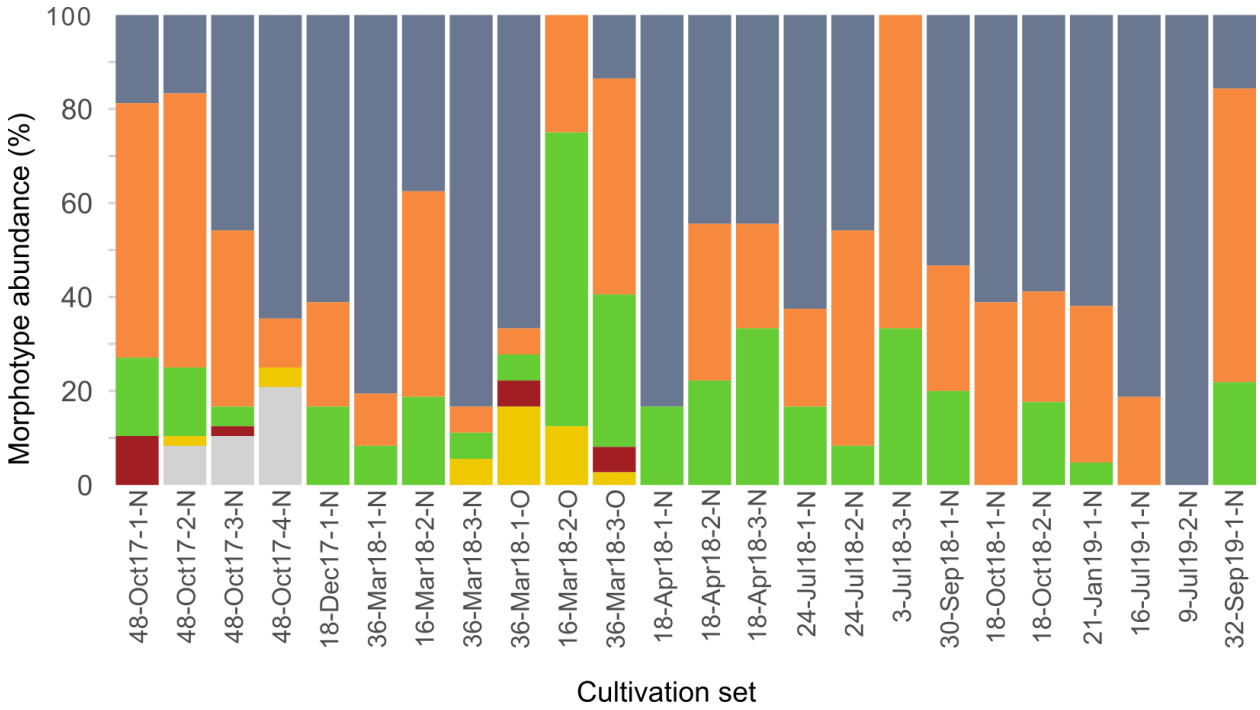

Figure 4.2. Relative abundance of the five final morphotypes per cultivation set. Microbial mats are shown in blue-gray, hemispheroids in orange, photogranules in green, disrupted photogranules in red, unconsolidated biomass in yellow and undetermined samples in light gray. We coded in the names of the cultivation sets the number of repeated vials (e.g., 48), the month and year when the cultivation was started (e.g., Oct 2017), replicated cultivation sets when several were started in the same month and the sludge origin, i.e., Narbonne (N) or Ornaisons (O).

4.4.2 *Microbial abundance*

4.4.2.1 Change in microbial abundance from inoculum to final morphotypes

The morphological conversion of the initially unconsolidated, mostly heterotrophic activated sludge ecosystem into spatially structured syntrophic ecosystem of phototrophs and heterotrophs is confirmed by a change in the microbial communities. The average total size of the microbial communities in the initial activated sludge of $3.8 \cdot 10^{10} \pm 3.0 \cdot 10^{10}$ copies·ml^{-1} was reduced by almost a factor of two in the final samples of $1.7 \cdot 10^{10} \pm 1.7 \cdot 10^{10}$ copies·ml^{-1} (p-value < 0.01, Wilcoxon rank sum test)**Figure 4.3**. This reduction in the closed ecosystem may have resulted from the recycling of activated sludge biomass for the production of structuring agents, such as extracellular polymeric substances that are highly abundant in microbial mats (Wingender et al., 1999), including photogranules (Kuo-Dahab et al., 2018). The number of phototrophic counts increased from $6.2 \cdot 10^{8} \pm 5.8 \cdot 10^{8}$ copies·ml^{-1} in the activated sludge to $4.1 \cdot 10^{9} \pm 3.1 \cdot 10^{9}$ copies·ml^{-1} in the final morphotypes (p-value 0.025, Wilcoxon rank sum test). This was due to an increase in the total cyanobacterial population size from $1.9 \cdot 10^{8} \pm 2.0 \cdot 10^{8}$ to $4.1 \cdot 10^{9} \pm 6.9 \cdot 10^{9}$ copies·ml^{-1} (p-value 0.013, Wilcoxon rank sum test) (**Figure 4.3**a; grouped morphotypes form the final structure).

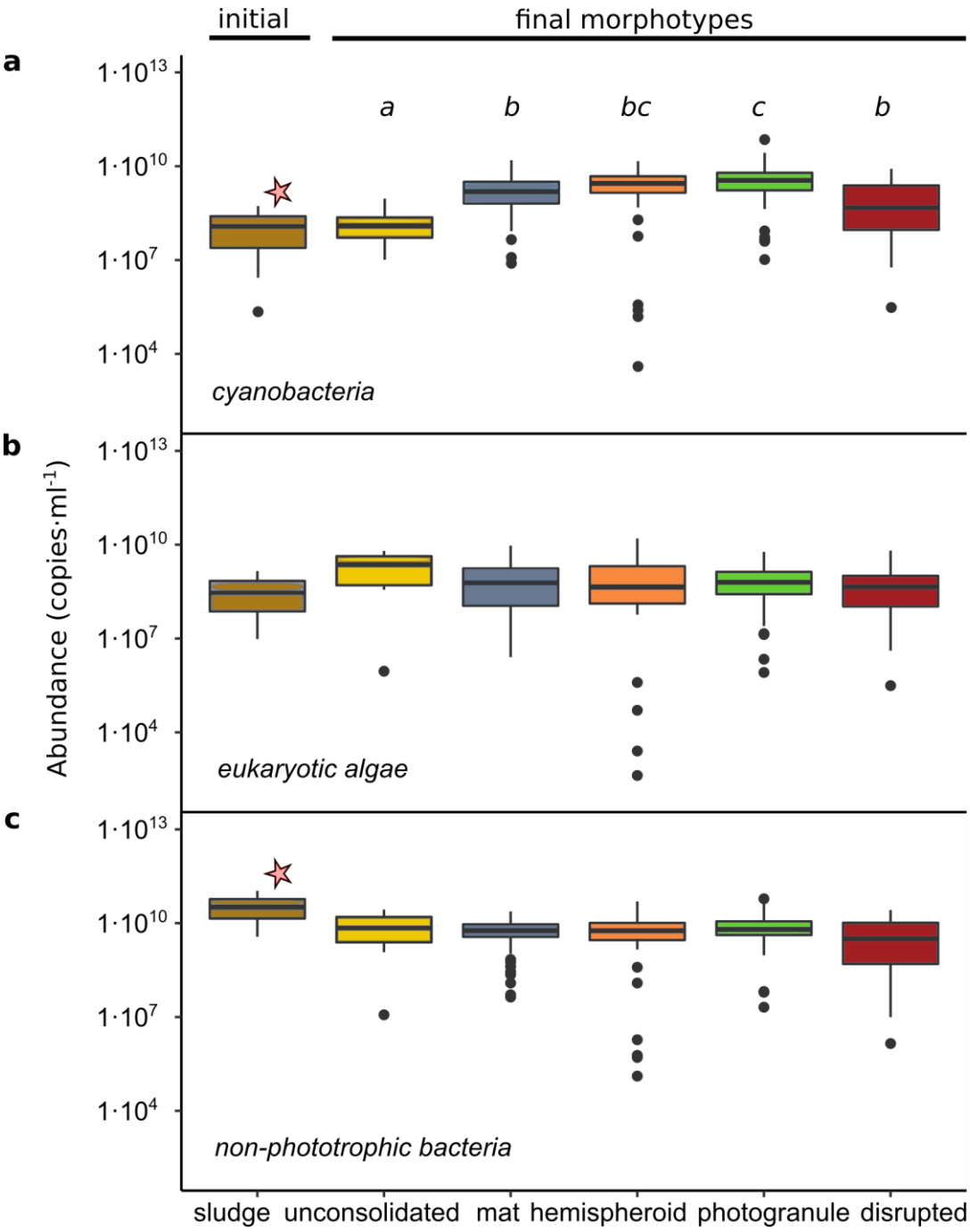

Figure 4.3. Microbial abundance in the initial activated sludge and the five final morphotypes . (a) Cyanobacterial and (b) algal abundance displayed in 23S rRNA gene copies·ml^{-1}. (c) Non-phototrophic bacterial abundance displayed in 16 rRNA gene copies·ml^{-1}. Activated sludge is shown in brown, unconsolidated biomass in yellow, microbial mats in blue-gray, hemispheroids in orange, photogranules in green and disrupted photogranules in red. Significant differences between the initial and final structure (i.e., all morphotypes grouped together) are indicated by an asterisk, and between final morphotypes by letters.

We did not detect a change in the total microalgal population size during morphotype development ($4.3{\cdot}10^{8}{\pm}4.3{\cdot}10^{8}$ copies·ml^{-1} inoculum and $1.4{\cdot}10^{9}{\pm}2.0{\cdot}10^{9}$ copies·ml^{-1} final morphotypes (p-value 0.14, Wilcoxon rank sum test)) (**Figure 4.3**b). The relative abundance of microalgae increased, however, because the total population size decreased. The non-phototrophic part of the communities decreased from $3.8{\cdot}10^{10}{\pm}2.9{\cdot}10^{10}$ copies·ml^{-1} in the activated sludge to $8.6{\cdot}10^{9}{\pm}9.2{\cdot}10^{9}$ copies·ml^{-1} in in the final morphotypes (p-value < 0.01, Wilcoxon rank sum test) (**Figure 4.3**c), most likely because part of the biomass was recycled for the production of phototrophs (Kuo-Dahab et al., 2018).

4.4.2.2 Difference in microbial abundance between the final morphotypes

Total community size did not differ between morphotypes (p-values > 0.05, Wilcoxon rank sum test). Cyanobacterial population size was larger for photogranules ($6.1{\cdot}10^{9}{\pm}1.0{\cdot}10^{10}$) compared to disrupted photogranules ($1.9{\cdot}10^{9}{\pm}2.8{\cdot}10^{9}$), microbial mats ($2.9{\cdot}10^{9}{\pm}3.6{\cdot}10^{9}$) and unconsolidated biomass ($2.4{\cdot}10^{8}{\pm}3.2{\cdot}10^{8}$) (p-values 0.042, 0.023, < 0.01, respectively, Wilcoxon rank sum test) (**Figure 4.3**a). Cyanobacterial population size was smaller for unconsolidated biomass than for the other morphotypes (p-values < 0.05, Wilcoxon rank sum test). We did not detect differences in algal and non-phototrophic bacterial population size between morphotypes (p-values > 0.05, Wilcoxon rank sum test) (**Figure 4.3**b and c, respectively). Eukaryotic algae were more abundant than cyanobacteria in in 13% of the hemispheroids, 14% of the photogranules, 25% of the mats, 33% of the disrupted photogranules and 88% of the unconsolidated biomass. Taking into consideration the cyanobacterial population sizes by morphotype, we observed an increasing abundance of cyanobacteria compared to algae with increasing spatialization (**Error! Reference source not found.**). This corresponds to the results from a study comparing photogranules with disrupted photogranules (Stauch-White et al., 2017).

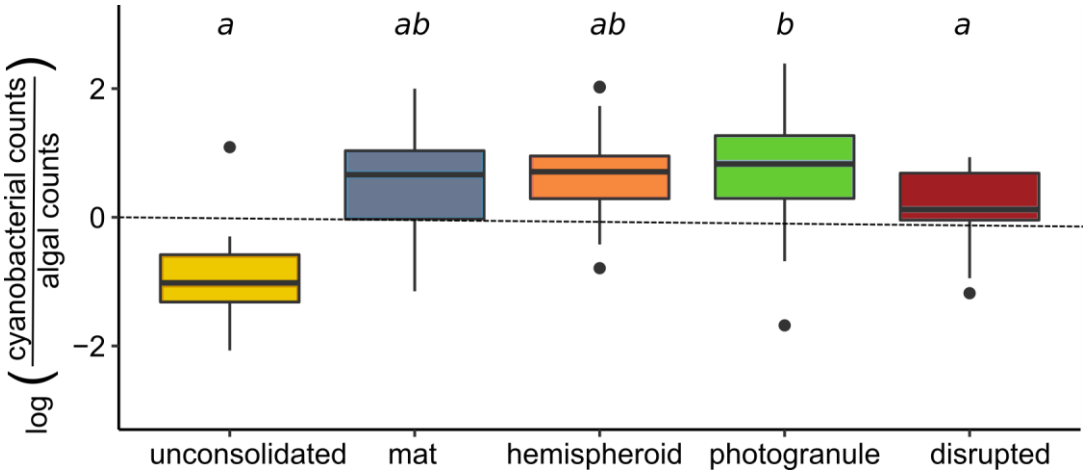

Figure 4.4. Cyanobacteria to algae abundance per morphotype. Unconsolidated biomass is shown yellow, microbial mats in blue-gray, hemispheroids in orange, photogranules in green and disrupted photogranules in red. Significant differences are indicated by letters.

4.4.3 ***Microbial composition***

4.4.3.1 Microbial composition of the inoculum

The initial activated sludge consisted mainly of non-phototrophic bacteria (99±0.6%). Bacterial sequences that were most abundant in the inocula were most closely related to the following microorganisms contained in SILVA SSURef 132 database: C10-SB1A detected in thirteen out of

fourteen samples at an average abundance of 4.0±1.0% and 4.0±1.1%, respectively, of the non-phototrophic population and total community (13/14, 4.0±1.0%, 4.0±1.1%), uncultured *Ardenticatenales* (13/14, 2.5±2.4%, 2.5±1.2%), *Terrimonas* (14/14, 2.1±0.7%, 2.1±0.7%) and an unclassified Gammaproteobacteria bacterium (13/14, 1.8±1.3%, 1.8±1.3%). Highly similar sequence types were found in activated sludge samples from a Danish wastewater treatment plant, following from BLAST searches (99.7% sequence similarity of C10-SB1A to LR636559.1 and MH537630.1, 97.6% of *Ardenticatenales* to LR634333.1 and 100% of *Terrimonas* to LR644797.1) and the literature (Nierychlo et al., 2020, 2019). C10-SB1A and *Ardenticatenales* are members of the phylum Chloroflexi known to cause filamentous bulking in activated sludge systems (Andersen et al., 2020). *Terrimonas* sequence types are also found in a bulking sludge (Jin et al., 2013). The unclassified Gammaproteobacteria bacterium had no close BLAST hits (>98%) to GenBank sequence types.

The initially low abundance of phototrophic microorganisms in the activated sludge (1.5±0.6%) is in line with what is expected for activated sludge (Yang et al., 2011). The inoculum contained on average 0.5±0.7% cyanobacteria. Cyanobacterial sequences that were most abundant in the inocula were most closely related to the following microorganisms contained in SILVA LSURef 132 database: *Planktothrix* detected in six out of fourteen samples at an average abundance of 19±13% and 0.08±0.07%, respectively, of the cyanobacterial population and total community (6/14, 19±13%, 0.08±0.07%), *Plankthothricoides* (5/14, 32±31%, 0.05±0.04%), *Aliterella* (8/14, 20±21%, 0.16±0.41%) and *Chroococcidiopsis* (8/14, 14±13%, 0.07±0.17%). Algae constituted largest part of the phototrophic populations of the inoculum (69±27% algae vs 31±27% cyanobacteria). Activated sludge samples contained on average 0.9±0.4% eukaryotic algae. Algae that were most abundant in the activated sludge were unclassified ((i): 9/14, 13±5.9% of the algal population, 0.14±0.09% of the total population; (ii): 14/14, 6.8±5.3%, 0.05±0.04%; (iii): 11/14, 8.3±4.6%, 0.10±0.08%). Identical sequence types to the unclassified algae sequences were also present in amplicons from Milferstedt et al. (2017). Other than this, sequence (i) had close BLAST hits to the diatom *Planothidium* (99.2% sequence similarity to sequence MW648601.1 in GenBank), sequence (ii) to unicellular alga *Vischeria* (100% to KX839261.1) and sequence (iii) to the diatom *Nanofrustulum* (98.9% to MN276191.1).

4.4.3.2 Microbial composition of the grouped and individual final morphotypes

The low abundance of phototrophs in the inoculum had increased to 38±13% in the final samples. Cyanobacteria constituted largest part of the final morphotypes (72±27% cyanobacteria vs 28±27% algae). Relative cyanobacterial abundance had increased to 29±16% in the final morphotypes. Cyanobacterial sequences that were most abundant in the final morphotypes were most closely related to two sequence types of *Planktothrix* ((i) 116/186, 16±21%, 4.4±8.1%; (ii) 145/186, 9.0±21%, 1.6±4.3%) and two sequence types of *Tychonema* ((i) 130/186, 11±18%, 2.7±5.2%; (ii) 109/186, 17±30%). Gliding filamentous cyanobacteria of Subsection III (e.g., *Planktothrix* and *Tychonema*) were enriched during morphotype development, consistent with what we observed in **Chapter 5**. Filamentous cyanobacteria were more abundant than unicellular cyanobacteria in the final communities, in agreement with the literature on photogranules (Milferstedt et al., 2017; Stauch-White et al., 2017). Gliding filamentous cyanobacteria are often found in structured ecosystems (Anesio et al., 2017; Belnap and Gardner, 1993; Tiron et al., 2015). Not a single cyanobacterial OTU constituted more than 1% of the total community in unconsolidated biomass.

Relative algal abundance had increased to 10±8.7% in the final communities of the morphotypes. Algae that were most abundant in the final morphotypes correspond to *Chlorella* (186/186, 48±26%, 4.6±5.4%). Compared to the other morphotypes, unconsolidated biomass contained in addition at relatively high abundances of *Tetradesmus* ((i) 8/8, 1.4±2.6%; (ii) 7/8, 1.3±2.2%) and unclassified algae ((i) 8/8, 0.5±0.6%; (ii) 5/8, 1.4±1.7%), and disrupted photogranules of a *Durinskia* sequence type (10/12, 0.3±1.5%). Unclassified sequence type (i) had 100% sequence similarity to an amplicon from Milferstedt et al. (2017) and 99.2% to *Scenedesmus* (GU939613.1) and sequence type (ii) had 99.73% sequence similarity both to an amplicon from Milferstedt et al. (2017) and *Parachlorella kessleri* (FJ968741.1). *Scenedesmus* was the most abundant alga in photogranules in an earlier study (Milferstedt et al., 2017). Algal abundance and the number of abundant algal OTUs decreased with increasing spatialization.

The transformation of the heterotrophic activated sludge into a syntrophic ecosystem of phototrophs and heterotrophs, led to a decrease in the relative abundance of non-phototrophic bacteria to 62±13%. Bacteria that were most abundant in the final morphotypes correspond to *Hydrogenophaga* (181/186; 4.9±5.0%, 2.5±2.6%), *Luteimonas* (168/186, 5.7±9.3%, 3.2±5.5%) and *Porphyrobacter* (164/186, 2.5±3.4%, 1.2±1.7%). *Sediminibacterium* was high abundant in half of the final morphotypes (94/186, 3.0±7.1%, 1.6±3.6%). *Sediminibacterium* and *Lysobacter*, which belongs to the same family as *Luteimonas*, were most abundant in photogranules in a previous study (Milferstedt et al., 2017). The same unclassified Gammaproteobacteria bacterium as detected in the activated sludge was furthermore relatively high abundant in mats (47/51, 0.8±0.8%), hemispheroids (47/51, 0.8±0.8%) and photogranules (47/51, 0.8±0.8%), consistent with the results of **Chapter 5**. Compared to the other morphotypes, *Terrimonas* was higher abundant in photogranules (58/69, 0.9±0.9%) and disrupted photogranules (11/12, 1.0±1.0%), possibly related to the formation of the spherical structure. *Salinimonas* was relatively high abundant in mats (42/51, 1.2±1.3%), unconsolidated biomass (7/8, 3.6±4.5%) and disrupted photogranules (12/12, 1.2±1.8%) and unclassified *Rhodobacteraceae* in unconsolidated biomass (8/8, 1.3±1.1%) and disrupted photogranules (12/12, 1.1±1.4%), which may be related to a lack of structure.

4.4.4 *Microbial diversity*

4.4.4.1 Change in microbial diversity from inoculum to final morphotypes

The Shannon index describes diversity considering species richness and evenness of distribution. The cyanobacterial Shannon diversity of the final morphotypes (1.2±0.5) did not differ from that of the initial activated sludge (1.5±0.7) (p-value 0.46, Wilcoxon rank sum test) (**Figure 4.5**a). The final morphotypes had lower algal Shannon diversity of 1.5±0.5 compared to 2.6±0.3 of the inoculum (p-value < 0.01, Wilcoxon rank sum test) (**Figure 4.5**b), mostly caused by a less even distribution of OTUs caused by the strong enrichment of one single OTU, i.e., a *Chlorella* sequence type. The non-phototrophic part of the microbial communities had higher species richness than the phototrophic populations, as indicated by the 7-fold higher number of OTUs. The bacterial Shannon diversity of the final morphotypes of 4.4±0.6 was lower compared to those of the inoculum (5.3±0.4) (p-value < 0.01, Wilcoxon rank sum test) (**Figure 4.5**c), mostly caused by a loss of species richness. The number of observed OTUs from 1038±210 in the initial activated sludge to 490±190 in the final morphotypes (p-value < 0.01, Wilcoxon rank sum test).

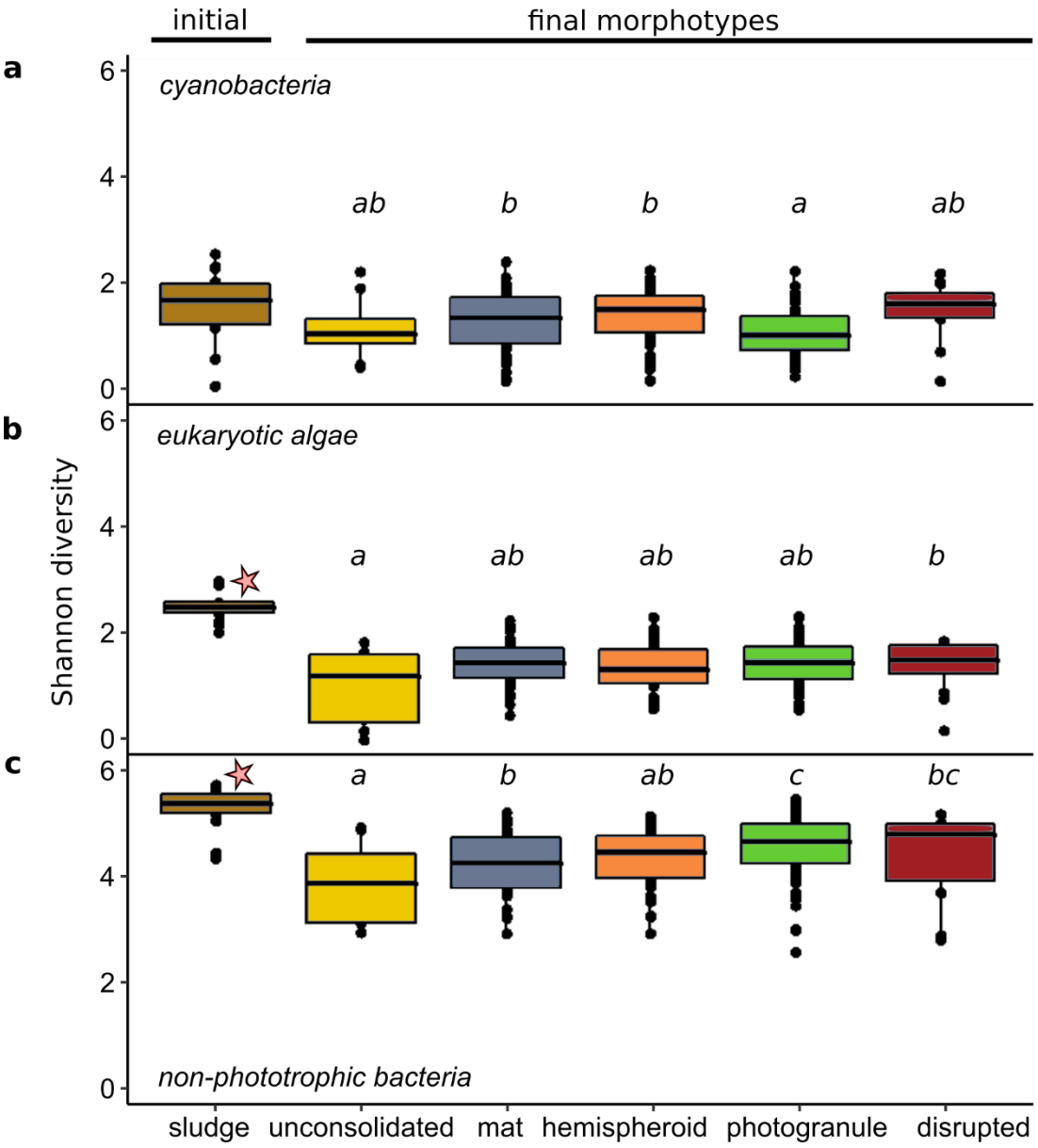

Figure 4.5. Microbial diversity of the initial activated sludge and the five final morphotypes. (a) Cyanobacterial, (b) eukaryotic algal and (c) non-phototrophic bacterial diversity displayed as Shannon index. Activated sludge is shown in brown, unconsolidated biomass in yellow, microbial mats in blue-gray, hemispheroids in orange, photogranules in green, disrupted photogranules in red. Significant differences between the initial and final structure (i.e., all morphotypes grouped together) are indicated by an asterisk, and between final morphotypes by letters.

4.4.4.2 Differences in microbial diversity between the final morphotypes

Photogranules had lower cyanobacterial Shannon diversity (1.0±0.5) compared to hemispheroids (1.3±0.5) and microbial mats (1.2±0.6) (p-values < 0.01 and 0.022, respectively, Wilcoxon rank sum test) (**Figure 4.5**a). Unconsolidated biomass had lower algal Shannon diversity (1.1±0.8) compared to disrupted photogranules (1.5±0.5) (p-value 0.039, Wilcoxon rank sum test) (**Figure 4.5**b) because OTUs were less even distributed. Photogranules had higher bacterial Shannon diversity (4.6±0.6) compared to hemispheroids (4.4±0.8), microbial mats (4.3±0.6) and unconsolidated biomass (3.9±0.8) (p-values < 0.01, < 0.01, 0.016) (**Figure 4.5**c). Unconsolidated biomass had lower bacterial Shannon diversity than microbial mats, photogranules and disrupted photogranules (4.4±0.8) (p-values 0.023, 0.016, 0.039, respectively, Wilcoxon rank sum test). Bacterial Shannon diversity increased with increasing spatialization, mainly because of an increasing number of OTUs from unconsolidated biomass (341±195) to microbial mats (464±180), hemispheroids (468±173) and disrupted photogranules (475±191), to photogranules (544±196). More complex morphotypes may have more niche differentiation, i.e., photogranules have a longer redox gradient along their diameter than flat mats for different species to exist (Wong et al., 2015).

4.4.5 ***Variation in final population structure between samples***

We investigated the link between microbial population structure, final morphotype and the five observed experimental factors “cultivation set”, “origin of inoculum”, “sampling season”, “inoculum volume”, and “duration of cultivation”. This was done using distance-based constrained redundancy analysis. The five factors were chosen based on their potential influence on the final population structures and morphotypes.

The five considered experimental factors and the final morphotypes could explain 35% of the variation in cyanobacterial populations between all 186 morphotype samples, 40% of the eukaryotic algal populations and 38% of the non-phototrophic bacterial populations (**Table 1**). The factor “cultivation set” contributes most to this variation, i.e., 27% for cyanobacteria, 37% for eukaryotic algae and 32% for non-phototrophic bacteria. “Cultivation set” considers each experiment as if it did not share any factors with the others, even though at some time points, experiments were started from the same sludges but in for example different vials types. All “cultivations sets” are listed in **Error! Reference source not found.**. This factor lumping various known and unknown factors was created to test the hypothesis that every cultivation set may be unique, caused by yet unknown factors that may override the communalities between the cultivation sets. The importance that this factor has compared to the more explicit factors indicates that we are still missing a clear understanding of what factors determine the differences in final microbial populations.

Morphotypes could only explain 5%, 4% and 3% of the variation in, respectively, cyanobacterial, algal and non-phototrophic populations between final samples. This was confirmed by *adonis* followed by *SIMPER* coupled to Kruskal-Wallis rank sum test. The variability within cultivation sets is higher than between cultivation sets. Grouping of samples with cultivation sets can also been seen in the PCoA plots in **Figure S1**. However, also within a cultivation set we did not detect significant differences in cyanobacterial, algal and non-phototrophic populations between morphotypes based on *adonis* followed by *SIMPER* coupled to Kruskal-Wallis rank sum test. Contrary to what we hypothesized, we did not find significant differences in final cyanobacterial populations between the five final morphotypes, neither in algal nor in non-phototrophic

populations. It thus appears that morphotypes do not possess their own fingerprint population, preventing us to predict a morphotype from sequence amplicons.

Even the most differentiating factor “cultivation set” among the tested factors does not, in absolute terms, correlate very well with the microbial populations of cyanobacteria, eukaryotic algae and non-phototrophic bacteria. Most of the variation between samples cannot be explained by the final morphotype and identified experimental factors. We hypothesize that stochastic events at inoculation explain the remainder of the variation between samples (Zhou and Ning, 2017).

Table 1. Microbial variation explained by experimental factors and observed morphotypes. Significant values for the individual and grouped factors as calculated by *capscale*.

Microbial group (# OTUs)	Cultivation set	Origin of inoculum	Sampling season	Inoculum volume	Duration of cultivation	Morphotype	Grouped factors
Cyanobacteria (555)	27%	4%	9%	6%	1%	5%	**35%**
Algae (230)	37%	8%	9%	9%	6%	4%	**40%**
Non-phototrophic bacteria (5491)	32%	8%	7%	4%	3%	3%	**38%**

The visually obvious differences between morphotypes do not correlate with their final phototrophic populations structures. Morphotype development must therefore depend on earlier events in the phototrophic populations during the transformation of the activated sludge. Cyanobacterial growth was needed to form a coherent structure. A succession of cyanobacteria with different traits may have led to the development of the five distinct morphotypes, but we do not see this when studying the final population structures (**Chapter 5**). Cyanobacterial succession is common in the formation of spatial structures in nature, e.g., in desert (Danin et al., 1998) and High Arctic biological soil crusts (Pessi et al., 2019). We had a conservative sampling approach in which we waited until morphotypes had stabilized in all vials before harvesting the entire cultivation set at once. We may therefore not have captured the differences in microbial communities that led to the development of the five distinct morphotypes. Microbial population dynamics are needed to reveal the link between phototrophic population structure and spatialization. A difficulty, however, is the, at this point, lack of predictive power during the experiment. When scarifying a vial during the process of structure formation, we cannot know with certainty the final outcome of structure formation. This currently prevents us from linking microbial community structure to a morphotype. An integrated omics approach coupled to mathematical modelling may link key species to functions in spatial structure development (Narayanasamy et al., 2015; Widder et al., 2016). A detailed study of cyanobacterial physiology related to spatialization may help deciphering the different roles of cyanobacteria in structure formation (Martínez-García et al., 2018). Hydrostatic photogranulation can be used as a model system to study spatialization using one type of gliding filamentous cyanobacteria, for example isolated from a final morphotype, in defined synthetic medium.

Phototrophic communities may have converged across the five morphotypes because of a strong selection pressure, e.g., constant high light intensity. We applied constant illumination ranging from 35 to 130 µmol·m^2·s^{-1} PAR to our ecosystem. In comparison, 12 h light/ 12 h dark cycles with a photon flux density of approximately 5 µmol·m^2·s^{-1} is recommended by the Pasteur Culture Collection of Cyanobacteria for xenic cyanobacterial cultures. Our light conditions might have been so extreme that we eventually always selected for the same phototrophic microorganisms despite the role of other phototrophs in the initial development of the distinct morphotypes. Strong selection pressure leads to reproducible community structure (Pagaling et al., 2014). This led us to hypothesize that photogranulation may be the result of self-shading: microorganisms in the outer layer aggregate to protect the interior cells from photo-inhibition such as described for naturally occurring photogranules (Castenholz, 1968, 1967). The outer layer may be formed by thick, robust cyanobacteria that form an interwoven network reinforced by EPS, protecting the thinner, more fragile cyanobacteria and other microbes inside the granule. The most abundant cyanobacteria *Tychonema* and *Planktothrix* in the final structures have relatively large cell widths of, respectively, 6.5-8 µm (Shiels et al., 2019) and 2.3-9.8 µm (Komárek and Komárkova, 2004). They possibly produce relatively large quantities of EPS and contain photoprotective pigments that prevent from photodamage (Balskus et al., 2011; Kurmayer et al., 2016).

In this study, we focused on differences in microbial populations between spatial structures, because we hypothesized that filamentous cyanobacteria play an important role in structuring the ecosystems. EPS is, however, the main structuring component of biofilms. Differences between morphotypes may not (only) be caused by the type of cyanobacteria, but (also) by the type and amount of EPS that they produce in response to culture conditions and cell status (De Philippis and Vincenzini, 1998).

Non-phototrophic bacterial populations became larger and more diverse with increasing spatialization. Photogranules have a smaller surface to volume ratio and therewith a smaller photoactive layer compared the non-phototrophic population than in another morphotype, e.g., a flat microbial mat. Bacteria in a photogranule are located along longer oxygen, redox and nutrient gradients from the photogranule surface to the photogranule core than bacteria in a flat microbial mat. This may have consequences for niche differentiation and microbial community composition (Wong et al., 2015). Microscale measurements coupled to mathematical modeling may give insight into differences in physicochemical gradients between morphotypes (Ouazaite et al., n.d.).

Heterotrophic bacteria that were dominant in the final morphotypes, i.e., *Hydrogenophaga*, *Luteimonas*, and *Sediminibacterium*, were also the dominant bacteria associated with filamentous cyanobacteria that we isolated from photogranules (data not shown). *Porphyrobacter* was furthermore dominant in the final morphotypes, but not detected in cyanobacterial cultures. The repeated observation of high abundance of these cyanobacterial and suggests that these microbes live in close spatial proximity (Ouazaite et al., 2021) from which they mutually benefit. Cyanobacteria provide a support structure and access to carbon and oxygen for heterotrophic bacteria that can decompose and recycle the organic materials. Heterotrophs provide a carbon source to cyanobacteria and stimulate their growth (Delucca and Mccracken, 1977; Herbst, 1978). Bacterial associations of *Hydrogenophaga*, *Porphyrobacter*, *Sediminibacterium* with cyanobacteria has been observed in nature and culture medium (Hube et al., 2009; Kim et al., 2019), also specifically for *Planktothrix* (Kurobe et al., 2018) and *Tychonema* (Pinto et al., 2018). Individual-based modeling may reveal how syntrophic interactions lead to spatial structure development (Estrela and Brown, 2013; Momeni et al., 2013a).

4.5 Conclusion

Activated sludge and its microbial community developed during the transformation into a syntrophic ecosystem with a distinct morphology. What we observe at the end does not show the changes in microbial population structure over time, but presents an endpoint in the morphological development. The cultivation set marked the final community structure. Cyanobacterial growth was needed to form a coherent structure. A higher relative abundance of cyanobacteria compared to algae resulted in a more complex spatially oriented structure. The final morphotype had a small effect on the final phototrophic population structure. Eventually, phototrophic populations converged across the different morphotypes. Spatialization is thus determined at an earlier point in time and microbial population dynamics are needed to reveal the link between microbial population structure and spatialization. Our ecosystem enables the production of a range of morphotypes from the same inoculum under the same experimental conditions. This system can be used as a model ecosystem to gain insight into spatial structure development in natural and engineered ecosystems, e.g., by closely following all succession steps during morphotype development.

I observed the production of a range of spatial structures in replicated incubations, whereas only photogranules were observed in experiments prior to my PhD. Contrary to what I expected, I did not detect differences in final cyanobacterial populations between final morphotypes, neither in algal nor in non-phototrophic bacterial populations. I hypothesized that cyanobacterial species play a role in shaping the ecosystem initially, but that this is no longer visible in the final communities. I investigated whether the morphotype distribution can be shifted towards photogranules by augmenting the inoculum with cyanobacterial strains from the outer layer of mature photogranules or culture collections. I furthermore characterized the morphotype-forming behavior of the cyanobacterial strains in culture medium. The bioaugmentation study is the topic of the next chapter.

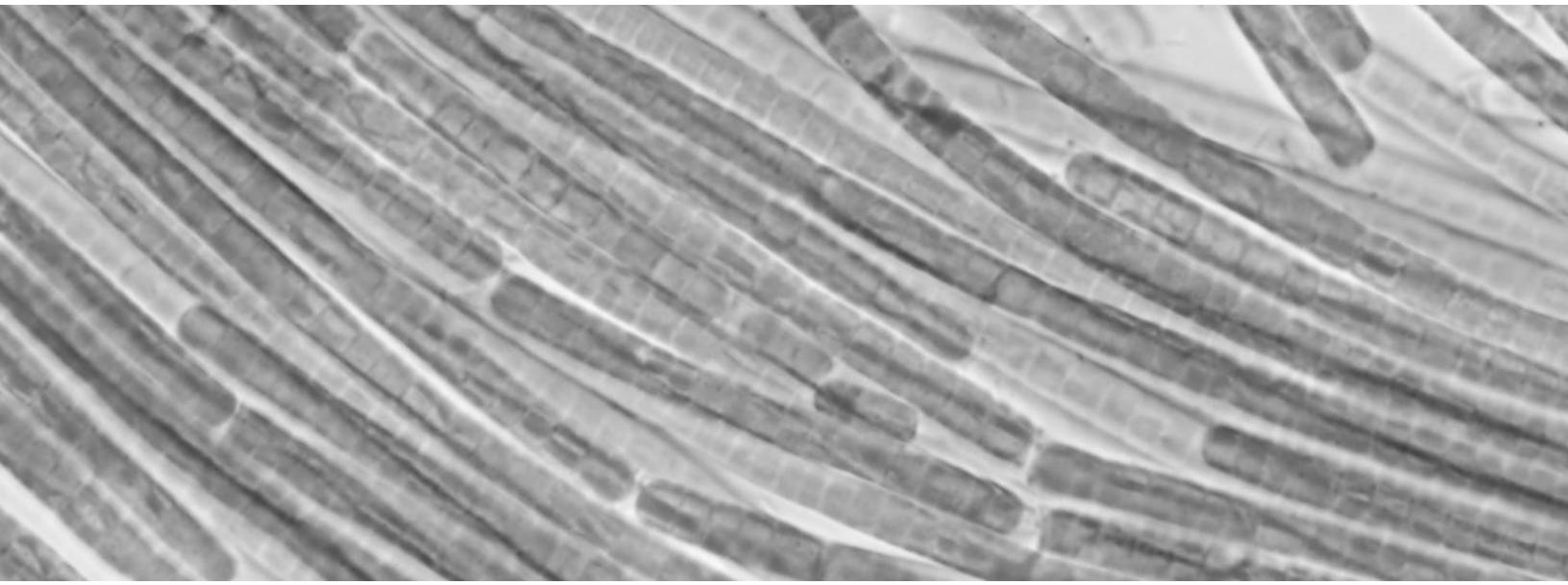

5

Initial type and abundance of cyanobacteria determines morphotype development of phototrophic ecosystems

5.1 Abstract

Photogranules are found in nature, e.g., as cryoconite on glaciers and microbialites in marine waters. To better understand the initial requirements for photogranulation, laboratory models are now available, i.e., using activated sludge as starting matrix. We observed, however, the development of a range of morphotypes in replicated incubations: photogranules, hemispheroids and microbial mats. Here, we investigate how morphotype development can be altered by cyanobacterial augmentation. We hypothesized that gliding filamentous cyanobacteria found in the outer layer of photogranules possess the trait to form photogranules. We augmented five activated sludges with increasing amounts of phototrophic communities or cyanobacterial strains. The initial type of cyanobacterial and its abundance determined the ecosystem's final morphotype. Augmentation in sufficient concentrations steered morphotype development into the direction of the morphotype typically formed by the xenic strain. Final communities were always dominated by mat-forming cyanobacteria, whereas photogranule-formers were low abundant or absent. The presence of photogranule-formers seems to be required for the initiation of photogranulation, but they are eventually lost from the community. Our model ecosystem can contribute to the fundamental understanding of the role of cyanobacteria in spherical structure development, also applying to the formation of cryoconite and microbialites, or engineering of photogranules for biotechnological applications.

5.2 Introduction

Spatial organization is an often neglected topic in microbial ecology despite being an important property of many ecosystems (Widder et al., 2016). It links microbial community structure to ecosystem function by favoring the development of substrate and metabolite gradients in the ecosystem (Momeni et al., 2013b). Investigating the relationship between spatial organization, microbial community assembly and ecosystem function will contribute to the understanding of natural and engineered spatially explicit ecosystems.

Microbial growth as biofilms is a well-known survival strategy (Jefferson, 2004). Cyanobacteria initiate biofilm formation by colonizing the substratum and producing a matrix of extracellular polymeric substances (EPS) that binds and traps other microorganisms (Rossi and De Philippis, 2015). Cyanobacteria are known to produce a variety of spatial structures, including flat mats (Stal, 1995), rafts (Paerl et al., 1989), tufts (Walter et al., 1976) and clumps (Richardson and Castenholz, 1989; Sim et al., 2012). Here, we are interested in the community assembly and spatial development of spherical aggregates known as photogranules (Milferstedt et al., 2017). Photogranules have been found in a wide variety of natural environments, e.g., cryoconite granules on glacier surfaces (Takeuchi et al., 2001), modern marine microbialites in tropical lagoons (Abed et al., 2003) and marine waters (Brehm et al., 2003).

Filamentous cyanobacteria are believed to be keystone species in the development of photogranules (Milferstedt et al., 2017). The majority of cyanobacteria found in photogranules are taxonomically part of Subsection III (Abed et al., 2003; Brehm et al., 2003; Cameron et al., 2012) in Bergey's Manual of Systematics of Archaea and Bacteria (Castenholz et al., 2015). They are characterized by a filamentous morphology and often possess gliding motility. Gliding motility is believed to be essential for photogranule formation (Castenholz, 1967; Shepard and Sumner, 2010; Tamulonis and Kaandorp, 2014; Walsby, 1968). A common feature of photogranules is a phototrophic layer at the biomass-water interface. This layer results from cyanobacterial growth (Shepard and Sumner, 2010) and differentiates photogranules from other spherical structures

formed by aggregation. Aggregation occurs on time scales of minutes to hours in sufficiently dense cyanobacterial cultures (Castenholz, 1967; Walsby, 1968). The mat-like photolayer is rich in EPS (Langford et al., 2010) and contributes to structural stability (Rossi and De Philippis, 2015).

Park & Dolan (2015) described the production of photogranules in the laboratory. These so-called oxygenic photogranules are produced from activated sludge in closed, light-exposed, hydrostatically incubated vials. The transformation of the initially mostly heterotrophic bacterial community into a syntrophic community composed of cyanobacteria and other bacteria takes several weeks. As naturally occurring photogranules, oxygenic photogranules possess an EPS-rich phototrophic outer layer (Abouhend et al., 2019; Kuo-Dahab et al., 2018) densely populated by Subsection III cyanobacteria (Milferstedt et al., 2017; Trebuch et al., 2020). We recently observed that biological replicates did not consistently form a photogranule morphotype. Instead, a range of morphotypes was produced, including microbial mats, hemispheroids and photogranules (Joosten et al., 2020) (**Chapter 3**).

Gliding filamentous cyanobacteria of Subsection III in the outer layer of oxygenic photogranules may possess the necessary traits to photogranulate, but are typically rare in activated sludge. Random differences in their initially low abundance may explain the unreproducible outcome between replicates. We hypothesize that we can shift the morphotype distribution towards photogranules by adding cyanobacteria harvested from outer layers of mature photogranules to the initial activated sludge. This addition is a type of bioaugmentation and has already been successfully applied using cyanobacteria to improve ecosystem function, e.g., in soil (Issa et al., 2007) or wastewater treatment (Silva-Benavides and Torzillo, 2012; Singh and Thakur, 2015).

We performed five independent experiments in which we augmented fresh activated sludge with increasing amounts of phototrophic communities and cyanobacterial strains derived from photogranules or culture collections. We tested how modification of the initial type and abundance of cyanobacterial strains influenced the final community structure and spatial development. Hydrostatic photogranulation can be used as a model ecosystem to test general ecological principles (Konopka, 2006) under controlled conditions in repeated experiments.

5.3 Materials and Methods

5.3.1 *Hydrostatic production of spatial structures from augmented activated sludge*

In five independent experiments, we transformed fresh activated sludge into a phototrophic ecosystem (**Figure 5.1**). Over a period of three years, fresh sludge was sampled at the start of each experiment from the aeration basin of the domestic wastewater treatment plant of Narbonne, France. An aliquot of the activated sludge samples was stored at -20°C until DNA extraction. No activated sludge is available for the first two experiments, but we approximated its composition using a sample collected at another date during the same month to have an indication of phototroph to non-phototroph ratio. We used either 24-well microplates, 4 ml or 10 ml vials for the transformation. Between 1.5 to 10 ml of well-mixed activated sludge was added to the vessel as a function of vessel volume. The volume of augmented phototrophic biomass varied between 10 and 500 µl. Augmentations consisted of serially diluted stock solutions prepared from homogenized photogranules, separated outer layers from photogranules, or of cyanobacterial strains (**Figure 5.1**). Sludge and the additions were gently homogenized. We incubated 9 to 20 replicates per tested condition. Microplates and vials were subsequently closed with their respective lid or a rubber stopper. They were hydrostatically incubated at room temperature under

constant LED illumination at 78 or 104 µmol·m^2·s^{-1} photosynthetically active radiation (PAR) for vials and microplates, respectively. A series of vials was incubated until compact phototrophic morphotypes developed that remained intact when vigorously shaken, approximately after two to eight weeks for the different experiments. Bioaugmentation did not change the speed of contraction of a sludge (p-value > 0.5, t-test) (**Figure S2** and **Figure S3**). We documented the morphotype that formed in each vessel, i.e., a microbial mat, hemispheroid or photogranule (**Figure 5.1**). We consider a microbial mat a flat and compacted structure that covers the entire bottom of the vessel. A hemispheroid is contracted, i.e., it covers a smaller area than the vessel bottom and has a curved surface. A photogranule has a smaller contact area with the vessel bottom than the apparent diameter of the biomass aggregate. Its self-supporting morphology resembles a sitting spheroid. We verified the presence of filamentous cyanobacteria by white light and fluorescence stereomicroscopy using a Leica M205FA equipped with a ET535/50x and ET590 LP filter set (Leica Microsystems SAS, Nanterre, France). Samples were stored at -20°C until DNA extraction.

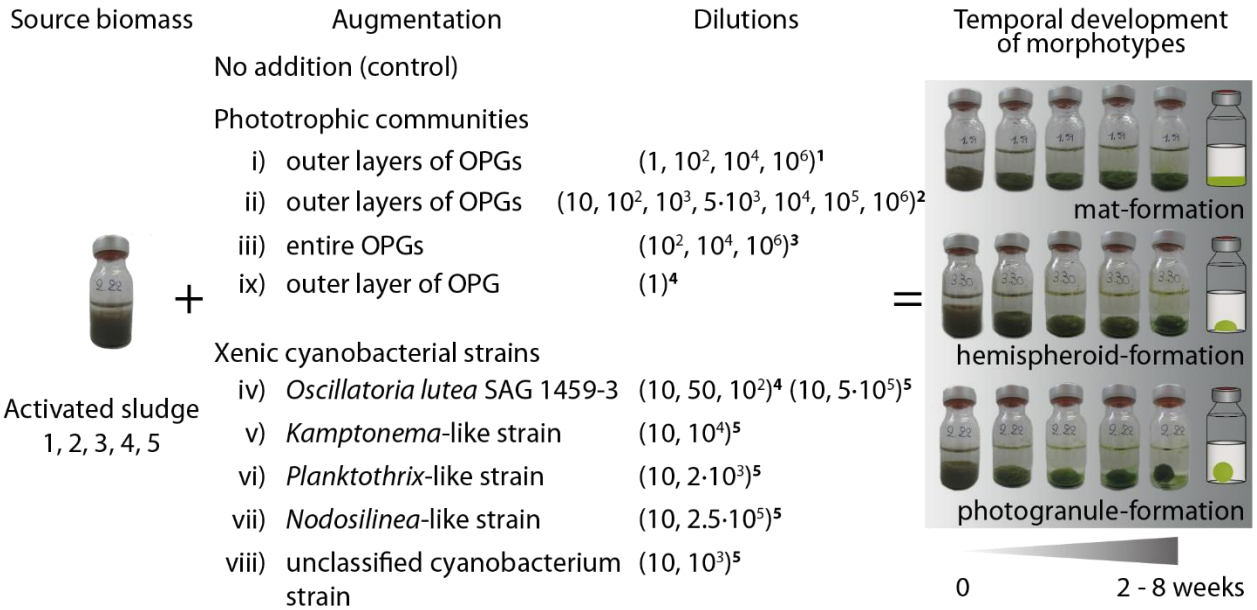

Figure 5.1. Biomass sources for inocula and augmentations and exemplary morphotype development. An overview listing the source biomass, the biomass types used in augmentations, as well as their dilution. Superscripts indicate the source biomass that was augmented with the respective dilutions. The photo shows exemplary temporal developments of the three morphotypes in 10 ml vials with an outer diameter of 24 mm, together with a stylized representation of the final morphotype. The transformation of the untreated or augmented activated sludge could result in a single morphotype, or in a range of morphotypes.

5.3.2 *Production of biomass for augmentations*

Photogranules for augmentations were produced using the procedures of Joosten et al. (2020) (**Chapter 3**) and Milferstedt et al. (2017).

5.3.2.1 Phototrophic communities

Phototrophic communities for augmentations (**Figure 5.1**) originated from phototrophic outer layers peeled off with a tweezer from multiple photogranules (addition **i** and **ii**) or from one single

photogranule (addition **ix**). We also used entire photogranules directly (addition **iii**). Outer layers and entire photogranules were manually homogenized with an Eppendorf micropestle for tubes.

Dominant cyanobacteria in the phototrophic communities were a *Tychonema* sequence type (additions **i**, **ii**, **ix**), and a *Pantanalinema* sequence type (addition **iii**) (see Supplementary information: phototrophic communities for details). The homogenized solutions were the starting point for serial dilutions that were used straightaway to augment the sludge in individual experiments. Cyanobacterial stock solutions and the lowest dilutions were stored at -20°C until DNA extraction.

5.3.2.2 Xenic cyanobacterial strains

The strain *Oscillatoria lutea* SAG 1459-3 (addition **iv**) was ordered from the Culture Collection of Algae (SAG) at the University of Göttingen, Germany. Other xenic cyanobacterial strains used for augmentations were isolated from photogranules by the authors (**Error! Reference source not found.**additions **v**-**viii**) (**Figure 5.1**). For the isolation, single cyanobacterial filaments were separated from different mature photogranules in Z8 medium and transferred to fresh Z8 (Kotai, 1972). Cyanobacterial strains in the augmentations were identified as a *Kamptonema*-like strain (addition **v**), a *Planktothrix*-like strain (addition **vi**), a *Nodosilinea*-like strain (addition **vii**) and an unclassified cyanobacterium strain (addition **viii**) (**Table S2**). All the strains belong to Subsection III (Castenholz et al., 2015): non-heterocystous, unbranched filamentous cyanobacteria of which most exhibit gliding motility. Gliding motility of the strains was confirmed by plating and microscopic observations. Cyanobacterial strains were grown in BG-11 medium (Rippka et al., 1979) at 12/12 light/dark cycles at 30 $\mu mol \cdot m^2 \cdot s^{-1}$ PAR. Cyanobacterial biomasses were homogenized a day before the augmentation experiment. This stock solution was kept in suspension using magnetic stirring and two to three dilutions were made to augment the sludge. The dilutions steps were adjusted to the estimated concentrations of the stock solutions to obtain similar number of cells (**Figure 5.1**). Cyanobacterial dilutions were stored at -20°C until DNA extraction.

5.3.3 ***Determination of microbial community structure***

DNA was extracted from activated sludge, cyanobacterial additions and a selection of final morphotypes using DNeasy PowerWater Kit (Qiagen GmbH, Hilden, Germany) following manufacturer's instructions. DNA concentration and purity were determined by spectrophotometry (Tecan-Spark NanoQuant, M10, Infinite NanoQuant M200, Tecan, Männedorf, Switzerland). Extracted DNA was stored at -20°C.

5.3.3.1 Microbial quantification by qPCR

Concentrations of bacteria and cyanobacteria in all samples were determined by qPCR with universal bacterial primers and primers specifically for cyanobacteria (including chloroplasts). DNA extracts were diluted to a concentration of 10 $ng \cdot \mu l^{-1}$. Universal bacterial primers were used targeting the V3-V5 region of the 16S rRNA gene. Reaction mixtures contained 2.5 µl of SsoAdvanced™ Universal Probes Supermix (Bio-rad Laboratories, Hercules, CA, USA), 100 nM of forward primer BAC338F (5'-ACTCCTACGGGAGGCAG-3'), 250 nM of reverse primer BAC805R (5'-GACTACCAGGGTATCTAAT CC-3'), 50 nM of probe BAC516F (5'-Yakima Yellow-TGCCAGCAGCCGCGGTAATAC–TAMRA-3') (Yu et al., 2005) and 1 µl of DNA for a final volume of 5 µl. The qPCR program consisted of 2 min at 95°C for pre-incubation of the DNA template, followed by 40 cycles at 95°C for 7 s for denaturation and at 60°C for 25 s for annealing and

amplification. Cyanobacterial primers targeted the V2-V3 region of the 16S rRNA gene of cyanobacteria and chloroplasts. Reaction mixtures contained 12.5 µl of SsoAdvanced™ Universal Probes Supermix (Bio-rad Laboratories), 200 nM of forward primer CYAN 108F (5'-ACGGGTGAGTAACRCGTRA-3'), 200 nM of reverse primer CYAN 377R (5'-CCATGGCGGAAAATTCCC-3') (Nübel et al., 1997; Urbach et al., 1992) and 2 µl of DNA for a final volume of 12.5 µl. The qPCR program consisted of 2 min at 95°C for pre-incubation of the DNA template, followed by 40 cycles at 95°C for 15 s for denaturation and at 52°C for 60 s for annealing and amplification, followed by melting curve analysis. Samples were treated using a Bravo automated liquid handling platform (Agilent, Santa Clara, CA, USA) and a ViiA 7 384-wells real-time PCR system (Applied Biosystems, Waltham, MA, USA) at the GeT-Trix platform of GenoToul Genopole Toulouse, France.

5.3.3.2 Microbial community sequencing

Amplicons of 16S (bacteria and archaea) and 23S (cyanobacteria and chloroplasts) rRNA gene fragments were sequenced to determine the microbial community composition. The V4-V5 regions of the 16S rRNA gene was PCR amplified using the primer pair 515U 5′-GTGYCAGCMGCCGCGGTA-3′ and 928U 5′-CCCCGYCAATTCMTTTRAGT-3′ (Wang and Qian, 2009) with their respective linkers over 30 cycles (annealing temperature 65°C). These primers target both bacterial (including cyanobacteria and chloroplasts) and archaeal 16S rRNA genes. The same DNA was amplified with the primer pair p23SrV_f1 5′-GGACAGAAAGACCCTATGAA-3′ and p23SrV_r1 5′-CAGCCTGTTATCCCTAGAG-3′ (Sherwood and Presting, 2007) with their respective linkers over 30 cycles (annealing temperature 59°C). These primers target a 23S rDNA plastid marker in cyanobacteria and eukaryotic algae.

DNA amplicons were submitted for sequencing of paired 300 bp reads according to manufacturer's instructions (Illumina MiSeq v3 chemistry, San Diego, CA, USA) to GeT-PlaGe sequencing platform of GenoToul Genopole Toulouse, France. We will submit the amplicon sequences of the activated sludge, augmentations and final samples to the SRA of NCBI to be publicly available.

Forward and reverse sequences were assembled using a modified version of the MiSeq Standard Operating Procedure (Kozich et al., 2013) in Mothur version 1.42.3 (Schloss et al., 2009). This included pre-clustering at four differences in nucleotides over the length of the amplicon and chimera checking using Uchime (Edgar et al., 2011). Rare unique sequences that appeared less than three times in the entire data set were removed. Taxonomic alignment of 16S and 23S sequences was done to the respective SILVA databases SSURef and LSURef, release 132 (Quast et al., 2013), as provided by Mothur. The alignment was screened to remove poorly aligned sequences (vertical = T, and trump =). Based on their taxonomy, 16S sequences were separated into bacterial and archaeal sequences, and 23S into cyanobacterial and chloroplast sequences. Unclassified bacteria were removed from 23S sequences.

In our work, operational taxonomic units (OTUs) represent unique sequences at the end of the Standard Operating Procedure. Relative sequence counts were transformed to absolute counts using qPCR results by combining copy numbers of bacteria and cyanobacteria for 16S sequence counts and using cyanobacterial copy numbers alone for 23S sequence counts.

Sequence analyses were performed in R 4.0.3 (R core development team, 2019) using phyloseq 1.27.6 (McMurdie and Holmes, 2013). We analyzed initial activated sludge, cyanobacterial additions and final morphotype communities. We analyzed the change in microbial community

structure from untreated or augmented activated sludge to final morphotypes. We tested whether morphotypes had different community compositions using *adonis* (pairwise permutational multivariate analysis of variance) from vegan on the Bray-Curtis distance matrix. Homogeneity of dispersion between groups of samples needs to be assured as it is a prerequisite for a valid comparison of morphptypes using *adonis*. For this, we performed *betadisper* from vegan 2.5.6 (Oksanen et al., 2019) on the Bray-Curtis distance matrix to test if groups of samples (i.e., morphotypes) were homogenously dispersed in relation to their OTUs in the samples (Anderson, 2006).

5.4 Results and Discussion

Photogranulation in hydrostatic batch cultivations can be used as a model ecosystem to study the influence of the initial conditions on community assembly and spatial development of the photogranule ecosystem. Here, we studied the communities of the initial activated sludge and the final morphotypes without and after cyanobacterial augmentation. The biological and chemical composition of the activated sludge differed per experiment due to natural variation. Based on qPCR results, the initial activated sludge in the five experiments was, as expected (Yang et al., 2011), almost entirely composed of non-phototropic bacteria (98.6±0.8%) with 0.3±0.4% cyanobacteria and 1.0±0.5% eukaryotic algae. The initial communities were analyzed at the beginning of three out of five experiments (not available for sludge 1 and 2). The phototrophic community in sludge 3, based on 23S rRNA gene amplicons, was dominated by an uncultured coccoidal *Chroococcidiopsis* (44% of cyanobacterial counts; representing only 0.1% of total bacterial counts). The filamentous cyanobacterium *Planktothricoides* dominated the phototrophic populations of sludge 4 and 5 (respectively, 49% and 79% of cyanobacterial counts; 0.4% and 0.002% of total bacterial counts). These cyanobacteria remained rare after the transformation into phototrophic ecosystems. Cyanobacteria were enriched during morphotype development, making up on average 35±15% of all bacteria and phototrophs in the final microbial communities. Eukaryotic algae constituted 4±4% and the remainder was formed by non-phototrophic bacteria (61±15%). No bacterial OTU was substantially selected during the experiments, with major bacterial OTUs representing less than 5.2±6.4% of the total community (see Supplementary information: “Abundant bacteria in final communities” for more details). A single cyanobacterial OTU could make up to 32±19% of the total community. The substantial increase justifies our focus on cyanobacteria.

The initial activated sludge consisted of small flocs on the order of hundreds of micrometers (Schmid et al., 2003) and is unconsolidated, i.e., entirely resuspendable after agitation. It transformed into well-defined, macroscopic spatial structures over the course of several weeks. We classify them as either microbial mats, hemispheroids or photogranules (**Figure 5.1**). In replicated vessels of five sludges, we observed all morphotypes in varying abundances. Two untreated sludges developed a distribution of all three morphotypes, either being mat-dominated (**Figure 5.2**: control of sludge 3) or with approximately equal weights (**Figure 5.4Error! Reference source not found.**: control of sludge 5). The distributions from three unaugmented sludges were dominated by a single morphotype, i.e., 100% photogranules (**Figure 5.2**: control of sludge 1, 2) or 100% mats (**Figure 5.2**: control of sludge 4).

We were able to modify the spatial self-organization of the developing phototrophic ecosystems by augmenting the initial activated sludge with phototrophic communities or xenic cyanobacterial strains. Outer layers of photogranules used in the augmentations (**Figure 5.1**: additions **i**, **ii**) were

dominated by *Tychonema* sequence types at 47% and 87% of cyanobacterial abundance and 7% and 42% of total bacterial abundance, respectively. Large additions of *Tychonema*-dominated cyanobacterial communities converted the naturally photogranule-forming sludge into a mat morphotype (**Figure 5.2**: additions **i**, **ii**). Entire photogranules (**Figure 5.1**: addition **iii**) were dominated by a *Pantanalinema* sequence type at 100% of cyanobacterial abundance and 48% of total bacterial abundance in the addition. Adding a *Pantanalinema*-dominated community to the dominantly mat-forming sludge likewise increased the proportion of mats in the resulting morphotypes (**Figure 5.2**: addition **iii**). In this experiment, the *Pantanalinema*-like sequence type was already present at 0.03% of the initial activated sludge community, which corresponds to 12% of the cyanobacterial population. This is the only case in our study when the augmented sequence type was already present in the initial activated sludge. Augmenting an initially mat-forming sludge with the xenic *Oscillatoria lutea SAG* 1459-3 strain from a culture collection directed morphotype development towards photogranules (**Figure 5.2**: addition **iv** to sludge 4).

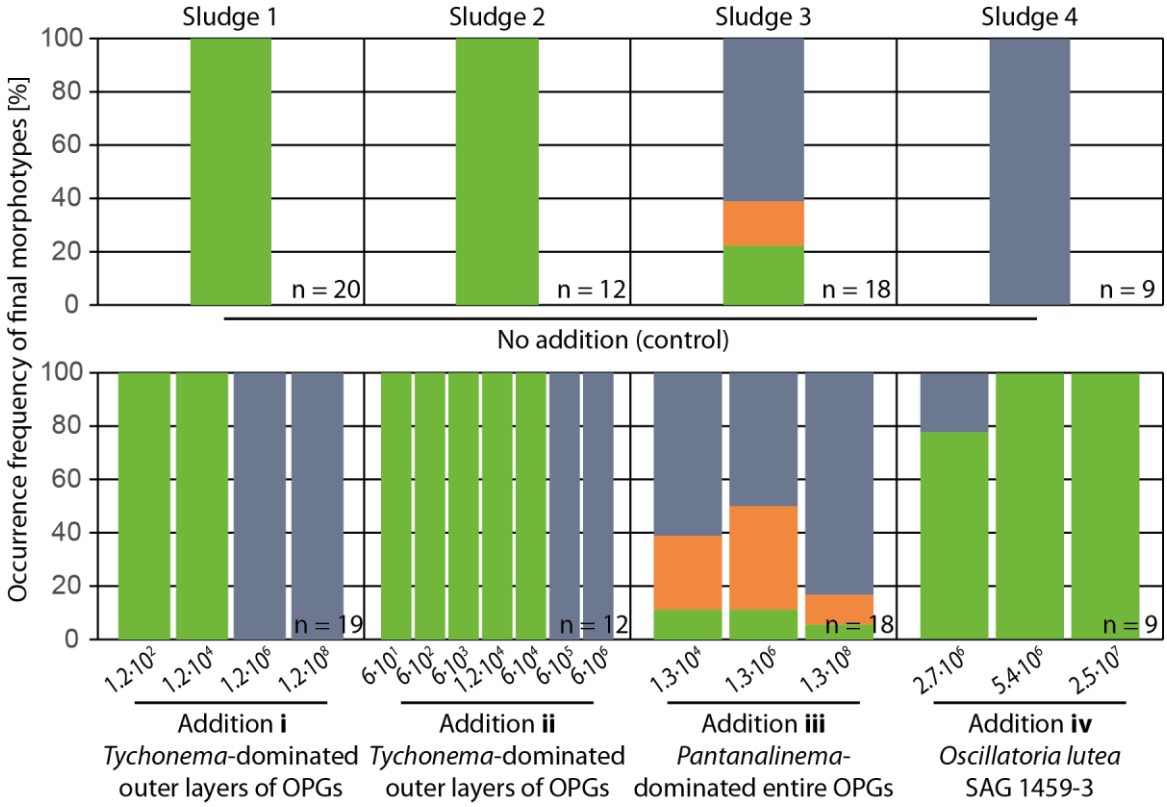

Figure 5.2. Modification of the morphotype-forming behavior of untreated activated sludge after cyanobacterial augmentation. Increasing cyanobacterial augmentations are expressed in 23S rRNA gene copies·mL^{-1} of the most dominant cyanobacterial sequence type per addition, i.e., (**i**-**ii**) *Tychonema*, (**iii**) *Pantanalinema* and (**iv**) *Oscillatoria lutea*. Resulting morphotypes are presented as percentage of the number of replicates in bar plots: photogranules are shown in green, hemispheroids in orange and mats in blue-gray.

We characterized the developing morphotype of our cyanobacterial strains isolated from photogranules when grown in the absence of activated sludge, i.e., in Z8 or BG-11 culture medium (**Figure 5.3**). The *Kamptonema*-like strain, as well as the culture collection strain *Oscillatoria lutea* SAG 1459-3 (**Figure 5.3a, b**, respectively) formed photogranules, as do *Kamptonema animale* SAG 1459-6 and *Kamptonema formosum* PCC 6407 (**Figure 5.3c, d**, respectively). Note that the latter two *Kamptonema* strains were not used for augmentation experiments in this manuscript. In

addition to this phenotypic proximity, *O. lutea SAG* 1459-3 is also phylogenetically close to *Kamptonema* sp. and our *Kamptonema*-like isolate (data not shown). The 23S rRNA amplicon of our *Kamptonema*-like strain shared 98.7% sequence identity with the two *Kamptonema* culture collection strains and 95.9% with *O. lutea* SAG 1459-3.

The *Planktothrix*-like strain built elongated, free-floating aggregates (**Figure 5.3e**). A *Nodosilinea*-like strain formed biofilms covering the water-glass interface with pillars extending from the biofilm into the bulk liquid (**Figure 5.3f**) and an unclassified cyanobacterium strain built patchy biofilms (**Figure 5.3g**). A *Tychonema*-like strain formed a somewhat smooth biofilm covering the entire air-water interface (**Figure 5.3Error! Reference source not found.h**). Its 23S rRNA sequence was identical to the *Tychonema* sequence types found in additions **i**, **ii** and **ix**. The identified mat-forming strains were phylogenetically more distantly related to each other (between 84.1 and 87.5%) than the photogranule-forming strains of *Oscillatoria* and *Kamptonema*.

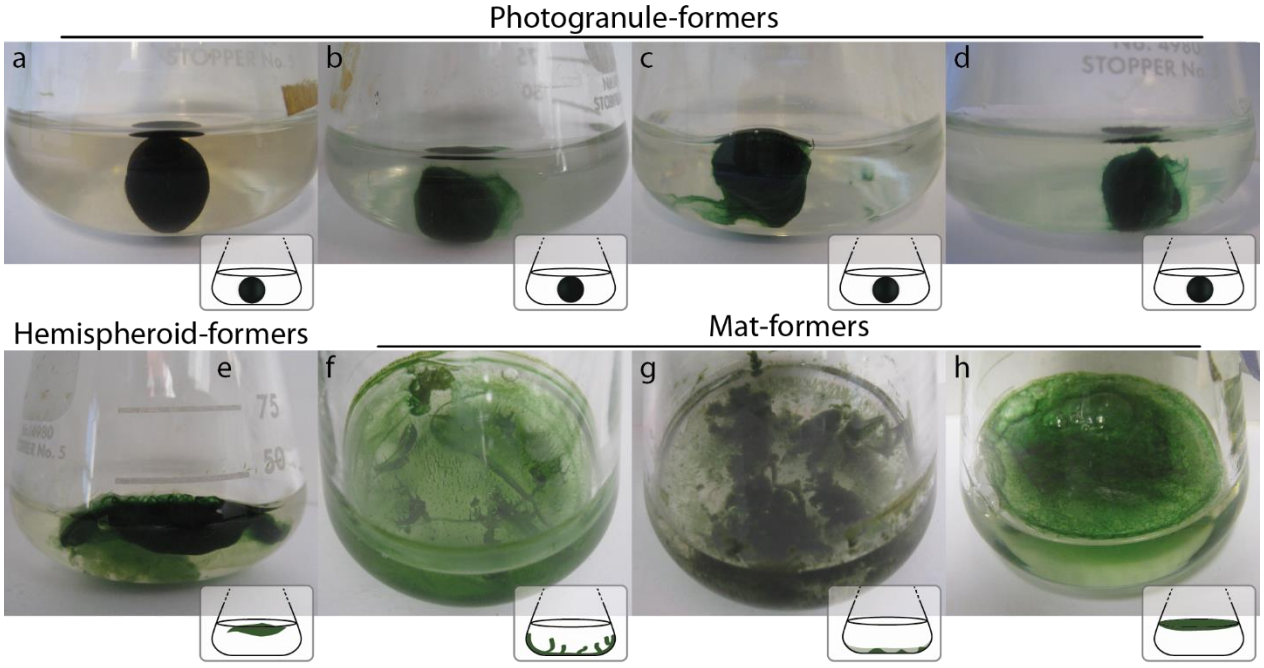

Figure 5.3. Macroscopic structures formed by xenic cyanobacterial cultures. Cyanobacterial cultures in Z8 or BG-11 culture medium in 125 ml Erlenmeyer flasks. Photogranule-formers: (a) *Kamptonema*-like strain, (b) *Oscillatoria lutea* SAG 1459-3, (c) *Kamptonema animale* SAG 1459-6, (d) *Kamptonema formosum* PCC 6407. (e) *Planktothrix-like* strain forming elongated structures or hemispheroids. Mat-formers: (f) *Nodosilinea*-like strain, (g) unclassified cyanobacterium strain, (h) *Tychonema*-like strain.

The morphotype developed by isolated strains is carried over to augmented sludge when the respective morphotype is added in sufficiently large quantities. When adding cyanobacterial strains to an activated sludge that produced an approximately equal distribution of morphotypes (**Figure 5.4Error! Reference source not found.**: control of sludge 5), we were able to push the spatial development towards the morphotype of the augmented strain. The addition of the photogranule-forming strains *Oscillatoria lutea* SAG 1459-3 and *Kamptonema* (**Figure 5.3ab**) directed morphotype development towards photogranules (**Figure 5.4**: additions **iv**, **v**). This corresponds to what we observed for *Oscillatoria lutea* SAG 1459-3 when added to sludge 4 (**Figure 5.2**: addition **iv**). Likewise, the addition of the elongated structure-forming strain *Planktothrix* (**Figure 5.3e**) resulted in a hemispheroid dominance (**Figure 5.4**: addition **vi**). Note that we call the resulting structure “elongated” in the Erlenmeyer flasks, because the floating

biomass is not limited by the glass bottom, whereas we call it a “hemispheroid” when it is in contact with the bottom of a 10 ml vial. The *Planktothrix*-like strain is the only strain we identified that led to the formation of hemispheroids. Augmenting the activated sludge with the mat-forming strains, i.e., *Nodosilinea* and the unclassified cyanobacterium (**Figure 5.3fg**), led to a mat-dominated distribution (**Figure 5.4Error! Reference source not found.**: additions **vii**, **viii**). The shift towards mat formation was equally observed for *Tychonema*-dominated augmentations (**Figure 5.3**, **Figure 5.4**: addition **ix**, dominated by a *Tychonema* sequence type at 47% of cyanobacterial abundance and 29% of total bacterial abundance). This corresponds to what we observed for the *Tychonema*-dominated addition to sludge 1 and 2 (**Figure 5.2**: additions **i**, **ii**).

The properties of the added cyanobacterial strain determine the final spatial structure of the developing ecosystem and can therefore be considered a keystone species in the spatial assembly of these phototrophic ecosystems. Phylogenetically and morphologically similar gliding filamentous cyanobacteria act as ecosystem engineer in nature, e.g., when forming biological soil crust in desert ecosystems (Garcia-Pichel et al., 2013; Mazor et al., 1996) or cryoconite on glacier surfaces (Anesio et al., 2017; Edwards et al., 2014). The choice of cyanobacterium can be used as lever to direct morphotype development when engineering photogranules for biotechnological applications.

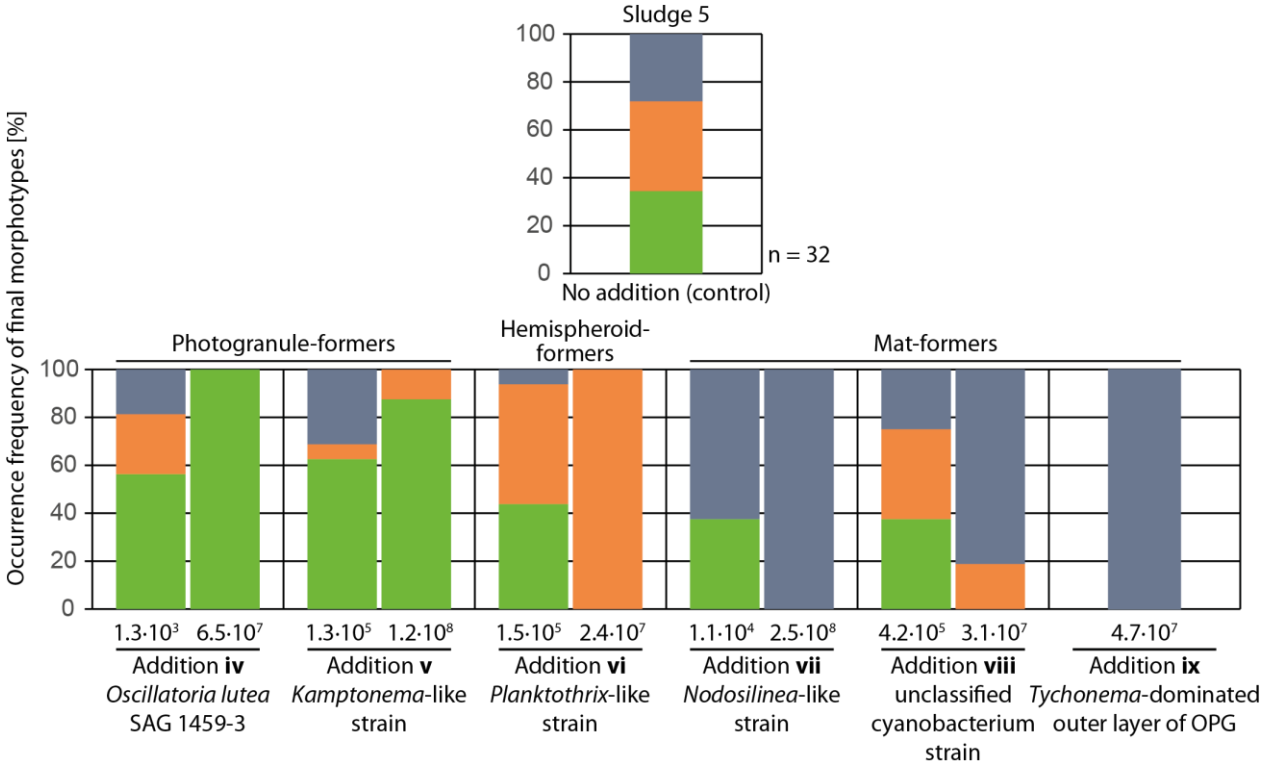

Figure 5.4. Directed modification of the morphotype-forming behavior of an untreated activated sludge after specific cyanobacterial augmentations. Note that addition **iv** contains the same strain as in **Figure 5.2**. Increasing cyanobacterial augmentations are expressed in 23S rRNA gene copies·ml^{-1} of the (most dominant) cyanobacterial sequence type per addition, i.e., (**iv**) *Oscillatoria lutea*, (**v**) *Kamptonema*, (**vi**) *Planktothrix*, (**vii**) *Nodosilinea*, (**viii**) unclassified cyanobacterium and (**ix**) *Tychonema*. Resulting morphotypes are presented as percentage of the number of replicates in bar plots: photogranules are shown in green, hemispheroids in orange and mats in blue-gray. The number of replicates is 16 for all augmentations.

Cyanobacterial augmentations have an ecosystem-wide impact that is concentration-dependent. With increasing numbers of added cells (**Figure 5.2** and **Figure 5.4**), the distribution of morphotypes shifted towards the morphotype that was preferentially produced by the dominant cyanobacterium in the addition. The number of cells needed to induce a shift in morphotypes is not fixed, but may depend on the already present autochthonous cyanobacterial population of the activated sludge. The concentration-dependent shift in spatial structure formation was most clearly visible after the addition of outer layers dominated by the mat-former *Tychonema* to a naturally photogranule-forming sludge (**Figure 5.2**: additions **i**, **ii**;**Figure S2**, **Figure S3**). Photogranules were still produced after small additions of *Tychonema*-containing outer layers, whereas greater additions led to the formation of microbial mats. The shift towards mat formation was also observed after we augmented an activated sludge that produced a wider range of morphotypes with *Tychonema*-dominated communities (**Figure 5.4**: addition **ix**). Increasing additions of the mat-former *Pantanalinema* to a mostly mat-producing sludge increased the proportion of mats among the morphotypes (**Figure 5.2**: addition **iii**). This was also true when other mat-forming cyanobacteria where added (**Figure 5.4**: additions **vii**, **viii**). The same concentration-dependency was observed for the hemispheroid-forming (**Figure 5.4**: addition **vi**) and photogranule-forming strains (**Figure 5.2**, **Figure 5.4**: addition **iv**, **v**).

Observing a reproducible morphotype after augmentation with a specific strain, we hypothesized that morphotype-formation is strain-dependent. We consider the *Tychonema, Pantanalinema, Nodosilinea* sequence types, as well as the unclassified cyanobacterium strain as mat-formers, *Planktothrix* sequence types as hemispheroid-formers, and *Kamptonema* and *Oscillatoria* sequence types as photogranule-formers.

We investigated how cyanobacterial augmentations modified the final microbial community structure (**Figure 5.5**, **Figure S4**). Final morphotypes always had a higher abundance of the identified morphotype-formers than the initial activated sludge. Eventually, in the final spatial structures, mat-formers dominated the communities independent of the added morphotype-former (**Figure 5.5**, **Figure S4bce**). This is visible by the arrows that point towards the top of the triangle in the ternary phase diagrams. Notable exceptions were the *Pantanalinema*-dominated augmentation of $1.3 \cdot 10^4$ copies$\cdot$ml^{-1} (addition **iii**) to sludge 3 for which each of the morphotype-formers dominated at least one of the replicates (**Figure S4a**: blue arrows), and the *Oscillatoria lutea* SAG 1459-3 augmentation (addition **iv**) to sludge 4 (**Figure S4d**), where sometimes also hemispheroid-formers became most abundant. Photogranule-formers always disappeared, despite their influence on morphotype formation (**Figure 5.5c, Figure S4Figure S4de**). Adding photogranule-formers induced a morphological change compared to the control incubations, but were at most detected at low abundances in the final morphotypes. We did not detect significant differences in cyanobacterial community structures between mats, hemispheroids and photogranules within an experiment (p-values > 0.05, *adonis*).

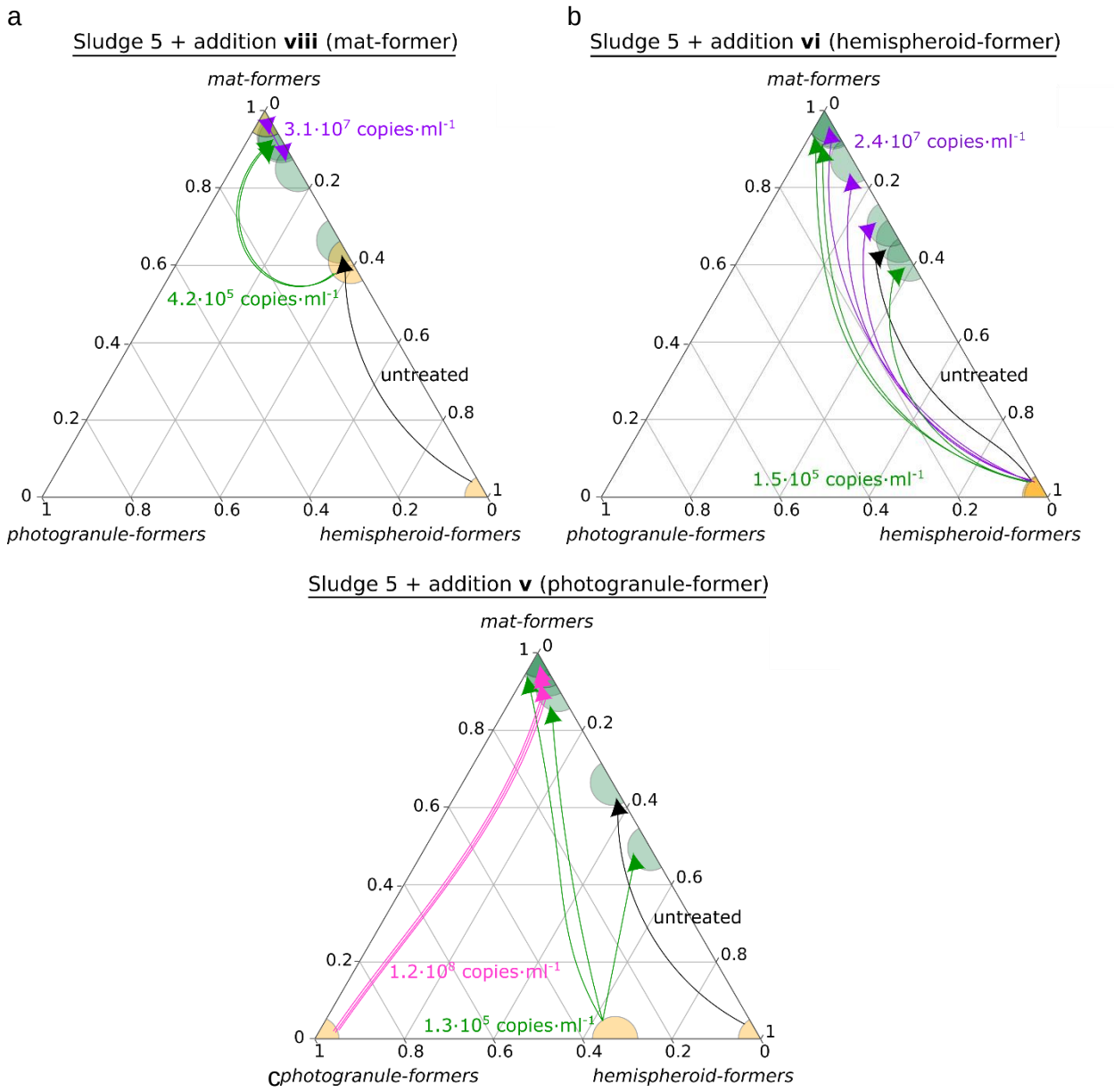

Figure 5.5. Change in proportion of mat-, hemispheroid- and photogranule-formers from the inoculum to the final morphotype communities. (a) sludge 5 augmented with addition **viii**, (b) sludge 5 with addition **vi**, and (c) sludge 5 with addition **v**. Results are based on 23S rRNA gene amplicon sequencing and cyanobacterial qPCR. Initial activated sludge is shown in orange and final morphotypes in green. Untreated control is represented by a black arrow. Increasing cyanobacterial additions are indicated by colored arrows. We used the same color for replicates on a single image (n=2-3 for sludge 5), and for additions with the same order of magnitude between images.

Our results lead us to hypothesize that the final morphotype of an incubation results from the competition between cyanobacteria forming the various morphotypes contained in the addition and those already present in the activated sludge. After small additions of cyanobacteria, whether they were mat-, hemispheroid- or photogranule-formers, the autochthonous activated sludge community was not sufficiently affected and maintained the strongest impact on the final spatial structure. With increasing additions, the augmented cyanobacteria outcompeted the autochthonous cyanobacteria of the activated sludge and may override the otherwise naturally

developing spatial structure of the ecosystem. However, during the development of the final spatial structure, it appears that photogranule-formers are eventually systematically outcompeted, despite their marked effect in earlier succession phases.

We do not know when the added photogranule-formers like *Kamptonema* disappeared during photogranule development. It seems reasonable to assume that *Kamptonema* disappeared after the photogranule structure was built, i.e., after the first detection of the photogranule morphotype. The stable structure of empty sheaths and exopolymers produced by *Kamptonema* could then have been successively colonized by mat-forming cyanobacteria (Kühl et al., 2003). We could possibly detect *Kamptonema* in photogranules when sampling the photogranules directly after they are formed, as opposed to our conservative sampling approach in which we waited for mature structures to be formed and stabilized in all vessels before sampling. Alternatively, *Kamptonema* may have disappeared before we observed the photogranule structure because of the sequential involvement of different cyanobacterial types in structure development. Pioneering cyanobacteria initiate the colonization and stabilization of natural ecosystems, including desert (Danin et al., 1998) and High Arctic biological soil crust (Pessi et al., 2019). They are favored initially when cyanobacterial population density and competition are low. When environmental conditions change, the specialists are outcompeted by generalists that are adapted to a wider range of environmental conditions (Sigler and Zeyer, 2004). Cyanobacterial succession has been observed in eutrophic water bodies as a result of e.g., changing temperature (Chu et al., 2007), irradiance (Oberhaus et al., 2007), CO_2 (Van de Waal et al., 2011) and nutrient levels (Ammar et al., 2014). *Kamptonema* may have been outcompeted by the changing environmental conditions and its relatively slow growth compared to the successive strains (**Table S3**).

Photogranule-formers were possibly needed initially to induce a change in the activities of mat-formers, e.g., in gliding motility, filament flexibility, rigidity or binding ability, to be able to produce the photogranule structure. They may therefore not necessarily play a direct role in structure building, but rather promote other community members (Mohlin et al., 2012). This could have happened when photogranule-formers were still present (Chen et al., 2006) or after they had disappeared, i.e., by means of a microbial legacy effect (Leroy and De Vuyst, 2004). The fact that the putative ecosystem engineer must be initially present but may not dominate or even survive at the end of the process is also observed in other ecosystems, as for example in cheese production (Vass and Langenheder, 2017). There, the ecosystem engineer is needed to ferment and acidify the milk to create a favourable habitat for the community involved in product maturation. The abundance of the starter microbes in the final product is low. Alternatively, *Kamptonema* may have disappeared because of a allelophatic effect of successive strains (Shao et al., 2013).

Whole-genome sequencing and transcriptomics of time-series during the spatialization may help identify what factors drive the relationship between cyanobacterial types and spatialization. Photogranule-formers may for example express genes that are not present or expressed in mat-formers, e.g., those involved in gliding motility (Lamparter et al., 2021), filament flexibility-rigidity (Springstein et al., 2020) and binding ability (Pereira et al., 2015).

It would be ideal to be able to monitor cyanobacterial competition during photogranulation. This, however, is experimentally difficult to do as currently only destructive sampling allows microbial community analysis. Knowing that the development of a range of morphotypes is possible, it would thus be required to predict with certainty the final morphotype of the sacrificed incubation, which has so far not been possible. Now being able to control the outcome by cyanobacterial

augmentation with the appropriate strains, we are able to design future experiments in which we can for example vary the number of added *Kamptonema* and *Tychonema* cells to investigate cyanobacterial competition at the tipping point between photogranule and mat formation. A detailed study of the physiology related to spatialization coupled to individual based modelling may help deciphering the different roles of these cyanobacteria in spatial structure formation (Estrela and Brown, 2013; Kreft et al., 2007).

Linking the formation of spatial structures to the presence and activity of specific cyanobacteria as done here has some limitations. Additions of cyanobacteria-dominated communities derived from the outer layers of photogranules may already contain a variety of cyanobacterial strains. In these more complex additions, potential antagonistic behaviour between strains or other interactions make the interpretation of these experiments more difficult. On the other hand, the use of monoclonal cultures may introduce a culturing bias (Tabacchioni et al., 2000; Ward et al., 1990). This could result in cyanobacterial strains possessing traits that are well-adapted to growth in culture medium, but possibly not anymore to the formation of photogranules. More importantly, when isolation attempts are done using final structures as source material, as we did, it is more likely to recover mat-forming cyanobacteria, as they outcompete photogranule-formers over the incubation period (**Figure 5.5**). Future isolation attempts should therefore take into consideration the putative succession of cyanobacteria in photogranulating samples, as the final community may only contain in low numbers the organisms responsible for structure development.

Our currently identified photogranule-formers have high sequence similarity. They are phylogenetically close compared to the more divers mat-formers. This may be the result of a sampling bias, because we isolated cyanobacteria from mature photogranules that typically contained a low number of photogranule-formers. We may find that photogranule-formers are phylogenetically more diverse when we isolate cyanobacteria at a moment that is better suited for photogranule-formers. If not, phylogenetically close photogranule-formers imply that there is a narrow group of cyanobacteria that can form a photogranules. Being able to produce photogranules may not be as common among Subsection III cyanobacteria as initially suggested (Milferstedt et al., 2017).

5.5 Conclusion

Our initial hypothesis that all cyanobacteria present in the outer layer of mature photogranules form this particular spherical structure oversimplified the process of photogranulation of biological material containing a diverse cyanobacterial community. Sufficiently large additions of phototrophic communities or xenic cyanobacterial strains to activated sludge led to a change in the distribution of morphotypes towards the morphotype typically formed by the augmented strain. It seems that independent of the initial community composition and additions, including situations where photogranule-formers were added, mat-forming cyanobacteria eventually outcompete other morphotype-formers. However, despite their eventual displacement from the phototrophic population, photogranule-formers like *Kamptonema* were the ecosystem engineers and shaped the final ecosystem structure as their addition led to a change in the distribution of morphotypes towards photogranules. Our model ecosystem can contribute to the fundamental understanding of the initial requirements for cryoconite and microbialite development and the engineering of photogranules in biotechnology.

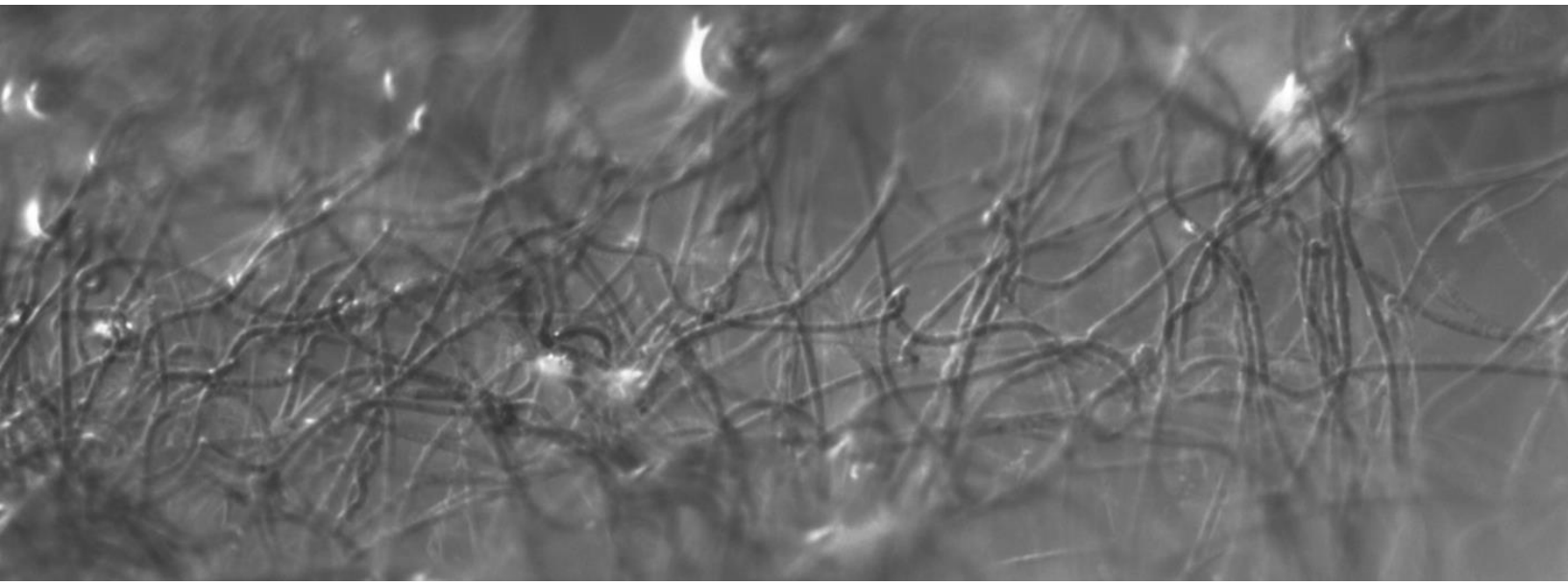

6

Encountered issues and recommendations for improvement

In this chapter, I will outline issues that I encountered during my PhD project and give recommendations for improvement for future researchers on hydrostatic photogranulation or a related topic.

We developed a high-throughput time-lapse imaging assay to quantify photogranulation to compare between cultivation sets and conditions. The assay provides us a way to measure biomass contraction in many vials simultaneously without having to move the vials. A limitation of the assay is that it captures only two dimensions whereas photogranulation is a 3D phenomenon. A 3D assay could visualize the exact transition from loose activated sludge to a spherical aggregate that we cannot document with the scanner, specifically the moment when the spherical structure first appears. We briefly tested the use of X-ray tomography with Eric Rondet and Thierry Ruiz of the University of Montpellier. Results from this tests were not easily interpretable because of the high water and low mineral particle content in photogranules produced in hydrostatic batch cultivation. A 3D assay may be worth looking into in the future.

Before I started my PhD, activated sludge transformed into a photogranule in practically each incubated vial. Only a few photogranules were formed in the large number of incubated vials after the start of my PhD, which resulted in a low photogranulation success rate. There is no good record of the initial conditions when photogranulation success rate was close to a 100%. I recommend to well characterize the current activated sludge that forms a range of morphotypes, e.g., its floc size, microbial community structure, organic matter and nutrient composition, to have this data available for when the sludge recovers its high photogranulation success rate. Then we can compare the results and identify the initial parameters that result in photogranulation.

Halfway through my PhD, I shifted my research efforts from modifying the activated sludge matrix for photogranulation to photogranulation from cyanobacterial strains. With the help of Charlotte Duval and Sahima Hamlaoui of the group of Cécile Bernard at the Muséum national d'Histoire naturelle (Paris, France), I isolated twenty-one gliding filamentous cyanobacteria from mature photogranules. Even though the strains are monocolonal with respect to cyanobacteria, they contain a number of associated bacteria. I was ultimately interested in learning whether photogranulation follows from a cyanobacterial trait, without the involvement of its associated bacteria, or whether it results from the combined activities of cyanobacteria and heterotrophic bacteria. Because it is time-consuming (months to years) and difficult to form an axenic culture from a cyanobacterial strain, I ordered axenic cyanobacteria from the Pasteur Culture Collection of Cyanobacteria (Paris, France). I observed the formation of photogranules by *Kamptonema formosum* PCC 6407, but it appeared that my culture got contaminated over time. I recommend redoing this exercise to unravel the role of bacteria in the formation of the spherical structure. Alternatively, bacterial communities surrounding a cyanobacterial strain can be exchanged (engineered) to investigated how bacterial species affect the photogranulation ability.

We selected our 16S cyanobacterial qPCR assay based on a study that investigated the mechanisms of photogranulation (Stauch-White et al., 2017). This assay did, however, not produce repetitive results for the standard curves in our laboratory. The assay works sufficiently to have an indication of the copy numbers, but it is highly recommended to optimize the 16S cyanobacterial qPCR assay to obtain a higher accuracy if this line of research was to be continued.

We selected our 16S V4-V5 sequencing primer pair based on the premise that they did not amplify plastids (Hodkinson and Lutzoni, 2009; Wang and Qian, 2009). In addition, we selected a 23S plastid primer pair to amplify plastids. We did, however, find a lot of plastid sequence types in our

16S samples. A RDP's ProbeMatch search (http://rdp.cme.msu.edu/probematch/search.jsp) showed that this primer pair binds to plastids, as good as they do to bacteria. Depending on the objectives of future microbial community studies, more specific primer pairs will have to be selected.

For sequencing, we used 16S sequencing primers that target archaea, bacteria and plastids and 23S sequencing primers that target plastids. For qPCR, we used 16S bacterial primers that target bacteria, excluding cyanobacteria, and 16S cyanobacterial primers that target plastids. Because sequencing primers targeted overlapping microbial groups and qPCR primers did not target the same microbial groups as the sequencing primers, we had to carefully check to which sequences the copy numbers applied. A smarter choice of sequencing and qPCR primers that target sequences of the same microbial groups will make this easier in the future.

We used partial 16S and 23S rRNA gene amplicon sequencing to profile microbial communities of photogranules and other spatial structures. When I isolated cyanobacteria from photogranules, I used the same high-throughput sequencing method to get an idea of their identity. Partial amplicon sequences are, however, not sufficiently large to provide taxonomic resolution at a species and strain level (Johnson et al., 2019). Full-length 16S and 23S rRNA gene sequences by a long-read sequencing technology are better suited for this (Callahan et al., 2019).

I learnt that the SILVA LSU database (release 132) does not provide a well-curated taxonomic description of the cyanobacterial sequences. This became clear when I made phylogenetic trees with reference sequences extracted from the SILVA database. I found sequences with the same taxonomic names in different clusters in the phylogenetic tree. Erroneous classifications often occur through misidentifications or modifications in nomenclature (Komárek, 2018). I therefore suggest using a reference database of which the taxa names have been verified and updated for further studies, e.g., the curated database of cyanobacterial strains called "CyanoType" (Ramos et al., 2017).

Cyanobacterial nomenclature is under constant revision as scientists are figuring out a common approach to cyanobacterial taxonomy, which makes it difficult to compare results between studies (Abed et al., 2003). I already noticed that taxa names changed when I updated the SILVA LSU database from version 115 to 132, giving me seemingly different cyanobacterial community compositions of photogranules. I observed that this mistake was also easily made by other researchers comparing their results to the literature. Being aware of this, I tried to stay away from cyanobacterial classification for a long time, and rather looked at overall similarities or differences between samples. This was, however, no longer possible when we encountered the different activities of cyanobacterial types in **Chapter 5**.

For cyanobacterial classification, it is recommended to complement molecular methods with e.g., morphological, ultrastructural, biochemical or ecologies other studies, which is called a polyphasic approach (Komárek, 2016; Wilmotte et al., 2017). I started the morphological characterization of the cyanobacterial strains right after their isolation, mostly because I wanted to relate their properties to photogranulation. I learnt however, that, as an untrained person, it is difficult to properly provide a morphological description of a cyanobacterial strain. In addition, I observed changes in morphological features over the period of one year. I do not know whether these changes resulted from the adaptation of the strains to cultivation conditions in general, or specially to applied conditions, such as type of culture medium or light intensity (Albrecht et al., 2017). The morphological features are, however, needed if we want to classify our isolates. An important

consideration is furthermore the impact of continued transfer of the cyanobacterial strains on their traits, and if we can still properly identify the strains now they have been in culture medium for almost two years.

I started to assess the EPS composition and abundance of cyanobacterial strains together with the MSc student Raffaello Mattiussi, in collaboration with Elisabeth Girbal-Neuhauser and Claire Emmanuelle Marcato-Romain of Laboratoire de Biotechnologies Agroalimentaire et Environnementale (LBAE of Université de Toulouse, France). We selected our EPS extraction method based on the work of Loustau et al. (2018). These authors tested two different physical (sonication, cation exchange resin) and three different chemical (formamide, EDTA, Tween 20) methods to select a robust procedure for the extraction of EPS from aggregates of three benthic microorganisms, including the filamentous cyanobacterium *Phormidium autumnale*. They found that dispersing of the aggregates, followed by formamide addition and incubation with Dowex cation exchange resin, resulted in the highest EPS (mostly proteins) yield with low cell lysis. We optimized their extraction approach for our cyanobacterial strains. We extracted EPS from our strains and started their characterization, but were not able to finish this due to technical issues and time limitations. We did not manage to obtain reproducible results for the calibration curve of the anthrone-sulfuric acid assay for polysaccharide quantification, possibly because the sulfuric acid was not sufficiently concentrated and because of the high lab room temperatures mid-summer, which may have directly induced the reaction. The anthrone-sulfuric acid assay for polysaccharide quantification has to be adapted to be reproducible in our lab. I believe that understanding the role of EPS composition and abundance in spatialization is an interesting and important topic and should be pursued.

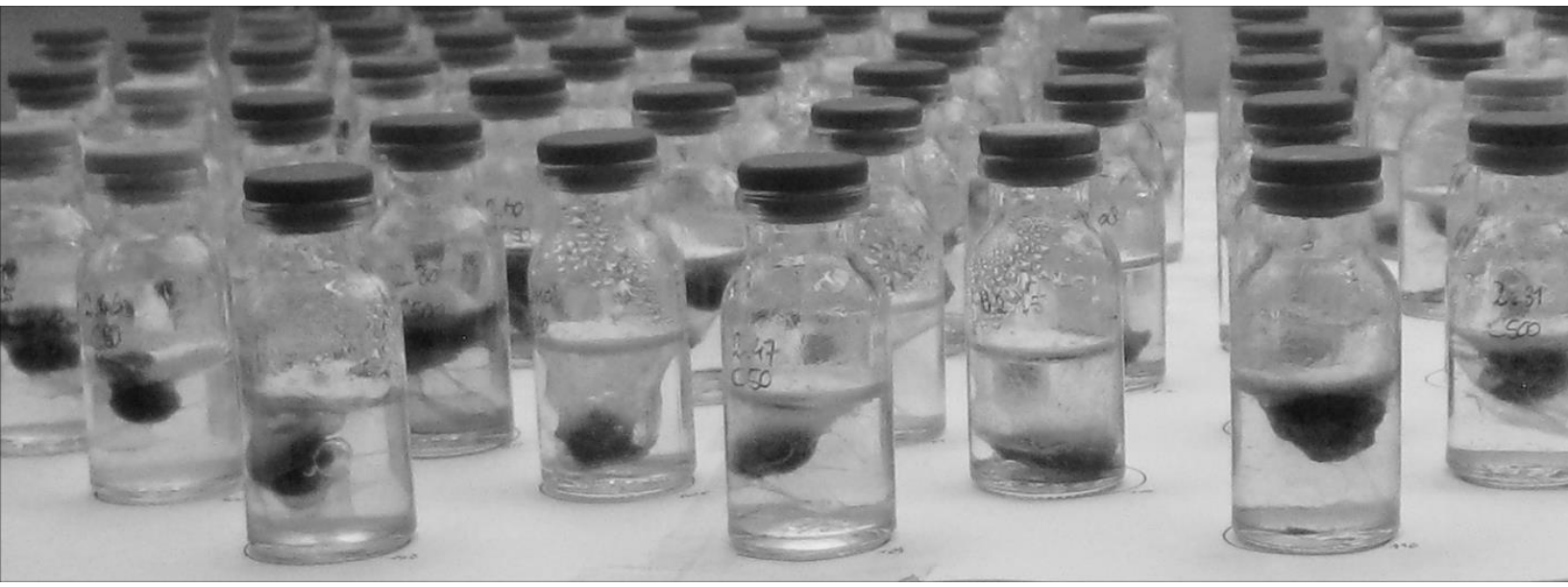

7

Conclusion

The objective of my PhD research was to explore the minimum conditions for the formation of oxygenic photogranules from a microbial ecological angle. A perspective well beyond my PhD work would be to apply this knowledge to control photogranulation in biotechnology. This chapter gives an overview of my findings and how they contribute to our understanding of microbial community assembly and structure formation during photogranulation.

During my PhD, photogranules were not always produced from the transformation of activated sludge, contrary to what was observed in preliminary experiments before I started my PhD. I worked with activated sludge inocula that typically formed a small number of photogranules compared to total number of morphotypes. There is no good record of the initial conditions when photogranulation success rate was still close to a 100%, which makes it difficult to find out what has changed in the initial conditions that now results in the formation of a range of spatial structures. Based on the cyanobacterial augmentations presented in **Chapter 5**, the change may lie in the initial presence and abundance of mat-, hemispheroid- and photogranule-forming cyanobacteria that are enriched and compete with each other, determining which spatial structure is formed.

My plan at the start of my thesis was to modify parameters in the complex activated sludge inoculum and measure how this affects the dynamics and final photogranule diameter to identify the minimum requirements for photogranulation. I therefore developed and published a high-throughput time-lapse imaging assay, that is presented in **Chapter 3**. The assay allowed us to monitor the dynamics of biomass contraction for many vials in parallel without having to touch them and possibly disturb the ecological environment. This approach appeared, however, less useful than intended due to the unexpectedly low photogranulation success rate. I could not systematically test if a modification of the initial conditions improved photogranulation because the activated sludge source that I used as a control produced varying distributions of spatial structures.

I therefore did an intensive study of producing and sampling a wide range of spatial structures (i.e., unconsolidated biomass, microbial mats, hemispheroids, photogranules and disrupted photogranules) to link final spatial organization to final microbial community structure and identify species that are needed for photogranulation in **Chapter 4**. Contrary to what I expected, the visually obvious differences between morphotypes did not correlate with their final community structures. Spatial structure development must therefore depend on earlier events in the community during the transformation of the activated sludge. A succession of different functional microorganisms, notably cyanobacteria, may have led to the development of the distinct spatial structures. Spatialization increased with increasing cyanobacterial to algal abundance, indicating the need for cyanobacterial growth to form a coherent structure. Phototrophic communities may have converged across the five spatial structures because of the high light intensities that we applied to the ecosystem. This strong selection pressure may ultimately have resulted in the same phototrophic communities despite the roles of different phototrophs in structure development initially. This led us to hypothesize that photogranulation is a result of self-shading: microorganisms in the outer layer aggregate to protect the interior cells from photo-inhibition, such as described for naturally occurring photogranules. The outer layer may be formed by thick, robust cyanobacteria (here, *Tychonema* and *Planktothrix*) that form a dense network that is reinforced by EPS and protects the more fragile microbes in the interior.

Spatialization increased with increasing non-phototrophic bacterial population size and number of OTUs. Photogranules have a smaller surface to volume ratio and therewith a smaller photoactive layer compared the non-phototrophic population than in another morphotype, e.g., a flat laminated

microbial mat. Bacteria in a photogranule are located along longer oxygen, redox and nutrient gradients from the photogranule surface to the photogranule core than bacteria in a microbial mat. This may have consequences for niche differentiation and the microbial community composition. The bacteria that were found to be dominant in the final morphotypes in **Chapter 4** and **5**, were also the dominant bacteria in cultures of gliding filamentous cyanobacteria isolated from photogranules, i.e., *Hydrogenophaga*, *Luteimonas* and *Sediminibacterium*. This suggests that these microorganisms live in close spatial proximity and have a syntrophic relationship.

From the augmentation experiments in **Chapter 5**, I learnt that the spatial self-organization of the ecosystem can be steered in a certain direction. The cyanobacterial strain had a profound effect on the resulting spatial structure when added in sufficient amounts. Cyanobacterial strains promoted either mat, hemispheroid or photogranule formation. Photogranule-forming strains *Oscillatoria* and *Kamptonema* made their mark on the final morphotype, but not on the final community structure because they were outcompeted by mat-formers, i.e., *Tychonema*. The presence of photogranule-formers seems to be required for the initiation of photogranulation, but not for maintenance of the spherical structure. I do not know at what point in time the photogranule-formers disappeared from the developing ecosystem. I hypothesized that they could initially compete or even lead the competition with other morphotype-forming strains. *Kamptonema* may have created a solid matrix of empty sheaths and other polymers that was successively colonized by mat-forming strains. In that case, the loss of *Kamptonema* from the photogranule communities must have happened after the 3D structure was built, possibly because of changing environmental conditions or a high selection pressure. Alternatively, *Kamptonema* disappeared before we first observed the photogranule and its spatial legacy remained to push the community into photogranulation.

Because mat-forming cyanobacteria are highly abundant in photogranule outer layers and photogranule-forming strains are practically absent, I isolated more mat-formers than photogranule-formers (10 to 1). The single photogranule-forming strain showed the same behavior as three culture collection strains in that it formed a spherical structure. The observed photogranule-formers were phylogenetically closer to each other than the mat-formers. This may be a distorted view because, as appeared later, the moment of isolation was not preferred for the selection of photogranule-formers. It may, however, also indicate a narrow range of cyanobacteria that are capable of photogranulation. Repeated observations of the formation of the same macroscopic structure by the same cyanobacterial strain suggests that the ability to photogranulate is inherent to the strain.

A tipping point of my PhD was when I started to work with cyanobacterial strains isolated from photogranules and ordered from culture collections. From cultivating the cyanobacterial strains on defined minimal media, I learnt that they can form photogranules in the absence of a complex activated sludge matrix. Contradictory to photogranules formed from activated sludge, these granules do not contain an unconsolidated interior of non-phototrophic bacteria. From microscopic observations, their interior seems to be made up of empty sheaths and other polymers. Cyanobacteria can thus build the immobilization structure themselves and do not dependent on an allochthonous matrix for the formation of the spherical structure. I do, however, not know whether cyanobacteria do this alone or in collaboration with their associated bacteria. I reduced the requirement for photogranulation from a complex activated sludge matrix to a xenic, gliding filamentous cyanobacterial strain in defined synthetic medium. This could possibly be further reduced to an axenic strain.

With my thesis, I bridged the research fields of microbial ecology and process engineering. Photogranulation in semi-stagnant environments was known in nature, but never applied in biotechnology. I acquired a deeper understanding of the minimum conditions allowing the development of oxygenic photogranules: a photogranule-forming cyanobacterium in defined synthetic medium. This principle may also apply to the development of cryoconite granules and modern microbialites in nature. The acquired knowledge offers a starting point to steer photogranulation by augmentation in bioreactors and to ecological engineer photogranule microbiomes starting from a single photogranule-forming strain for application in biotechnology.

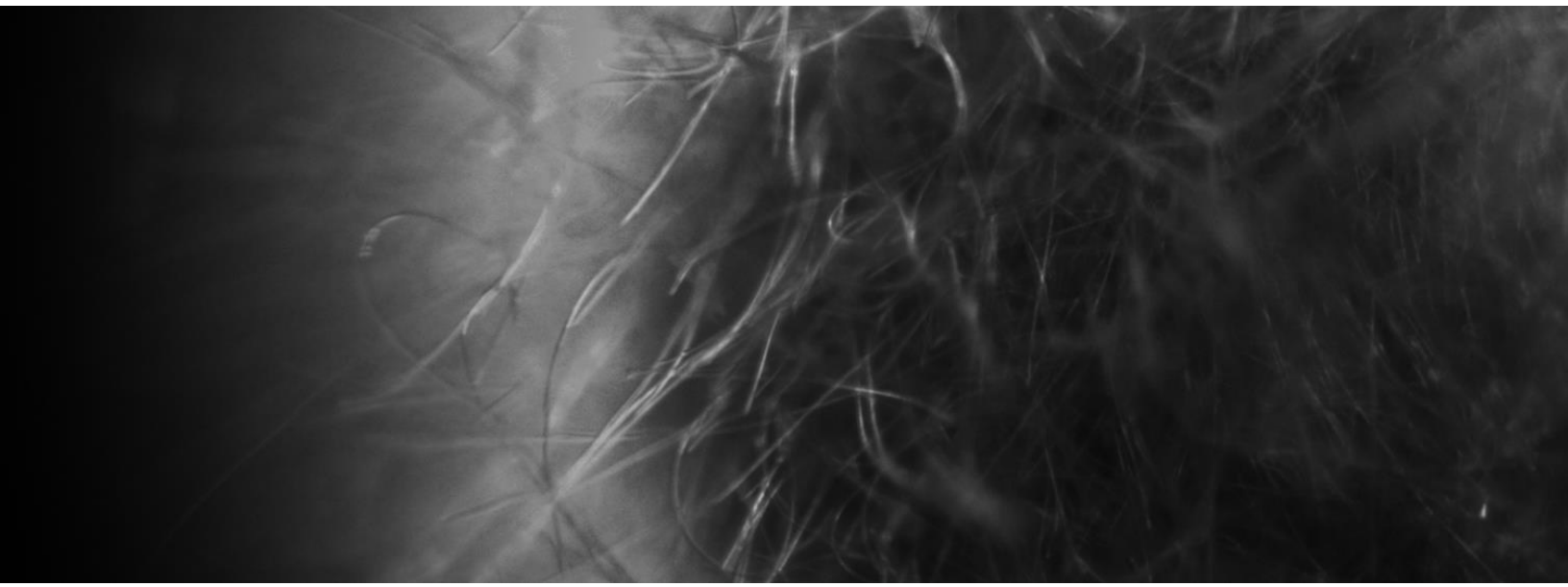

8

Perspectives

With my thesis, we are a step closer to understanding the minimum requirements for photogranulation, specifically the biological key players. However, we still do not know the exact mechanisms of photogranulation. In this chapter, I propose potential directions for further research.

8.1 Role of cyanobacterial characteristics in photogranulation

In **Chapter 5**, I hypothesized that photogranule-forming cyanobacterial strains are phylogenetically close. I am, however, not sure if this observation results from a sampling bias. I therefore suggest increasing the working set of photogranule-forming cyanobacteria by isolating filamentous cyanobacteria at an earlier stage of photogranule development. This may give us access to a larger diversity of putative photogranule-formers, and thus unravel if there is a specific trait responsible for photogranulation.

I started characterizing the cyanobacterial strains based on macroscopic and microscopic observations to identify the traits needed for photogranulation. I did not observe major differences in morphology between *Kamptonema*-like photogranule-forming strains and *Tychonema*-like mat-forming strains. Lacking a strong set of initial hypothesis for the mechanisms of photogranulation, I looked at a wide range of traits and may have overlooked relevant properties. Characteristics that I believe are important in photogranulation are gliding motility, e.g., speed and reversal frequency, filament flexibility and cell surface properties, e.g., EPS composition and abundance. Gliding motility is inherent to photogranulation: conditions that affect gliding motility affect photogranulation (Biddanda et al., 2015; Castenholz, 1967; Walsby, 1968). Brehm et al. (2003) showed that cyanobacteria moved fast towards, and quickly penetrated a developing sphere. Trichomes subsequently reduced their gliding speed and increased their reversal frequency to remain in the favorable sphere area. Trichomes bent to retain their position in modern microbialites (Sim et al., 2012). Gliding is furthermore reduced by a change in EPS composition. Fresh cultures produce mostly slime EPS, whereas older cultures produce mostly capsular EPS in the form of sheaths that reduce gliding motility (Hoiczyk, 1998). Reduced gliding motility of trichomes was observed with progressing hydrostatic photogranulation (Kuo-Dahab et al., 2018). Gliding motility, filament flexibility and cell surface properties could be compared between mat-, hemispheroid and photogranule-formers. These characteristics are not easily measured in a meaningful way, because they are affected by biotic and abiotic factors. I did not decide which method is best suited to measure these characteristics under conditions that match those of a developing spherical structure. Gliding speed can be measured as net displacement on a semi-solid agar plate, but it is more difficult to simulate movements into a developing 3D structure. Real-time microscopic movies are preferred over net displacement measurement to quantify reversal frequencies. Filament flexibility can be measured as the trichome bending angle on microscopic images. Measurements could be used as an input for mathematical modeling to test environmental parameters and predict the outcome in terms of spatial structure formation.

In hydrostatic photogranulation from activated sludge, enrichment of cyanobacteria is needed to produce sufficient biomass and trichome density to form the mat-like photoactive layer on the surface of the photogranule. Trichomes should be sufficiently long and strong to form a dense, interwoven network that can spatially organize itself and englobe the rest of the biomass. We could therefore compare cyanobacterial growth rate and yield, filament length and mechanical strength between photogranule-formers and mat-formers and between photogranules and mats.

Cyanobacteria can very well adapt to changing environmental conditions. I therefore suggest investigating the above (and below) mentioned characteristics in environmental conditions similar to those in hydrostatic batch cultivations, e.g., increase in (cyanobacterial) cell density, raise in pH, decrease in nutrients. I already observed that the photogranulation potential of cyanobacterial strains was dependent on the composition of culture medium and pH, possibly linked to the amount of biomass needed to form a photogranule.

8.2 Role of extracellular polymeric substances in photogranulation

EPS are needed for gliding motility and for the construction of stable spatial structures. Cell surface properties of trichomes that are important for aggregation also depend on EPS. A change in cell surface properties can change the binding ability of the filaments. A hydrophobic cell surface is needed to overcome the cells' negative cell charge for cell adhesion. EPS have furthermore gel-forming properties. During photogranulation, we observed jellification of the biomass. Differences in cell surface properties and jellification states could explain differences between photogranules, hemispheroids and mats and should be tested.

EPS production and biofilm formation and aggregation are regulated by N-acyl-homoserine lactones (quorum sensing molecules) and cyclic di-GMP (second messenger used in signal transduction), that are themselves regulated by population density and local environmental conditions (Srivastava and Waters, 2012). Cyclic di-GMP is furthermore involved in cyanobacterial motility (Agostoni et al., 2016; Wan et al., 2013). Brehm et al. (2003) demonstrated the role of chemotaxis in formation of laboratory microbialites: heterotrophic bacteria produced AHLs that attracted the trichomes. We could investigate the effect of addition AHLs and cyclic di-GMP on hydrostatic photogranulation.

8.3 Genomic potential of cyanobacteria

The trait that we are after may be "hidden". With whole-genome sequencing, we can reveal these hidden properties as long as the genes are annotated. Having the genomes available of photogranule-, hemispheroid- and mat-forming strains, we may be able to identify genes that are different between them, such as genes that code for proteins involved in gliding motility or aggregation. A challenge for the analysis of the genomes of our cyanobacterial strains is the presence of the DNA of their bacterial associates (Alvarenga et al., 2017). We should therefore remove bacterial DNA before analyzing the genomes of our cyanobacterial strains. With whole-genome sequencing, we obtain insight into the genomic potential, but we do not know which genes are expressed. To better understand the functional activities of our strains, we can perform proteomics to compare actual gene expression between photogranule-, hemispheroid- and mat-formers and identify proteins associated with ecosystem function, i.e., spatialization (Maron et al., 2007). An integrated multi-omics analysis allows the establishment of associations between the genetic potential and the final spatial structure (Narayanasamy et al., 2015).

8.4 Cyanobacterial roles in determination of the photogranule structure

I hypothesized that there is a succession of cyanobacteria in the development of the final spatial structure, based on the results of **Chapter 4** and **5**. I suggested studying community dynamics during morphotype development to learn at what point during photogranule development the photogranule-forming *Kamptonema*-like strain decreased in abundance and the mat-forming *Tychonema*-like strain took over. This is, however, challenging because we cannot know which morphotype would have formed in a sacrificed vial. This limitation is resolved now that I have

learnt that I can steer photogranulation by cyanobacterial augmentation. Insight into which strain was present at what stage of photogranule development contributes to our understanding of whether *Kamptonema*-like cyanobacteria built the photogranule structure themselves, or encouraged the community to do so through a legacy effect. *Kamptonema* may have been systematically outcompeted by *Tychonema* because of a strong selection pressure, e.g., constant high light intensity. Effect of light on community assembly and spatial structure formation should therefore be investigated. The experimental data can be used as input for individual based modeling to reconstruct cyanobacterial succession and predict which spatial structure will form depending on the initial community structure and prevailing experimental conditions.

8.5 Role of bacteria associated with cyanobacteria in photogranulation

Cyanobacteria and bacteria live in close association from which they mutually benefit. Also in photogranules, cyanobacteria and bacteria are localized in the same part of the photogranule (Ouazaite et al., 2021). Heterotrophs like to live on the cyanobacterial surface because it provides a support structure and access to carbon and oxygen. Bacteria provide cyanobacteria a carbon source and can furthermore help them to grow and aggregate e.g., by neutralizing the negative cell charge, producing EPS, and contributing to quorum sensing. Specific bacterial communities can be associated with cyanobacterial genera (Zhu et al., 2016). We found specific bacteria to be associated with our cyanobacterial strains. The role of bacteria in the formation of photogranules is unknown (Castenholz, 1967; Sim et al., 2012). We could study the interaction between cyanobacteria and bacteria in cultures by exchanging (engineering) bacterial communities and investigate their effect on photogranulation.

8.6 Role of headspace gas in hydrostatic photogranulation

A range of experiments that I performed with activated sludge is exchanging the air in the headspace of the vial by another gas, i.e., oxygen, CO_2, nitrogen or argon. I hypothesized that I could give cyanobacterial growth a kick-start by exchanging air with CO_2. It appeared, however, that photogranules did not form when the headspace consisted of CO_2, possibly because of the sharp drop in pH. In typical cultivations the pH increased from ~7 to ~10 through photosynthesis. Oxygen in the headspace resulted, however, in faster photogranulation than the control. An increased oxygen concentration in the bulk also promoted faster clumping in modern clumped photosynthetic mats (Sim et al., 2012). Anoxia in the headspace, i.e., argon or nitrogen, delayed the onset of contraction, but formed eventually photogranules. This indicates that headspace composition, or its effect on e.g., redox and pH gradients, are important for photogranulation. The role of redox and oxygen gradients in hydrostatic photogranulation should be investigated in the future. This could be achieved using microelectrodes coupled to mathematical modeling.

8.7 Modelling to couple cyanobacterial behavior to spatialization

Our model ecosystem is able to generate data at the microscale, e.g., from microelectrodes and microscopy, enabling us to further explore the development of spatial structures using mathematical modelling. Spatialization is an important but often disregarded feature of microbial ecosystems (Widder et al., 2016). Continuum spatial models to compute substrate gradients, paired with individual based models capturing the behavior of filamentous cyanobacteria, will provide insights in the assembly of this phototrophic ecosystem and consequences for ecosystem function. This knowledge may enable us to better understand photogranulation in nature and apply oxygenic photogranules in biotechnology.

References

Abed, R.M.M., Golubic, S., Garcia-Pichel, F., Camoin, G.F., Sprachta, S., 2003. Characterization of microbialite-forming cyanobacteria in a tropical lagoon: Tikehau Atoll, Tuamotu, French Polynesia. J. Phycol. 39, 862–873. https://doi.org/10.1046/j.1529-8817.2003.02180.x

Abouhend, A.S., McNair, A., Kuo-Dahab, W.C., Watt, C., Butler, C.S., Milferstedt, K., Hamelin, J., Seo, J., Gikonyo, G.J., El-Moselhy, K.M., Park, C., 2018. The oxygenic photogranule process for aeration-free wastewater treatment. Environ. Sci. Technol. 52, 3503–3511. https://doi.org/10.1021/acs.est.8b00403

Abouhend, A.S., Milferstedt, K., Hamelin, J., Ansari, A.A., Butler, C., Carbajal-González, B.I., Park, C., 2019. Growth progression of oxygenic photogranules and its impact on bioactivity for aeration-free wastewater treatment. Environ. Sci. Technol. 54, 486–496. https://doi.org/10.1021/acs.est.9b04745

Agostoni, M., Waters, C.M., Montgomery, B.L., 2016. Regulation of biofilm formation and cellular buoyancy through modulating intracellular cyclic di-GMP levels in engineered cyanobacteria 113, 311–319. https://doi.org/10.1002/bit.25712

Alberghini, S., Polone, E., Corich, V., Carlot, M., Seno, F., Trovato, A., Squartini, A., 2009. Consequences of relative cellular positioning on quorum sensing and bacterial cell-to-cell communication. FEMS Microbiol. Lett. 292, 149–161. https://doi.org/10.1111/j.1574-6968.2008.01478.x

Albrecht, M., Pröschold, T., Schumann, R., 2017. Identification of Cyanobacteria in a eutrophic coastal lagoon on the Southern Baltic Coast. Front. Microbiol. 8, 1–16. https://doi.org/10.3389/fmicb.2017.00923

Alvarenga, D.O., Fiore, M.F., Varani, A.M., 2017. A metagenomic approach to cyanobacterial genomics. Front. Microbiol. 8, 809. https://doi.org/10.3389/fmicb.2017.00809

Ammar, M., Comte, K., Tran, T.D.C., El Bour, M., 2014. Initial growth phases of two bloom-forming cyanobacteria (*Cylindrospermopsis raciborskii* and *Planktothrix agardhii*) in monocultures and mixed cultures depending on light and nutrient conditions. Int. J. Limnol. 50, 231–240. https://doi.org/10.1051/limn/2014096

Andersen, D.T., Sumner, D.Y., Hawes, I., Webster-Brown, J., Mckay, C.P., 2011. Discovery of large conical stromatolites in Lake Untersee, Antarctica. Geobiology 9, 280–293. https://doi.org/10.1111/j.1472-4669.2011.00279.x

Andersen, M.H., Mcilroy, S.J., Nierychlo, M., Nielsen, P.H., Albertsen, M., 2020. Genomic insights into *Candidatus* Amarolinea aalborgensis gen. nov., sp. nov., associated with settleability problems in wastewater treatment plants. Syst. Appl. Microbiol. 42, 77–84. https://doi.org/10.1016/j.syapm.2018.08.001

Anderson, M.J., 2001. A new method for non-parametric multivariate analysis of variance. Austral Ecol. 26, 32–46. https://doi.org/10.1046/j.1442-9993.2001.01070.x

Anderson, M.J., Willis, T.J., 2003. Canonical analysis of principal coordinates: a useful method of constrained ordination for ecology. Ecology 84, 511–525. https://doi.org/10.1890/0012-9658(2003)084[0511:CAOPCA]2.0.CO;2

Andres, M.S., Reid, R.P., 2006. Growth morphologies of modern marine stromatolites: a case study from Highborne Cay, Bahamas. Sediment. Geol. 185, 319–328. https://doi.org/10.1016/j.sedgeo.2005.12.020

Anesio, A.M., Lutz, S., Chrismas, N.A.M., Benning, L.G., 2017. The microbiome of glaciers and ice sheets. npj Biofilms Microbiomes 3, 1–11. https://doi.org/10.1038/s41522-017-0019-0

Ansari, A.A., Abouhend, A.S., Park, C., 2019. Effects of seeding density on photogranulation and the start-up of the oxygenic photogranule process for aeration-free wastewater treatment. Algal Res. 40, 101495. https://doi.org/10.1016/j.algal.2019.101495

Arcila, J.S., Buitrón, G., 2017. Influence of solar irradiance levels on the formation of microalgae-bacteria aggregates for municipal wastewater treatment. Algal Res. 27, 190–197. https://doi.org/10.1016/j.algal.2017.09.011

Arcila, J.S., Buitrón, G., 2016. Microalgae–bacteria aggregates: effect of the hydraulic retention time on the municipal wastewater treatment, biomass settleability and methane potential. J. Chem. Technol. Biotechnol. 91, 2862–2870. https://doi.org/10.1002/jctb.4901

Balskus, E.P., Case, R.J., Walsh, C.T., 2011. The biosynthesis of cyanobacterial sunscreen scytonemin in intertidal microbial mat communities. FEMS Microbiol. Ecol. 77, 322–332. https://doi.org/10.1111/j.1574-6941.2011.01113.x

Belnap, J., Gardner, J., 1993. Soil microstructure in soils of the Colorado Plateau: the role of the cyanobacterium *Microcoleus vaginatus*. West. North Am. Nat. 53, 40–47.

Berrendero, E., Perona, E., Mateo, P., 2008. Genetic and morphological characterization of *Rivularia* and *Calothrix* (Nostocales, Cyanobacteria) from running water. Int. J. Syst. Evol. Microbiol. 58, 447–460. https://doi.org/10.1099/ijs.0.65273-0

Biddanda, B.A., McMillan, A.C., Long, S.A., Snider, M.J., Weinke, A.D., 2015. Seeking sunlight: rapid phototactic motility of filamentous mat-forming cyanobacteria optimize photosynthesis and enhance carbon burial in Lake Huron's submerged sinkholes. Front. Microbiol. 6, 1–13. https://doi.org/10.3389/fmicb.2015.00930

Brehm, U., Krumbein, W.E., Palinska, K.A., 2006. Biomicrospheres generate ooids in the laboratory. Geomicrobiol. J. 23, 545–550. https://doi.org/10.1080/01490450600897302

Brehm, U., Krumbein, W.E., Palinska, K.A., 2003. Microbial spheres: a novel cyanobacterial-diatom symbiosis. Naturwissenschaften 90, 136–140. https://doi.org/10.1007/s00114-003-0403-x

Brehm, U., Palinska, K.A., Krumbein, W.E., 2004. Laboratory cultures of calcifying biomicrospheres generate ooids - a contribution to the origin of oolites. Carnets géologie (Notebooks Geol. https://doi.org/10.4267/2042/309

Bridier, A., Piard, J., Pandin, C., Labarthe, S., Dubois-brissonnet, F., Briandet, R., 2017. Spatial organization plasticity as an adaptive driver of surface microbial communities. Front. Microbiol. 8, 1364. https://doi.org/10.3389/fmicb.2017.01364

Brito, Â., Ramos, V., Mota, R., Lima, S., Santos, A., Vieira, J., Vieira, C.P., Kaštovský, J., Vasconcelos, V.M., Tamagnini, P., 2017. Description of new genera and species of marine cyanobacteria from the Portuguese Atlantic coast. Mol. Phylogenet. Evol. 111, 18–34. https://doi.org/10.1016/j.ympev.2017.03.006

Brockmann, D., Gérand, Y., Park, C., Milferstedt, K., Hélias, A., Hamelin, J., 2021. Wastewater treatment using oxygenic photogranule-based process has lower environmental impact than conventional activated sludge process. Bioresour. Technol. 319. https://doi.org/10.1016/j.biortech.2020.124204

Cai, W., Zhao, Z., Li, D., Lei, Z., Zhang, Z., Lee, D.J., 2019. Algae granulation for nutrients uptake and algae harvesting during wastewater treatment. Chemosphere 214, 55–59.

https://doi.org/10.1016/j.chemosphere.2018.09.107

Callahan, B.J., Wong, J., Heiner, C., Oh, S., Theriot, C.M., Gulati, A.S., McGill, S.K., Dougherty, M.K., 2019. High-throughput amplicon sequencing of the full-length 16S rRNA gene with single-nucleotide resolution. Nucleic Acids Res. 47, e103. https://doi.org/10.1093/nar/gkz569

Cameron, K.A., Hodson, A.J., Osborn, A.M., 2012. Structure and diversity of bacterial, eukaryotic and archaeal communities in glacial cryoconite holes from the Arctic and the Antarctic. FEMS Microbiol. Ecol. 82, 254–267. https://doi.org/10.1111/j.1574-6941.2011.01277.x

Castenholz, R.., 1982. Motility and Taxes, in: Carr, N., Whitton, B. (Eds.), The Biology of Cyanobacteria. Blackwell Scientific, pp. 413–439.

Castenholz, R.W., 1968. The behavior of *Oscillatoria terebriformis* in hot springs. J. Phycol. 4, 132–139. https://doi.org/10.1126/science.210.4466.182

Castenholz, R.W., 1967. Aggregation in a thermophilic *Oscillatoria*. Nature 215, 1285–1286. https://doi.org/10.1038/2151285a0

Castenholz, R.W., Rippka, R., Herdman, M., Wilmotte, A., 2015. Subsection III . Bergey's Man. Syst. Archaea Bact. 1–4. https://doi.org/10.1002/9781118960608.gbm00432

Charpy, L., Alliod, R., Rodier, M., Golubic, S., 2007. Benthic nitrogen fixation in the SW New Caledonia lagoon. Aquat. Microb. Ecol. 47, 73–81. https://doi.org/10.3354/ame047073

Charpy, L., Palinska, K.A., Abed, R.M.M., Langlade, M.J., Golubic, S., Charpy, L., Palinska, K.A., Abed, R.M.M., Langlade, M.J., 2012. Factors influencing microbial mat composition, distribution and dinitrogen fixation in three western Indian Ocean coral reefs. Eur. J. Phycol. 47, 51–66. https://doi.org/10.1080/09670262.2011.653652

Charpy, L., Palinska, K.A., Casareto, B., Langlade, M.J., Suzuki, Y., Abed, R.M.M., Golubic, S., 2010. Dinitrogen-fixing cyanobacteria in microbial mats of two shallow coral reef ecosystems. Microb. Ecol. 59, 174–186. https://doi.org/10.1007/s00248-009-9576-y

Chen, B.-Y., Chen, S.-Y., Lin, M.-Y., Chang, J.-S., 2006. Exploring bioaugmentation strategies for azo-dye decolorization using a mixed consortium of *Pseudomonas luteola* and *Escherichia coli*. Process Biochem. 41, 1574–1581. https://doi.org/10.1016/j.procbio.2006.03.004

Chet, I., Mitchell, R., 1976. Ecological aspects of microbial chemotactic behavior. Annu. Rev. Microbiol. 30, 221–239. https://doi.org/10.1146/annurev.mi.30.100176.001253

Christensen, B.E., 1989. The role of extracellular polysaccharides in biofilms. J. Biotechnol. 10, 181–202. https://doi.org/10.1016/0168-1656(89)90064-3

Christner, B.C., Kvitko, B.H., Reeve, J.N., 2003. Molecular identification of Bacteria and Eukarya inhabiting an Antarctic cryoconite hole. Extremophiles 7, 177–183. https://doi.org/10.1007/s00792-002-0309-0

Chu, Z., Jin, X., Iwami, N., Inamori, Y., 2007. The effect of temperature on growth characteristics and competitions of *Microcystis aeruginosa* and *Oscillatoria mougeotii* in a shallow, eutrophic lake simulator system, in: Eutrophication of Shallow Lakes with Special Reference to Lake Taihu, China. Springer Dordrecht, pp. 217–223. https://doi.org/10.1007/s10750-006-0506-4

Clarke, K.R., 1993. Non-parametric multivariate analyses of changes in community structure. Aust. J. Ecol. 18, 117–143. https://doi.org/10.1111/j.1442-9993.1993.tb00438.x

Danin, A., Dor, I., Sandler, A., Amit, R., 1998. Desert crust morphology and its relations to microbiotic succession at Mt. Sedom, Israel. J. Arid Environ. 38, 161–174. https://doi.org/https://doi.org/10.1006/jare.1997.0326

De Philippis, R., Sili, C., Paperi, R., Vincenzini, M., 2001. Exopolysaccharide-producing cyanobacteria and their possible exploitation: A review. J. Appl. Phycol. 13, 293–299. https://doi.org/10.1023/A:1017590425924

De Philippis, R., Vincenzini, M., 1998. Exocellular polysaccharides from cyanobacteria and their possible applications. FEMS Microbiol. Rev. 22, 151–175. https://doi.org/10.1016/S0168-6445(98)00012-6

De Winder, B., Staats, N., Stal, L.J., Paterson, D.M., 1999. Carbohydrate secretion by phototrophic communities in tidal sediments. J. Sea Res. 42, 131–146. https://doi.org/10.1016/S1385-1101(99)00021-0

Delucca, R., Mccracken, M.D., 1977. Observations on interactions between naturally-collected bacteria and several species of algae. Hydrobiologia 55, 71–75. https://doi.org/https://doi.org/10.1007/BF00034807

Edgar, R.C., Haas, B.J., Clemente, J.C., Quince, C., Knight, R., 2011. UCHIME improves sensitivity and speed of chimera detection. Bioinformatics 27, 2194–2200. https://doi.org/10.1093/bioinformatics/btr381

Edwards, A., Anesio, A.M., Rassner, S.M., Sattler, B., Hubbard, B., Perkins, W.T., Young, M., Griffith, G.W., 2011. Possible interactions between bacterial diversity, microbial activity and supraglacial hydrology of cryoconite holes in Svalbard. ISME J. 5, 150–160. https://doi.org/10.1038/ismej.2010.100

Edwards, A., Mur, L.A.J., Girdwood, S.E., Anesio, A.M., Stibal, M., Rassner, S.M.E., Hell, K., Pachebat, J.A., Post, B., Bussell, J.S., Cameron, S.J.S., Griffith, G.W., Hodson, A.J., Sattler, B., 2014. Coupled cryoconite ecosystem structure-function relationships are revealed by comparing bacterial communities in alpine and Arctic glaciers. FEMS Microbiol. Ecol. 89, 222–237. https://doi.org/10.1111/1574-6941.12283

Edwards, A., Pachebat, J.A., Swain, M., Hegarty, M., Hodson, A.J., Irvine-Fynn, T.D.L., Rassner, S.M.E., Sattler, B., 2013. A metagenomic snapshot of taxonomic and functional diversity in an alpine glacier cryoconite ecosystem. Environ. Res. Lett. 8, 035003. https://doi.org/10.1088/1748-9326/8/3/035003

Elias, S., Banin, E., 2012. Multi-species biofilms: living with friendly neighbors. FEMS Microbiol. Rev. 36, 990–1004. https://doi.org/10.1111/j.1574-6976.2012.00325.x

Estrela, S., Brown, S.P., 2013. Metabolic and demographic feedbacks shape the emergent spatial structure and function of microbial communities. PLoS Comput. Biol. 9, e1003398. https://doi.org/10.1371/journal.pcbi.1003398

Fang, F., Yang, L., Gan, L., Guo, L., Hu, Z., Yuan, S., Chen, Q., Jiang, L., 2014. DO, pH, and Eh microprofiles in cyanobacterial granules from Lake Taihu under different environmental conditions. J. Appl. Phycol. 26, 1689–1699. https://doi.org/10.1007/s10811-013-0211-4

Fattom, A., Shilo, M., 1984. Hydrophobicity as an adhesion mechanism of benthic cyanobacteria. Appl. Environ. Microbiol. 47, 135–143. https://doi.org/10.1128/aem.47.1.135-143.1984

Fenchel, T., Kühl, M., 2000. Artificial cyanobacterial mats: growth, structure, and vertical zonation patterns. Microb. Ecol. 40, 85–93. https://doi.org/10.1007/s002480000062

Flemming, H., Wingender, J., 2010. The biofilm matrix. Nat. Rev. Microbiol. 8, 623–633. https://doi.org/10.1038/nrmicro2415

Foster, J.S., Green, S.J., Ahrendt, S.R., Golubic, S., Reid, R.P., Hetherington, K.L., Bebout, L., 2009. Molecular and morphological characterization of cyanobacterial diversity in the stromatolites of Highborne Cay, Bahamas. ISME J. 3, 573–587. https://doi.org/10.1038/ismej.2008.129

Galetovic, A., Seura, F., Gallardo, V., Graves, R., Cortés, J., Valdivia, C., Nuñez, J., Tapia, C., Neira, I., Sanzana, S., Gómez-Silva, B., 2020. Use of phycobiliproteins from atacama cyanobacteria as food colorants in a dairy beverage prototype. Foods 9, 1–13. https://doi.org/10.3390/foods9020244

Garcia-Pichel, F., Castenholz, R.W., 2001. Photomovement of microorganisms in benthic and soil microenvironments, in: Häder, D.-P., Breure, A.M. (Eds.), Comprehensive Series in Photosciences. Elsevier, pp. 403–420. https://doi.org/10.1016/S1568-461X(01)80018-1

Garcia-Pichel, F., Loza, V., Marusenko, Y., Mateo, P., Potrafka, R.M., 2013. Temperature drives the continental-scale distribution of key microbes in topsoil communities. Science (80-.). 340, 1574–1577. https://doi.org/10.1126/science.1236404

Garcia-Pichel, F., Pringault, O., 2001. Microbiology: Cyanobacteria track water in desert soils. Nature 413, 380–381. https://doi.org/10.1038/35096640

Gerdel, R.W., Drouet, F., 1960. The cryoconite of the Thule area, Greenland. Trans. Am. Microsc. Soc. 79, 256. https://doi.org/10.2307/3223732

Golubic, S., Seong-Joo, L., Browne, K.M., 2000. Cyanobacteria: architects of sedimentary structures, in: Microbial Sediments. pp. 57–67. https://doi.org/10.1007/978-3-662-04036-2_8

Grewe, C.B., Pulz, O., 2012. The biotechnology of cyanobacteria, in: Whitton, B. (Ed.), Ecology of Cyanobacteria II. Springer Dordrecht, pp. 707–739. https://doi.org/10.1007/978-94-007-3855-3_26

Gupta, P., 2017. New record of Cyanoprokaryotes from West Bengal in Maldah district. Trop. Plant Res. 4, 421–432. https://doi.org/10.22271/tpr.2017.v4.i3.056

Gupta, S., Ross, T.D., Gomez, M.M., Grant, J.L., Romero, P.A., Venturelli, O.S., 2020. Investigating the dynamics of microbial consortia in spatially structured environments. Nat. Commun. 11, 1–15. https://doi.org/10.1038/s41467-020-16200-0

Gutzeit, G., Lorch, D., Weber, A., Engels, M., Neis, U., 2005. Bioflocculent algal-bacterial biomass improves low-cost wastewater treatment. Water Sci. Technol. 52, 9–18. https://doi.org/10.2166/wst.2005.0415

Guzmán-Soto, I., McTiernan, C., Gonzalez-Gomez, M., Ross, A., Gupta, K., Suuronen, E.J., Mah, T., Griffith, M., Alarcon, E.I., 2021. Mimicking biofilm formation and development: Recent progress in *in vitro* and *in vivo* biofilm models. Iscience 102443. https://doi.org/10.1016/j.isci.2021.102443

Häder, D.P., 1987. Photosensory behavior in procaryotes. Microbiol. Rev. 51, 1–21. https://doi.org/10.1128/mmbr.51.1.1-21.1987

Hanada, S., Hiraishi, A., Shimada, K., Matsuura, K., 1995. *Chloroflexus aggregans* sp. nov., a filamentous phototrophic bacterium which forms dense cell aggregates by active gliding movement. Int. J. Syst. Bacteriol. 45, 676–681. https://doi.org/10.1099/00207713-45-4-676

Havemann, S.A., Foster, J.S., 2008. Comparative characterization of the microbial diversities of

an artificial microbialite model and a natural stromatolite. Appl. Environ. Microbiol. 74, 7410–7421. https://doi.org/10.1128/AEM.01710-08

Herbst, V., 1978. Metabolic coupling between the alga Oscillatoria redekei and accompanying bacteria. Naturwissenschaften 65, 598–599. https://doi.org/https://doi.org/10.1007/BF00364919

Hodkinson, B.P., Lutzoni, F., 2009. A microbiotic survey of lichen-associated bacteria reveals a new lineage from the Rhizobiales. Symbiosis 49, 163–180. https://doi.org/10.1007/s13199-009-0049-3

Hodson, A., Anesio, A.M., Tranter, M., Fountain, A., Osborn, M., Priscu, J., Laybourn-Parry, J., Sattler, B., 2008. Glacial ecosystems. Ecol. Monogr. 78, 41–67.

Hodson, A., Cameron, K., Bøggild, C., Irvine-Fynn, T., Langford, H., Pearce, D., Banwart, S., 2010. The structure, biological activity and biogeochemistry of cryoconite aggregates upon an arctic valley glacier: Longyearbreen, Svalbard. J. Glaciol. 56, 349–362. https://doi.org/10.3189/002214310791968403

Hoiczyk, E., 2000. Gliding motility in cyanobacteria: observations and possible explanations. Arch. Microbiol. 174, 11–17. https://doi.org/10.1007/s002030000187

Hoiczyk, E., 1998. Structural and biochemical analysis of the sheath of *Phormidium uncinatum*. J. Bacteriol. 180, 3923–3932. https://doi.org/10.1128/jb.180.15.3923-3932.1998

Huang, W., Li, B., Zhang, C., Zhang, Z., Lei, Z., Lu, B., Zhou, B., 2015. Effect of algae growth on aerobic granulation and nutrients removal from synthetic wastewater by using sequencing batch reactors. Bioresour. Technol. 179, 187–192. https://doi.org/10.1016/j.biortech.2014.12.024

Hube, A.E., Heyduck-Söller, B., Fischer, U., 2009. Phylogenetic classification of heterotrophic bacteria associated with filamentous marine cyanobacteria in culture. Syst. Appl. Microbiol. 32, 256–265. https://doi.org/10.1016/j.syapm.2009.03.001

Irvine-Fynn, T.D.L., Bridge, J.W., Hodson, A.J., 2010. Rapid quantification of cryoconite: granule geometry and in situ supraglacial extents, using examples from Svalbard and Greenland. J. Glaciol. 56, 297–308. https://doi.org/10.3189/002214310791968421

Issa, O.M., Defarge, C., Bissonnais, Y. Le, Marin, B., Duval, O., Bruand, A., D'Acqui, L.P., Nordernberg, S., Annerman, M., 2007. Effects of the inoculation of cyanobacteria on the microstructure and the structural stability of a tropical soil. Plant Soil 290, 209–219. https://doi.org/10.1007/s11104-006-9153-9

Jefferson, K.K., 2004. What drives bacteria to produce a biofilm? FEMS Microbiol. Lett. 236, 163–173. https://doi.org/10.1016/j.femsle.2004.06.005

Jin, D., Wang, P., Bai, Z., Jin, B., Yu, Z., Wang, X., Zhuang, G., Zhang, H., 2013. *Terrimonas pekingensis* sp. nov., isolated from bulking sludge, and emended descriptions of the genus *Terrimonas*, *Terrimonas ferruginea*, *Terrimonas lutea* and *Terrimonas aquatica*. Int. J. Syst. Evol. Microbiol. 63, 1658–1664. https://doi.org/10.1099/ijs.0.036848-0

Johnson, J.S., Spakowicz, D.J., Hong, B.Y., Petersen, L.M., Demkowicz, P., Chen, L., Leopold, S.R., Hanson, B.M., Agresta, H.O., Gerstein, M., Sodergren, E., Weinstock, G.M., 2019. Evaluation of 16S rRNA gene sequencing for species and strain-level microbiome analysis. Nat. Commun. 10, 1–11. https://doi.org/10.1038/s41467-019-13036-1

Joosten, E.D., Hamelin, J., Milferstedt, K., 2020. Simple time-lapse imaging for quantifying the hydrostatic production of oxygenic photogranules. Bio-Protocol 10, e3784.

https://doi.org/10.21769/BioProtoc.3784

Kim, M., Shin, B., Lee, J., Park, H.Y., Park, W., 2019. Culture-independent and culture-dependent analyses of the bacterial community in the phycosphere of cyanobloom-forming *Microcystis aeruginosa*. Sci. Rep. 9, 1–13. https://doi.org/10.1038/s41598-019-56882-1

Komárek, J., 2018. Several problems of the polyphasic approach in the modern cyanobacterial system. Hydrobiologia 811, 7–17. https://doi.org/10.1007/s10750-017-3379-9

Komárek, J., 2016. A polyphasic approach for the taxonomy of cyanobacteria: principles and applications. Eur. J. Phycol. 51, 346–353. https://doi.org/10.1080/09670262.2016.1163738

Komárek, J., 2006. Cyanobacterial taxonomy: current problems and prospects for the integration of traditional and molecular approaches. Algae 21, 349–375. https://doi.org/10.4490/algae.2006.21.4.349

Komárek, J., Komárkova, J., 2004. Taxonomic review of the cyanoprokaryotic genera *Planktothrix* and *Planktothricoides*. Czech Phycol. Olomouc 1–18.

Konopka, A., 2006. Microbial ecology: searching for principles. Microbe 1, 175–179. https://doi.org/10.1128/microbe.1.175.1

Konopka, A., Carrero-Colon, M., Nakatsu, C.H., 2007. Community dynamics and heterogeneities in mixed bacterial communities subjected to nutrient periodicities. Environ. Microbiol. 9, 1584–1590. https://doi.org/10.1111/j.1462-2920.2007.01326.x

Kotai, J., 1972. Instructions for preparation of modified nutrient solution Z8 for algae. Nor. Inst. Water Res. Oslo 11, 5.

Kozich, J.J., Westcott, S.L., Baxter, N.T., Highlander, S.K., Schloss, P.D., 2013. Development of a dual-index sequencing strategy and curation pipeline for analyzing amplicon sequence data on the MiSeq Illumina sequencing platform. Appl. Environ. Microbiol. 79, 5112–5120. https://doi.org/10.1128/AEM.01043-13

Kreft, J.-U., Picioreanu, C., Wimpenny, J.W.T., van Loosdrecht, M.C.M., 2007. Individual-based modelling of biofilms. Microbiology 147, 2897–2912. https://doi.org/10.1099/00221287-147-11-2897

Kruschel, C., Castenholz, R.W., 1998. The effect of solar UV and visible irradiance on the vertical movements of cyanobacteria in microbial mats of hypersaline waters. FEMS Microbiol. Ecol. 27, 53–72. https://doi.org/10.1016/S0168-6496(98)00056-7

Kühl, M., Fenchel, T., Kazmierczak, J., 2003. Growth, structure and calcification potential of an artificial cyanobacterial mat, in: Fossil and Recent Biofilms, a Natural History of Life on Planet Earth. Springer Dordrecht, pp. 77–102. https://doi.org/10.1007/978-94-017-0193-8

Kumar, J., Singh, D., Tyagi, M.B., Kumar, A., 2019. Cyanobacteria: applications in biotechnology, in: Mishra, A.K., Tiwari, D.N., Rai, A.N.B.T.-C. (Eds.), Cyanobacteria: From Basic Science to Applications. Academic Press, pp. 327–346. https://doi.org/10.1016/B978-0-12-814667-5.00016-7

Kuo-Dahab, W.C., Stauch-White, K., Butler, C.S., Gikonyo, G.J., Carbajal-Gonzalez, B., Ivanova, A., Dolan, S., Park, C., 2018. Investigation of the fate and dynamics of extracellular polymeric substances (EPS) during sludge-based photogranulation under hydrostatic conditions. Environ. Sci. Technol. 52, 10462–10471. https://doi.org/10.1021/acs.est.8b03033

Kurmayer, R., Deng, L., Entfellner, E., 2016. Role of toxic and bioactive secondary metabolites in colonization and bloom formation by filamentous cyanobacteria *Planktothrix*. Harmful

Algae 54, 69–86. https://doi.org/10.1016/j.hal.2016.01.004

Kurobe, T., Lehman, P.W., Hammock, B.G., Bolotaolo, M.B., Lesmeister, S., Teh, S.J., 2018. Biodiversity of cyanobacteria and other aquatic microorganisms across a freshwater to brackish water gradient determined by shotgun metagenomic sequencing analysis in the San Francisco Estuary, USA. PLoS One 13, e0203953.

Lamparter, T., Babian, J., Fröhlich, K., Mielke, M., Weber, N., Wunsch, N., Zais, F., Schulz, K., Aschmann, V., Spohrer, N., Krauß, N., 2021. The involvement of type IV pili and phytochrome in gliding motility, lateral motility and phototaxis of the cyanobacterium *Phormidium lacuna*. bioRxiv. https://doi.org/https://doi.org/10.1101/2021.03.22.436410

Langford, H., Hodson, A., Banwart, S., Bøggild, C., 2010. The microstructure and biogeochemistry of Arctic cryoconite granules. Ann. Glaciol. 51, 87–94. https://doi.org/10.3189/172756411795932083

Legland, D., Arganda-Carreras, I., Andrey, P., 2016. MorphoLibJ: Integrated library and plugins for mathematical morphology with ImageJ. Bioinformatics 32, 3532–3534. https://doi.org/10.1093/bioinformatics/btw413

Leroy, F., De Vuyst, L., 2004. Lactic acid bacteria as functional starter cultures for the food fermentation industry. Trends Food Sci. Technol. 15, 67–78. https://doi.org/10.1016/j.tifs.2003.09.004

Liu, Y., Tay, J.H., 2002. The essential role of hydrodynamic shear force in the formation of biofilm and granular sludge. Water Res. 36, 1653–1665. https://doi.org/10.1016/S0043-1354(01)00379-7

Longo, S., D'Antoni, B.M., Bongards, M., Chaparro, A., Cronrath, A., Fatone, F., Lema, J.M., Mauricio-Iglesias, M., Soares, A., Hospido, A., 2016. Monitoring and diagnosis of energy consumption in wastewater treatment plants. A state of the art and proposals for improvement. Appl. Energy 179, 1251–1268. https://doi.org/10.1016/j.apenergy.2016.07.043

Loustau, E., Rols, J.L., Leflaive, J., Marcato-Romain, C.E., Girbal-Neuhauser, E., 2018. Comparison of extraction methods for the characterization of extracellular polymeric substances from aggregates of three biofilm-forming phototrophic microorganisms. Can. J. Microbiol. 64, 887–899. https://doi.org/10.1139/cjm-2018-0182

Mai, T., Johansen, J.R., Pietrasiak, N., Bohunická, M., Martin, M.P., 2018. Revision of the *Synechococcales* (Cyanobacteria) through recognition of four families including Oculatellaceae *fam. nov.* and Trichocoleaceae *fam. nov.* and six new genera containing 14 species. Phytotaxa 365, 1–59. https://doi.org/https://doi.org/10.11646/phytotaxa.365.1.1 ISSN

Malin, G., Walsby, A.E., 1985. Chemotaxis of a cyanobacterium on concentration gradients of carbon dioxide, bicarbonate and oxygen. J. Gen. Microbiol. 131, 2643–2652. https://doi.org/10.1099/00221287-131-10-2643

Maron, P.A., Ranjard, L., Mougel, C., Lemanceau, P., 2007. Metaproteomics: a new approach for studying functional microbial ecology. Microb. Ecol. 53, 486–493. https://doi.org/10.1007/s00248-006-9196-8

Martínez-García, R., Nadell, C.D., Hartmann, R., Drescher, K., Bonachela, J.A., 2018. Cell adhesion and fluid flow jointly initiate genotype spatial distribution in biofilms. PLoS Comput. Biol. 14, e1006094. https://doi.org/https://doi.org/10.1371/journal.pcbi.1006094

Masunga, G.S., Moe, S.R., Pelekekae, B., 2013. Distance-based tests for homogeneity of

multivariate dispersions. Ecosystems 16, 245–253. https://doi.org/10.1890/0012-9658(2001)082[3149:EOMGOS]2.0.CO;2

Mazor, G., Kidron, G.J., Vonshak, A., Abeliovich, A., 1996. The role of cyanobacterial exopolysaccharides in structuring desert microbial crusts. FEMS Microbiol. Ecol. 21, 121–130. https://doi.org/10.1016/0168-6496(96)00050-5

McMurdie, P.J., Holmes, S., 2013. Phyloseq: an R package for reproducible interactive analysis and graphics of microbiome census data. PLoS One 8, e61217. https://doi.org/10.1371/journal.pone.0061217

Milferstedt, K., Kuo-Dahab, W.C., Butler, C.S., Hamelin, J., Abouhend, A.S., Stauch-White, K., McNair, A., Watt, C., Carbajal-González, B.I., Dolan, S., Park, C., 2017. The importance of filamentous cyanobacteria in the development of oxygenic photogranules. Sci. Rep. 7, 17944. https://doi.org/10.1038/s41598-017-16614-9

Mohlin, M., Roleda, M.Y., Pattanaik, B., Tenne, S.J., Wulff, A., 2012. Interspecific resource competition-combined effects of radiation and nutrient limitation on two diazotrophic filamentous cyanobacteria. Microb. Ecol. 63, 736–750. https://doi.org/10.1007/s00248-011-9964-y

Momeni, B., Brileya, K.A., Fields, M.W., Shou, W., 2013a. Strong inter-population cooperation leads to partner intermixing in microbial communities. Elife 2, e00230. https://doi.org/10.7554/eLife.00230

Momeni, B., Waite, A.J., Shou, W., 2013b. Spatial self-organization favors heterotypic cooperation over cheating. Elife 2. https://doi.org/10.7554/eLife.00960

Moore, L.S., Burne, R. V., 1987. Microbialites: organosedimentary deposits of benthic microbial communities. Palaios 2, 241–254. https://doi.org/10.2307/3514674

Nadell, C.D., Drescher, K., Foster, K.R., 2016. Spatial structure, cooperation and competition in biofilms. Nat. Rev. Microbiol. 14, 589–600. https://doi.org/10.1038/nrmicro.2016.84

Nadell, C.D., Foster, K.R., Xavier, J.B., 2010. Emergence of spatial structure in cell groups and the evolution of cooperation. PLoS Comput. Biol. 6, e1000716. https://doi.org/10.1371/journal.pcbi.1000716

Narayanasamy, S., Muller, E.E.L., Sheik, A.R., Wilmes, P., 2015. Integrated omics for the identification of key functionalities in biological wastewater treatment microbial communities. Microb. Biotechnol. 8, 363–368. https://doi.org/10.1111/1751-7915.12255

Nguyen, N.-P., Warnow, T., Pop, M., White, B., 2016. Comparative integrated omics: identification of key functionalities in microbial community-wide metabolic networks. npj Biofilms Microbiomes 2, 1–8. https://doi.org/10.1038/npjbio

Nierychlo, M., Andersen, K.S., Xu, Y., Green, N., Jiang, C., Albertsen, M., Dueholm, M.S., Nielsen, P.H., 2020. MiDAS 3: an ecosystem-specific reference database, taxonomy and knowledge platform for activated sludge and anaerobic digesters reveals species-level microbiome composition of activated sludge. Water Res. 182, 115955.

Nierychlo, M., Miłobędzka, A., Petriglieri, F., McIlroy, B., Nielsen, P.H., McIlroy, S.J., 2019. The morphology and metabolic potential of the Chloroflexi in full-scale activated sludge wastewater treatment plants. FEMS Microbiol. Ecol. 95, fiy228. https://doi.org/10.1093/femsec/fiy228

Nübel, U., Garcia-Pichel, F., Muyzer, G., 1997. PCR primers to amplify 16S rRNA genes from cyanobacteria. Appl. Environ. Microbiol. 63, 3327–3332.

https://doi.org/10.1128/aem.63.8.3327-3332.1997

O'Brien, J., 2020. exiftoolr: ExifTool functionality from R. R Packag.

Oberhaus, L., Briand, J.F., Leboulanger, C., Jacquet, S., Humbert, J.F., 2007. Comparative effects of the quality and quantity of light and temperature on the growth of *Planktothrix agardhii* and *P. rubescens*. J. P 43, 1191–1199. https://doi.org/10.1111/j.1529-8817.2007.00414.x

Oksanen, J., Blanchet, F.G., Friendly, M., Kindt, R., Legendre, P., McGlinn, D., Minchin, P.R., O'Hara, R.B., Simpson, G.L., Solymos, P., Stevens, M.H.H., Szoecs, E., Wager, H., 2019. vegan: community ecology package. R Packag. version, 2.5-6.

Ouazaite, H., Desmond-Le Quéméner, E., Hamelin, J., Picioreanu, C., Lamb, J.J., Milferstedt, K., n.d. Light as a microenvironmental control for carbon conversion using oxygenic photogranules. Water Res. submitted.

Ouazaite, H., Milferstedt, K., Hamelin, J., Desmond-Le Quéméner, E., 2021. Mapping the biological activities of filamentous oxygenic photogranules. Biotechnol. Bioeng. 118, 601–611. https://doi.org/10.1002/bit.27585

Paerl, H.W., Bebout, B.M., Prufert, L.E., 1989. Bacterial associations with marine *Oscillatoria* sp. (*Trichodesmium* sp.) populations: ecophysiological implications. J. Phycol. 25, 773–784.

Paerl, H.W., Priscu, J.C., 1998. Microbial phototrophic, heterotrophic, and diazotrophic activities associated with aggregates in the permanent ice cover of Lake Bonney, Antarctica. Microb. Ecol. 36, 221–230. https://doi.org/10.1007/s002489900109

Pagaling, E., Strathdee, F., Spears, B.M., Cates, M.E., Allen, R.J., Free, A., 2014. Community history affects the predictability of microbial ecosystem development. ISME J. 8, 19–30. https://doi.org/10.1038/ismej.2013.150

Palińska, K.A., Abed, R.M.M., Charpy, L., Langlade, M.J., Beltrán-Magos, Y., Golubic, S., 2015. Morphological, genetic and physiological characterization of *Hydrocoleum*, the most common benthic cyanobacterium in tropical oceans. Eur. J. Phycol. 50, 139–154. https://doi.org/10.1080/09670262.2015.1010239

Palinska, K.A., Surosz, W., 2014. Taxonomy of cyanobacteria: a contribution to consensus approach. Hydrobiologia 740, 1–11. https://doi.org/10.1007/s10750-014-1971-9

Park, C. & Dolan, S., 2015. Algal-sludge granule for wastewater treatment and bioenergy feedstock generation. Pat. Appl. WO 2015112654 A2, Appl. number PCT/US2015/012332.

Park, S., Wolanin, P.M., Yuzbashyan, E.A., Lin, H., Darnton, N.C., Stock, J.B., Silberzan, P., Austin, R., 2003. Influence of topology on bacterial social interaction. PNAS 100, 13910–13915. https://doi.org/10.1073/pnas.1935975100

Pentecost, A., 1984. Effects of sedimentation and light intensity on mat-forming *Oscillatoriaceae* with particular reference to *Microcoleus lyngbyaceus* Gomont. J. Gen. Microbiol. 130, 983–990. https://doi.org/10.1099/00221287-130-4-983

Pereira, S.B., Mota, R., Vieira, C.P., Vieira, J., Tamagnini, P., 2015. Phylum-wide analysis of genes/ proteins related to the last steps of assembly and export of extracellular polymeric substances (EPS) in cyanobacteria. Sci. Rep. 5, 1–16. https://doi.org/10.1038/srep14835

Pessi, I.S., Pushkareva, E., Lara, Y., Borderie, F., Wilmotte, A., Elster, J., 2019. Marked succession of cyanobacterial communities following glacier retreat in the High Arctic. Microb. Ecol. 77, 136–147. https://doi.org/10.1007/s00248-018-1203-3

Petroff, A.P., Sub, M., Maslov, A., Krupenin, M., Rothman, D.H., Bosak, T., 2010. Biophysical basis for the geometry of conical stromatolites. PNAS 107, 9956–9961. https://doi.org/10.1073/pnas.1001973107

Pinto, F., Tett, A., F., Armanini, F., Asnicar, A., B., Pasolli, E., Zolfo, M., Donati, C., Salmaso, N., Segata, N., 2018. Draft genome sequences of novel *Pseudomonas*, *Flavobacterium*, and *Sediminibacterium* species strains from a freshwater ecosystem. Genome Announc. 6, e00009-18.

Porazinska, D.L., Fountain, A.G., Nylen, T.H., Tranter, M., Virginia, R.A., Wall, D.H., 2004. The biodiversity and biogeochemistry of cryoconite holes from McMurdo Dry Valley glaciers, Antarctica. Arctic, Antarct. Alp. Res. 36, 84–91. https://doi.org/10.1657/1523-0430(2004)036[0084:TBABOC]2.0.CO;2

Pratt, L.A., Kolter, R., 1998. Genetic analysis of *Escherichia coli* biofilm formation: roles of flagella, motility, chemotaxis and type I pili. Mol. Microbiol. 30, 285–293. https://doi.org/10.1046/j.1365-2958.1998.01061.x

Prieto-Barajas, C.M., Valencia-Cantero, E., Santoyo, G., 2018. Microbial mat ecosystems: Structure types, functional diversity, and biotechnological application. Electron. J. Biotechnol. 31, 48–56. https://doi.org/10.1016/j.ejbt.2017.11.001

Prufert-Bebout, L., Paerl, H.W., Lassen, C., 1993. Growth, nitrogen fixation, and spectral attenuation in cultivated Trichodesmi. Microbiology 1367–1375.

Quast, C., Pruesse, E., Yilmaz, P., Gerken, J., Schweer, T., Yarza, P., Peplies, J., Glöckner, F.O., 2013. The SILVA ribosomal RNA gene database project: improved data processing and web-based tools. Nucleic Acids Res. 41, 590–596. https://doi.org/10.1093/nar/gks1219

Quijano, G., Arcila, J.S., Buitrón, G., 2017. Microalgal-bacterial aggregates: applications and perspectives for wastewater treatment. Biotechnol. Adv. 35, 772–781. https://doi.org/10.1016/j.biotechadv.2017.07.003

R core development team, 2019. A Language and Environment for Statistical Computing. R Found. Stat. Comput.

Radzi, R., Muangmai, N., Broady, P., Wan Omar, W.M., Lavoue, S., Convery, P., Merican, F., 2019. *Nodosilinea signiensis* sp. nov. (Leptolyngbyaceae, Synechococcales), a new terrestrial cyanobacterium isolated from mats collected on Signy Island, South Orkney Islands, Antarctica. PLoS One 14, e0224395. https://doi.org/10.1371/journal.pone.0224395

Ramos, V., Morais, J., Vasconcelos, V.M., 2017. A curated database of cyanobacterial strains relevant for modern taxonomy and phylogenetic studies. Sci. Data 4. https://doi.org/10.1038/sdata.2017.54

Ramsing, N.B., Prufert-Bebout, L., 1994. Motility of *Microcoleus chthonoplastes* subjected to different light intensities quantified by digital image analysis, in: Microbial Mats. pp. 183–191. https://doi.org/10.1007/978-3-642-78991-5_19

Reid, R.P., Visscher, P.T., Decho, A.W., Stolz, J.F., Bebout, B.M., Dupraz, C., Macintyre, I.G., Paerl, H.W., Pinckney, J.L., Prufert-Bebout, L., Steppe, T.F., DesMarais, D.J., 2000. The role of microbes in accretion, lamination and early lithification of modern marine stromatolites. Nature 406, 989–992. https://doi.org/10.1038/35023158

Richardson, L.L., Castenholz, R.W., 1989. Chemokinetic motility responses of the cyanobacterium *Oscillatoria terebriformis*. Appl. Environ. Microbiol. 55, 261–263. https://doi.org/10.1128/aem.55.1.261-263.1989

Richardson, L.L., Castenholz, R.W., 1987. Diel vertical movements of the cyanobacterium *Oscillatoria terebriformis* in a sulfide-rich hot spring microbial mat. Appl. Environ. Microbiol. 53, 2142–2150. https://doi.org/10.1128/aem.53.9.2142-2150.1987

Rippka, R., 1988. Isolation and Purification of Cyanobacteria. Methods Enzymol. 167, 3–27. https://doi.org/10.1016/0076-6879(88)67004-2

Rippka, R., Deruelles, J., Waterbury, J.B., 1979. Generic assignments, strain histories and properties of pure cultures of cyanobacteria. J. Gen. Microbiol. 111, 1–61. https://doi.org/10.1099/00221287-111-1-1

Roeselers, G., van Loosdrecht, M.C.M., Muyzer, G., 2008. Phototrophic biofilms and their potential applications. J. Appl. Phycol. 20, 227–235. https://doi.org/10.1007/s10811-007-9223-2

Rossi, F., De Philippis, R., 2015. Role of cyanobacterial exopolysaccharides in phototrophic biofilms and in complex microbial mats. Life 5, 1218–1238. https://doi.org/10.3390/life5021218

Safitri, A.S., Hamelin, J., Kommedal, R., Milferstedt, K., 2021. Engineered methanotrophic syntrophy in photogranule communities removes dissolved methane. Water Res. X in press. https://doi.org/https://doi.org/10.1016/j.wroa.2021.100106

Sarma, S.J., Tay, J.H., Chu, A., 2017. Finding knowledge gaps in aerobic granulation technology. Trends Biotechnol. 35, 66–78. https://doi.org/10.1016/j.tibtech.2016.07.003

Schloss, P.D., Westcott, S.L., Ryabin, T., Hall, J.R., Hartmann, M., Hollister, E.B., Lesniewski, R.A., Oakley, B.B., Parks, D.H., Robinson, C.J., Sahl, J.W., Stres, B., Thallinger, G.G., Van Horn, D.J., Weber, C.F., 2009. Introducing mothur: open-source, platform-independent, community-supported software for describing and comparing microbial communities. Appl. Environ. Microbiol. 75, 7537–7541. https://doi.org/10.1128/AEM.01541-09

Schmid, M., Thill, A., Purkhold, U., Walcher, M., Bottero, J.-Y., Ginestet, P., Nielsen, P.H., Wuertz, S., Wagner, M., 2003. Characterization of activated sludge flocs by confocal laser scanning microscopy and image analysis. Water Res. 37, 2043–2052. https://doi.org/10.1016/S0043-1354(02)00616-4

Schneider, C., Rasband, W., Eliceiri, K., 2012. NIH Image to ImageJ: 25 years of image analysis. Nat. Methods 9, 671–675. https://doi.org/10.1007/978-1-84882-087-6_9

Segawa, T., Takeuchi, N., 2010. Cyanobacterial communities on Qiyi glacier, Qilian Shan , China. Ann. Glaciol. 51, 135–144. https://doi.org/https://doi.org/10.3189/172756411795932047

Shao, J., Peng, L., Luo, S., Yu, G., Gu, J., Lin, S., Li, R., 2013. First report on the allelopathic effect of *Tychonema bourrellyi* (Cyanobacteria) against *Microcystis aeruginosa* (Cyanobacteria). J. Appl. Phycol. 25, 1567–1573. https://doi.org/10.1007/s10811-012-9969-z

Shepard, R.N., Sumner, D.Y., 2010. Undirected motility of filamentous cyanobacteria produces reticulate mats. Geobiology 8, 179–190. https://doi.org/10.1111/j.1472-4669.2010.00235.x

Sherwood, A.R., Presting, G.G., 2007. Universal primers amplify a 23S rDNA plastid marker in eukaryotic algae and cyanobacteria. J. Phycol. 43, 605–608. https://doi.org/10.1111/j.1529-8817.2007.00341.x

Shiels, K., Browne, N., Donovan, F., Murray, P., Saha, S.K., 2019. Molecular characterization of twenty-five marine cyanobacteria isolated from coastal regions of Ireland. Biology (Basel).

8, 59. https://doi.org/10.3390/biology8030059

Sigler, W. V, Zeyer, J., 2004. Colony-forming analysis of bacterial community succession in deglaciated soils indicates pioneer stress-tolerant opportunists. Microb. Ecol. 48, 316–323. https://doi.org/10.1007/s00248-003-0189-6

Sihvonen, L.M., Lyra, C., Fewer, D.P., Rajaniemi-wacklin, P., Lehtim, J.M., Wahlsten, M., Sivonen, K., 2007. Strains of the cyanobacterial genera *Calothrix* and *Rivularia* isolated from the Baltic Sea display cryptic diversity and are distantly related to *Gloeotrichia* and *Tolypothrix*. FEMS Microbiol. Ecol. 61, 74–84. https://doi.org/10.1111/j.1574-6941.2007.00321.x

Silva-Benavides, A.M., Torzillo, G., 2012. Nitrogen and phosphorus removal through laboratory batch cultures of microalga *Chlorella vulgaris* and cyanobacterium *Planktothrix isothrix* grown as monoalgal and as co-cultures. J. Appl. Phycol. 24, 267–276. https://doi.org/10.1007/s10811-011-9675-2

Sim, M.S., Liang, B., Petroff, A.P., Evans, A., Klepac-Ceraj, V., Flannery, D.T., Walter, M.R., Bosak, T., 2012. Oxygen-dependent morphogenesis of modern clumped photosynthetic mats and implications for the archean stromatolite record. Geosciences 2, 235–259. https://doi.org/10.3390/geosciences2040235

Singh, J., Thakur, I.S., 2015. Evaluation of cyanobacterial endolith *Leptolyngbya* sp. ISTCY101, for integrated wastewater treatment and biodiesel production: a toxicological perspective. Algal Res. 11, 294–303. https://doi.org/10.1016/j.algal.2015.07.010

Soejima, A., Yamazaki, N., Nishino, T., Wakana, I., 2009. Genetic variation and structure of the endangered freshwater benthic alga Marimo, *Aegagropila linnaei* (Ulvophyceae) in Japanese lakes. Aquat. Ecol. 43, 359–370. https://doi.org/10.1007/s10452-008-9204-9

Sprachta, S., Camoin, G., Golubic, S., Le Campion, T., 2001. Microbialites in a modern lagoonal environment: nature and distribution, Tikehau atoll (French Polynesia). Palaeogeogr. Palaeoclimatol. Palaeoecol. 175, 103–124. https://doi.org/10.1016/S0031-0182(01)00388-1

Springstein, B.L., Woehle, C., Weissenbach, J., Helbig, A.O., Tal, D., Karina, S., 2020. Identification and characterization of novel filament-forming proteins in cyanobacteria. Sci. Rep. 10, 1–17. https://doi.org/10.1038/s41598-020-58726-9

Srivastava, D., Waters, C.M., 2012. A tangled web: Regulatory connections between quorum sensing and cyclic di-GMP. J. Bacteriol. 194, 4485–4493. https://doi.org/10.1128/JB.00379-12

Stal, L.J., 1995. Physiological ecology of cyanobacteria in microbial mats and other communities. New Phytol. https://doi.org/10.1111/j.1469-8137.1995.tb03051.x

Stal, L.J., van Gemerden, H., Krumbein, W.E., 1985. Structure and development of a benthic marine microbial mat. FEMS Microbiol. Lett. 31, 111–125. https://doi.org/10.1016/0378-1097(85)90007-2

Stauch-White, K., Srinivasan, V.N., Camilla Kuo-Dahab, W., Park, C., Butler, C.S., 2017. The role of inorganic nitrogen in successful formation of granular biofilms for wastewater treatment that support cyanobacteria and bacteria. AMB Express 7, 1–10. https://doi.org/10.1186/s13568-017-0444-8

Stibal, M., Sabacka, M., Zarsky, J., 2012. Biological processes on glacier and ice sheet surfaces. Nat. Geosci. 1–4. https://doi.org/10.1038/NGEO1611

Stibal, M., Schostag, M., Cameron, K.A., Hansen, L.H., Chandler, D.M., Wadham, J.L.,

Jacobsen, C.S., 2015. Different bulk and active bacterial communities in cryoconite from the margin and interior of the Greenland ice sheet. Environ. Microbiol. Rep. 7, 293–300. https://doi.org/10.1111/1758-2229.12246

Strunecky, O., Komárek, J., Šmarda, J., 2014. *Kamptonema* (*Microcoleaceae*, *Cyanobacteria*), a new genus derived from the polyphyletic *Phormidium* on the basis of combined molecular and cytomorphological markers. Preslia 193–207.

Tabacchioni, S., Chiarini, L., Bevivino, A., Cantale, C., Dalmastri, C., 2000. Bias caused by using different isolation media for assessing the genetic diversity of a natural microbial population. Microb. Ecol. 40, 169–176. https://doi.org/10.1007/s002480000015

Takeuchi, N., Kohshima, S., Seko, K., 2001. Structure, formation, and darkening process of albedo-reducing material (cryoconite) on a Himalayan glacier: a granular algal mat growing on the glacier. Arctic, Antarct. Alp. Res. 33, 115–122. https://doi.org/10.2307/1552211

Takeuchi, N., Nishiyama, H., Li, Z., 2010. Structure and formation process of cryoconite granules on Ürümqi glacier No. 1, Tien Shan, China. Ann. Glaciol. 51, 9–14. https://doi.org/10.3189/172756411795932010

Tamulonis, C., Kaandorp, J., 2014. A model of filamentous cyanobacteria leading to reticulate pattern formation. Life 4, 433–456. https://doi.org/10.3390/life4030433

Tamulonis, C., Postma, M., Kaandorp, J., 2011. Modeling filamentous cyanobacteria reveals the advantages of long and fast trichomes for optimizing light exposure. PLoS One 6, 1–12. https://doi.org/10.1371/journal.pone.0022084

Tay, J.H., Liu, Q.S., Liu, Y., 2001. The effects of shear force on the formation, structure and metabolism of aerobic granules. Appl. Microbiol. Biotechnol. 57, 227–233. https://doi.org/10.1007/s002530100766

Tiron, O., Bumbac, C., Manea, E., Stefanescu, M., Lazar, M.N., 2017. Overcoming microalgae harvesting barrier by activated algae granules. Sci. Rep. 7, 1–11. https://doi.org/10.1038/s41598-017-05027-3

Tiron, O., Bumbac, C., Patroescu, I. V., Badescu, V.R., Postolache, C., 2015. Granular activated algae for wastewater treatment. Water Sci. Technol. 71, 832–839. https://doi.org/10.2166/wst.2015.010

Togashi, T., Sasaki, H., Yoshimura, J., 2014. A geometrical approach explains Lake Ball (Marimo) formations in the green alga, *Aegagropila linnaei*. Sci. Rep. 4, 1–5. https://doi.org/10.1038/srep03761

Trebuch, L.M., Oyserman, B.O., Janssen, M., Wijffels, R.H., Vet, L.E.M., Fernandes, T. V., 2020. Impact of hydraulic retention time on community assembly and function of photogranules for wastewater treatment. Water Res. 173, 115506. https://doi.org/10.1016/j.watres.2020.115506

Urbach, E., Robertson, D.L., Chrisholm, S.W., 1992. Multiple evolutionary origins of prochlorophytes, the chlorophyll b-containing prokaryotes. Nature 355, 265–267. https://doi.org/10.1038/355265a0

Van de Waal, D.B., Verspagen, J.M.H., Finke, J.F., Vournazou, V., Immers, A.K., Kardinaal, W.E.A., Tonk, L., Becker, S., van Donk, E., Visser, P.M., Huisman, J., 2011. Reversal in competitive dominance of a toxic versus non-toxic cyanobacterium in response to rising CO_2. ISME J. 5, 1438–1450. https://doi.org/10.1038/ismej.2011.28

Van Den Hende, S., Carré, E., Cocaud, E., Beelen, V., Boon, N., Vervaeren, H., 2014.

Treatment of industrial wastewaters by microalgal bacterial flocs in sequencing batch reactors. Bioresour. Technol. 161, 245–254. https://doi.org/10.1016/j.biortech.2014.03.057

Vass, M., Langenheder, S., 2017. The legacy of the past: effects of historical processes on microbial metacommunities. Aquat. Microb. Ecol. 79, 13–19. https://doi.org/10.3354/ame01816

Walsby, A.E., 1968. Mucilage secretion and the movements of blue-green algae. Protoplasma 65, 223–238. https://doi.org/10.1007/BF01666380

Walter, M.R., Bauld, J., Brock, T.D., 1976. Microbiology and morphogenesis of columnar stromatolites (*Conophyton, Vacerrilla*) from hot springs in Yellowstone National Park, in: Developments in Sedimentology. pp. 273–310. https://doi.org/10.1016/S0070-4571(08)71140-3

Wan, C., Zhang, P., Lee, D., Yang, X., Liu, X., Sun, S., Pan, X., 2013. Disintegration of aerobic granules: role of second messenger cyclic di-GMP. Bioresour. Technol. 146, 330–335. https://doi.org/10.1016/j.biortech.2013.07.073

Wang, Y., Qian, P.Y., 2009. Conservative fragments in bacterial 16S rRNA genes and primer design for 16S ribosomal DNA amplicons in metagenomic studies. PLoS One 4. https://doi.org/10.1371/journal.pone.0007401

Ward, D.M., Weller, R., Bateson, M.M., 1990. 16S rRNA sequences reveal uncultured inhabitants of a well-studied thermal community. FEMS Microbiol. Lett. 75, 105–115. https://doi.org/10.1038/345063a0

Whale, G.F., Walsby, A.E., 1984. Motility of the cyanobacterium *Microcoleus chthonoplastes* in mud. Br. Phycol. J. 19, 117–123. https://doi.org/10.1080/00071618400650121

Wharton, R.A., McKay, C.P., Simmons, G.M., Parker, B.C., 1985. Cryoconite holes on glaciers. Bioscience 35, 499–503. https://doi.org/10.2307/1309818

Wickham, H., 2016. ggplot2: elegant graphics for data analysis. Springer International Publishing. https://doi.org/10.1007/978-3-319-24277-4

Wickham, H., 2011. The split-apply-combine strategy for data analysis. J. Stat. Software, 40(1), 1-29. URL http//www.jstatsoft.org/v40/i01/.

Wickham, H., François, R., Henry, L., Müller, K., 2019. dplyr: a grammar of data manipulation. R Packag.

Wickham, H., Hester, J., Francois, R., 2018. readr: read rectangular text data. R Packag.

Widder, S., Allen, R.J., Pfeiffer, T., Curtis, T.P., Wiuf, C., Sloan, W.T., Cordero, O.X., Brown, S.P., Momeni, B., Shou, W., Kettle, H., Flint, H.J., Haas, A.F., Laroche, B., Kreft, J.U., Rainey, P.B., Freilich, S., Schuster, S., Milferstedt, K., Van Der Meer, J.R., Grobkopf, T., Huisman, J., Free, A., Picioreanu, C., Quince, C., Klapper, I., Labarthe, S., Smets, B.F., Wang, H., Soyer, O.S., 2016. Challenges in microbial ecology: building predictive understanding of community function and dynamics. ISME J. 10, 2557–2568. https://doi.org/10.1038/ismej.2016.45

Wilbanks, E.G., Jaekel, U., Salman, V., Humphrey, P.T., Eisen, J.A., Facciotti, M.T., Buckley, D.H., Zinder, S.H., Druschel, G.K., Fike, D.A., Orphan, V.J., 2014. Microscale sulfur cycling in the phototrophic pink berry consortia of the Sippewissett Salt Marsh. Environ. Microbiol. 16, 3398–3415. https://doi.org/10.1111/1462-2920.12388

Wilmotte, A., Dail Laughinghouse IV, H., Capelli, C., Rippka, R., Salmaso, N., 2017. Taxonomic identification of cyanobacteria by a polyphasic approach, in: Kurmayer, R., Sivonen, K.,

Wilmotte, A., Salmaso, N (Eds.), Molecular Tools for the Detection and Quantification of Toxigenic Cyanobacteria. Wiley, pp. 79–134. https://doi.org/10.1002/9781119332169.ch4

Wingender, J., Neu, T.R., Flemming, H.C., 1999. What are bacterial extracellular polymeric substances?, in: Microbial Extracellular Polymeric Substances. Springer, Berlin, Heidelberg., pp. 1–19. https://doi.org/https://doi.org/10.1007/978-3-642-60147-7_1

Wong, H.L., Smith, D., Visscher, P.T., Burns, B.P., 2015. Niche differentiation of bacterial communities at a millimeter scale in Shark Bay microbial mats. Sci. Rep. 5, 1–17. https://doi.org/10.1038/srep15607

Xiang, S.-R., Shang, T.-C., Chen, Y., Jing, Z.-F., Yao, T., 2009. Dominant bacteria and biomass in the Kuytun 51 Glacier. Appl. Environ. Microbiol. 75, 7287–7290. https://doi.org/10.1128/AEM.00915-09

Yang, C., Zhang, W., Liu, R., Li, Q., Li, B., Wang, S., Song, C., Qiao, C., Mulchandani, A., 2011. Phylogenetic diversity and metabolic potential of activated sludge microbial communities in full-scale wastewater treatment plants. Environ. Sci. Technol. 45, 7408–7415. https://doi.org/10.1111/j.1574-6968.1990.tb04088.x

Yanni, D., Márquez-Zacarías, P., Yunker, P.J., Ratcliff, W.C., 2019. Drivers of spatial structure in social microbial communities. Curr. Biol. 29, R545–R550. https://doi.org/10.1016/j.cub.2019.03.068

Yu, Y., Lee, C., Kim, J., Hwang, S., 2005. Group-specific primer and probe sets to detect methanogenic communities using quantitative real-time polymerase chain reaction. Biotechnol. Bioeng. 89, 670–679. https://doi.org/10.1002/bit.20347

Zarsky, J.D., Stibal, M., Hodson, A., Sattler, B., Schostag, M., Hansen, L.H., Jacobsen, C.S., Psenner, R., 2013. Large cryoconite aggregates on a Svalbard glacier support a diverse microbial community including ammonia-oxidizing archaea. Environ. Res. Lett. 8, 035000. https://doi.org/10.1088/1748-9326/8/3/035044

Zeng, Y.-X., Yan, M., Yu, Y., Li, H.-R., He, J.-F., Sun, K., Zhang, F., 2013. Diversity of bacteria in surface ice of Austre Lovénbreen glacier, Svalbard. Arch. Microbiol. 195, 313–322. https://doi.org/10.1007/s00203-013-0880-z

Zhou, J., Ning, D., 2017. Stochastic community assembly: does it matter in microbial ecology? Microbiol. Mol. Biol. Rev. 81, e00002-17. https://doi.org/10.1128/MMBR.00002-17

Zhu, L., Zancarini, A., Louati, I., De Cesare, S., Duval, C., Tambosco, K., Bernard, C., Debroas, D., Song, L., Leloup, J., Humbert, J.F., 2016. Bacterial communities associated with four cyanobacterial genera display structural and functional differences: Evidence from an experimental approach. Front. Microbiol. 7, 1–11. https://doi.org/10.3389/fmicb.2016.01662

Zubia, M., Turquet, J., Golubic, S., 2016. Benthic cyanobacterial diversity of Iles Eparses (Scattered Islands) in the Mozambique Channel. Acta Oecologica 72, 21–32. https://doi.org/10.1016/j.actao.2015.09.004

Zubia, M., Vieira, C., Palinska, K.A., Roué, M., Gaertner, J.C., Zloch, I., Grellier, M., Golubic, S., 2019. Benthic cyanobacteria on coral reefs of Moorea Island (French Polynesia): diversity response to habitat quality. Hydrobiologia 843, 61–78. https://doi.org/10.1007/s10750-019-04029-8

Supplemental information

Principal Coordinate Analysis

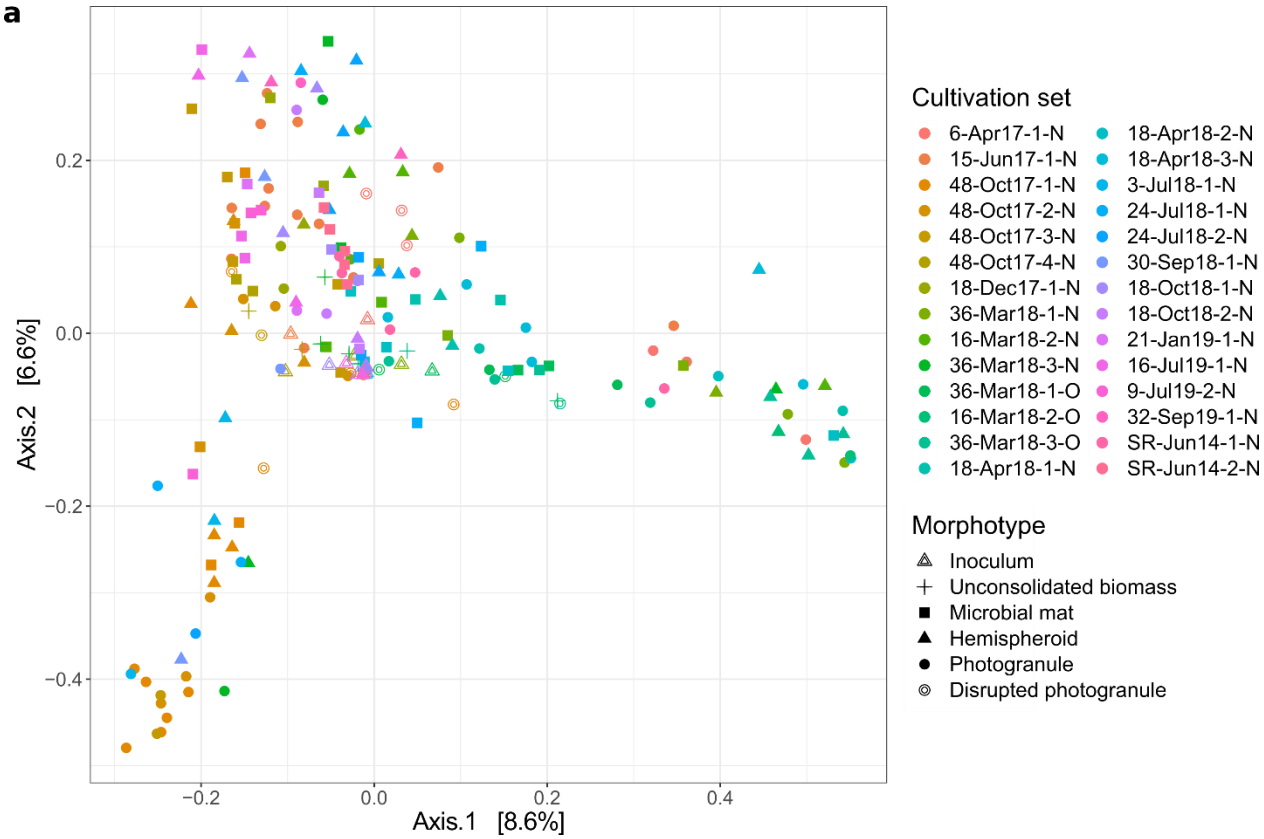

Figure S1. Principal Coordinate Analysis per microbial group. (a) Cyanobacteria. Legend applies to all panels. We coded in the names of the cultivation sets the number of repeated vials (e.g., 48), the month and year when the cultivation was started (e.g., Oct 2017), replicated cultivation sets when several were started in the same month and the sludge origin, i.e., Narbonne (N) or Ornaisons (O).

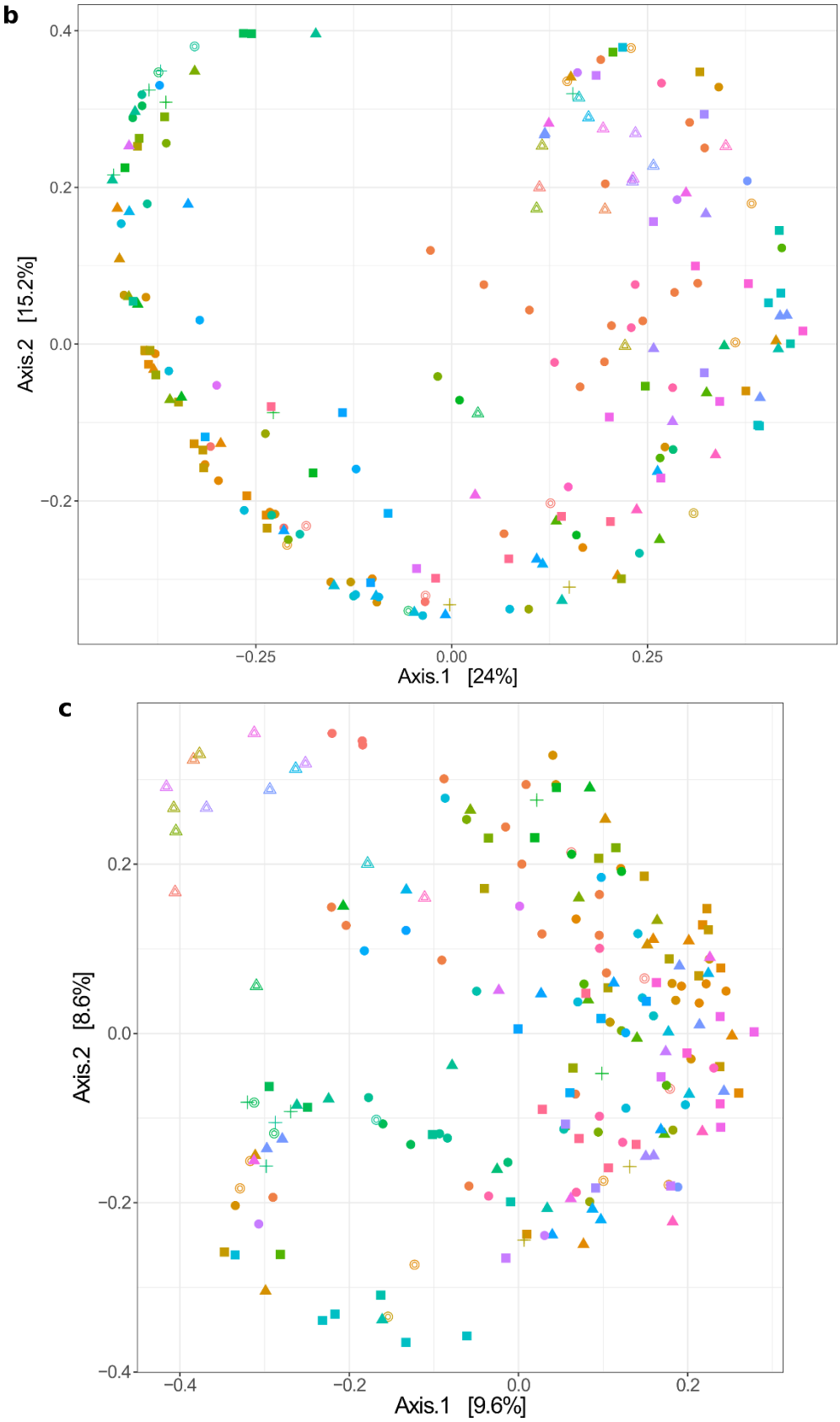

Figure S1. Continued. (b) Algae and (c) Bacteria.

Progression of photogranulation

Closed microplates and vials with fresh activated sludge were hydrostatically incubated on the document table of a desktop scanner with the scanner lid removed. We followed the transformation of activated sludge into a morphotype using high-throughput time-lapse imaging and automated image analysis (Joosten et al., 2020) (**Chapter 3**). Bioaugmentation shifted morphotype development at sufficiently large additions, but did not change the speed of contraction (**Figure S2** and **Figure S3**).

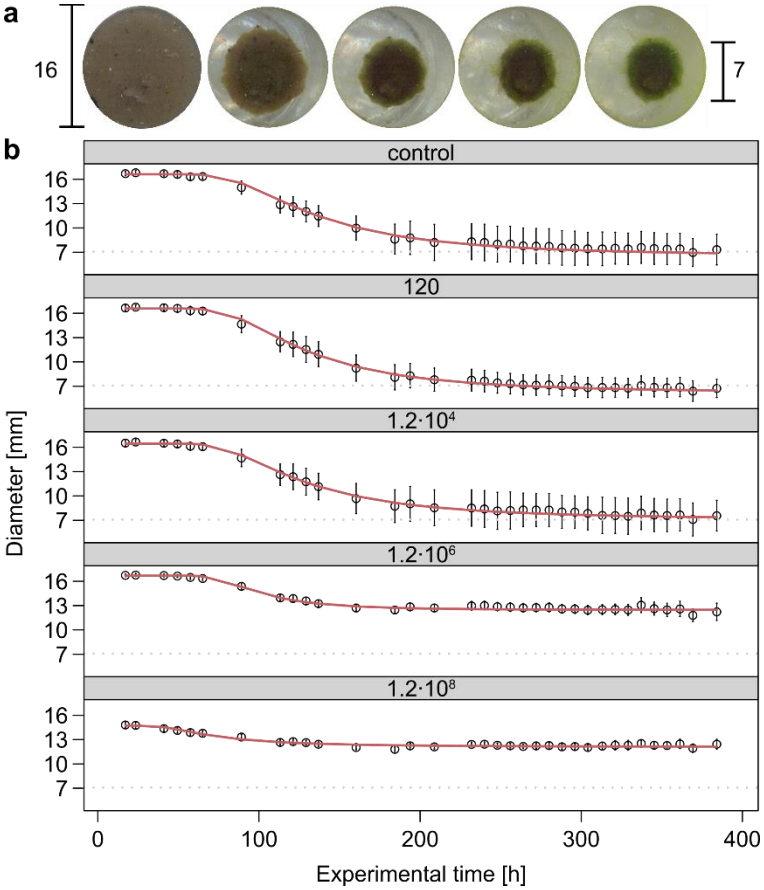

Figure S2. Progression of photogranulation of sludge 1 augmented with addition i. Photogranulation progression for the experiment in which activated sludge was augmented with homogenized outer layers of hydrostatically produced photogranules. Photogranulation is quantified as biomass contraction, i.e., the decrease in diameter over time, measured through the bottom of microplate wells according to Joosten et al. (2020). Biomass contraction is displayed as a function of the dominant *Tychonema* sequence type, expressed in 16S rRNA gene copies·mL-1 (grey boxes on top of each panel). Initially, the biomass covers the entire bottom, i.e., 16 mm. During successful photogranulation, the biomass contracts and forms an photogranule with a minimum diameter of approximately 7 mm. The biomass contracts minimally when a mat is formed (13 mm). Each graph panel represents the average of 17-20 replicates. Red lines represent Weibull distributions fitted to the data. Error bars represent standard deviations.

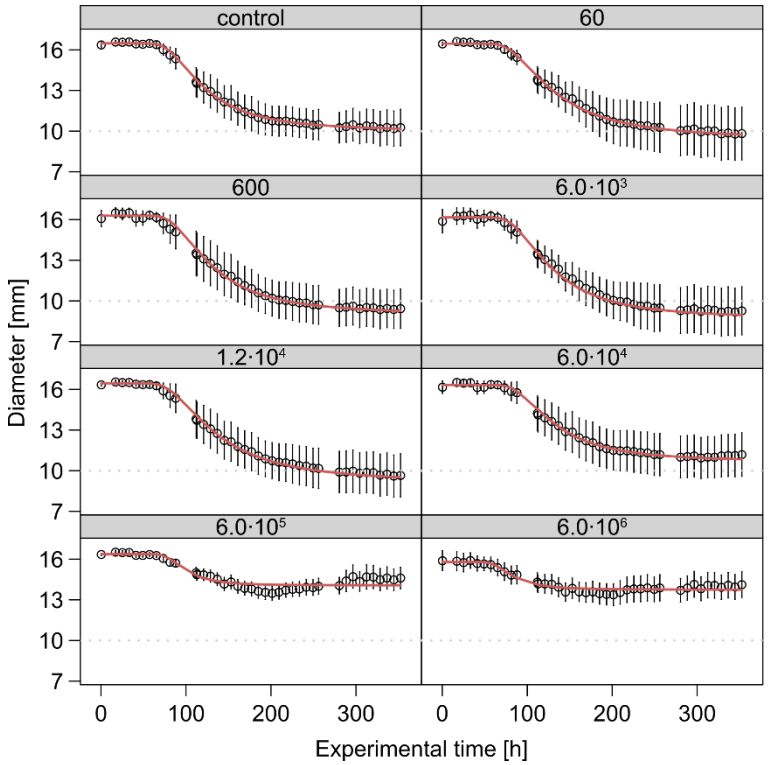

Figure S3. Progression of photogranulation of sludge 2 augmented with addition ii. Photogranulation progression for the experiment in which activated sludge was augmented with homogenized outer layers of photogranule from a bioreactor. Photogranulation is quantified as biomass contraction, i.e., the decrease in diameter over time, measured through the bottom of microplate wells according to Joosten et al. (2020). Biomass contraction is displayed as a function of the dominant *Tychonema* sequence type, expressed in 16S rRNA gene copies·mL-1 (grey boxes on top of each panel). Initially, the biomass covers the entire bottom, i.e., 16 mm. During successful photogranulation, the biomass contracts and forms an photogranule with a minimum diameter of approximately 10 mm. The biomass contracts minimally when a mat is formed (14 mm). Each graph panel represents the average of 11-12 replicates. Red lines represent Weibull distributions fitted to the data. Error bars represent standard deviations.

Description of biomass for augmentations

Photogranules for augmentations were produced **in hydrostatic batch cultivations and bioreactors** according to the procedures of Joosten et al. (2020) (**Chapter 3**) and Milferstedt et al. (2017).

Phototrophic communities

Phototrophic communities for augmentations originated from homogenization of the manually separated and pooled outer layers of **hydrostatically produced** photogranules (addition **i**), photogranules from a **bioreactor** (addition **ii**) and a **hydrostatically produced** photogranule after augmentation with the culture collection strain SAG 1459-3 (addition **ix**). Addition **iii** originated from direct homogenization of entire photogranules from a **bioreactor**.

The dominant cyanobacterium in the phototrophic communities was a *Tychonema bourrellyi* CCAP 1459/11B sequence type based on the 23S rRNA gene amplicon sequences (additions **i**, **ii**, **ix**: identical sequence type in all three additions). The dominant cyanobacterium in addition (**iii**) could not be classified based on its 23S rRNA gene amplicon sequence. It is affiliated with *Pantanalinema rosaneae* CENA 516 based on its 16S rRNA gene amplicon sequence.

Xenic cyanobacterial strains

Xenic cyanobacterial strains for augmentations were ordered from a culture collection, i.e., strain *Oscillatoria lutea* SAG 1459-3 (addition **iv**), or isolated from different mature photogranules (additions **v**-**viii**). Single cyanobacterial filaments were isolated from (a) **hydrostatically produced photogranules** by direct selection from a piece of the biomass dissolved in a water droplet (additions **v**-**vi**); (b) **photogranules from a bioreactor** by selection from a medium-solid agar plate after filaments had separated from the biomass by photomovement (additions **vii**-**viii**) (Rippka, 1988). Hydrostatically produced photogranules resulted from the transformation of activated sludge in closed 24-well microplates or 10 ml vials that were hydrostatically incubated under constant LED or incandescent light illumination (60 $\mu mol \cdot m^{2} \cdot s^{-1}$). Photogranules from a bioreactor were produced in a sequencing batch photobioreactor (Ouazaite et al., 2021) or continuously stirred tank reactor (Safitri et al., 2021).

The cyanobacterial strain in addition **v** was identified as unclassified *Phormidiaceae* based on its 23S rRNA gene amplicon sequence, and as *Kamptonema formosum* PCC 6407 based on its 16S rRNA gene amplicon sequence. We call this strain the *Kamptonema*-like strain. The cyanobacterial strains in additions **vi** and **vii** were identified as *Planktothrix agardhii* NIVA CYA 15 and *Nodosilinea nodulosa* PCC 7104 based on their respective 16S and 23S rRNA gene amplicon sequences. We therefore call them, respectively, *Planktothrix*- and *Nodosilinea*-like strain.

It should be noted that the taxonomy of cyanobacteria is under constant revision as scientists are working towards a consensus approach (Palinska and Surosz, 2014). True taxonomic classification should therefore not be based on names given to sequences alone, but on a combination of molecular and morphological studies (Komárek, 2006).

By ImageJ analysis of microscopic images, we determined trichome cell width of the cyanobacterial strains to be consistent with the literature (**Table S2**). The cyanobacterial strain in addition **viii** could not be classified based on its 23S rRNA gene amplicon sequence. It is affiliated with *Oscillatoria* SAG 1459-8 based on its 16S rRNA gene amplicon sequence. The strain does, however, not resemble an *Oscillatoria*-like organism based on its cell width. Its trichomes were too thin (1.3-1.4±0.2 µm) compared to typical *Oscillatoria* trichomes of ~3.5 µm (Kruschel and Castenholz, 1998) (**Table S2**). We call this strain therefore the unclassified cyanobacterium strain (addition **viii**). Performing a BLAST search on the NCBI nr/nt database, the 23S rRNA gene amplicon sequence was 99% similar to a sequence from an algal bloom (Sequence ID: GQ994598.1) and from a previous photogranule experiment in our laboratory (Milferstedt et al., 2017) (Sequence ID: KY920274.1). The 16S rRNA gene amplicon sequence was identical to sequences classified as *Tildeniella torsiva* (Sequence ID: KY498229.1) and *Jaaginema geminatum* (Sequence ID: KM019979.1), which both have filament widths comparable to our unclassified cyanobacterium strain (**Table S2**).

Table S2. Filament width of cyanobacterial strains cultivated in BG-11 and Z8 medium. Filament width is determined from microscopic images by ImageJ analysis and results are compared to the literature. n.a. is not available.

Augmentation	BG-11 medium		Z8 medium		Literature
Oscillatoria lutea SAG 1459-3 (**iv**)	3.5±0.5 µm	n=49	4.0±0.3 µm	n=27	~3.5 µm (Kruschel and Castenholz, 1998)
Kamptonema-like strain (**v**)	5.2±0.6 µm	n=76	5.6±0.4 µm	n=31	2.5-5.3 µm (Strunecky et al., 2014); 3.5–5 µm (*K. okenii*) (Shiels et al., 2019)
Planktothrix-like strain (**vi**)	4.8±0.6 µm	n=21	5.6±0.4 µm	n=17	2.3-9.8 µm (*P. agardhii*) (Komárek and Komárkova, 2004)
Nodosilinea-like strain (**vii**)	1.1±0.2 µm	n=91	1.6±0.3 µm	n=7	1.2-2.4 µm (*N. nodulosa*) (Radzi et al., 2019); 1.1–1.5 µm (*N. nodulosa*) (Brito et al., 2017)
Unclassified cyanobacterium strain (**viii**)	1.3±0.2 µm	n=40	1.4±0.2 µm	n=14	1.4-1.9 µm *Tildeniella torsiva* (Mai et al., 2018); 2.3–3.3 µm *Jaaginema geminatum* (Gupta, 2017)
Tychonema-like strain (**ix**)	5.2±0.6 µm	n=165	n.a.	n.a.	6.5-8 µm (*T. decoloratum*) (Shiels et al., 2019)

Filamentous cyanobacteria from photogranules from bioreactors were smaller in diameter than those from hydrostatic photogranules. In bioreactors, there are hydrodynamic forces that promote granulation, e.g., hydrodynamic shear force. In hydrostatic photogranulation, these external driving forces are absent and photogranulation results from microbial activities. Properties of cyanobacteria may therefore be more important in hydrostatic than hydrodynamic photogranulation. Larger trichome width may provide mechanical strength to encapsulate the biomass, or may provide better protection against high light conditions.

Abundant bacteria in final communities

As in **Chapter 4**, most abundant bacterial sequence types in the final morphotypes were affiliated with: *Luteimonas* detected in 49 of 68 final morphotypes at an average abundance of 5.2%±6.4, *Hydrogenophaga* in 39 of 68 samples at 3.5%±3.1% and *Gemmatimonadaceae* in 36 of 68 samples at 2.4%±2.1%. BLAST searches did not result in better taxonomic identifications.

Proportion of morphotype-forming cyanobacterial strains in initial and final communities

We investigated how mat-, hemispheroid-, and photogranule-forming cyanobacterial strains were represented in the final communities of the final morphotypes that resulted from the transformation of untreated sludge and sludge augmented with phototrophic communities or cyanobacterial strains (**Figure S4**).

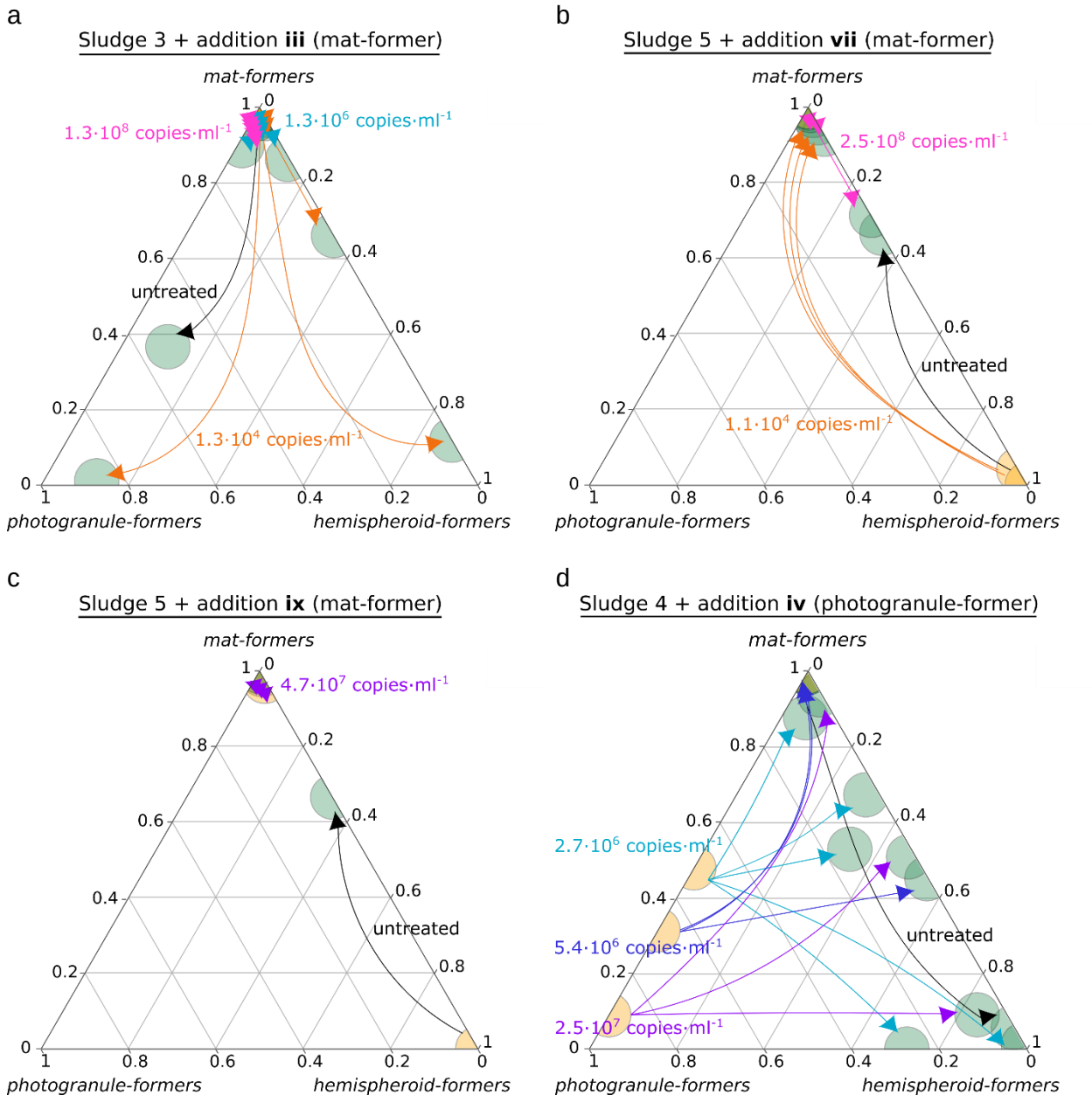

Figure S4. Change in proportion of mat-, hemispheroid- and photogranule-formers from the inoculum to the final morphotype communities. (a) sludge 3 augmented with addition **iii**, (b) sludge 5 with addition **vii**, (c) sludge 5 with addition **ix**, (d) sludge 4 with addition **iv**, and (e) sludge 5 augmented with addition **iv**. Results are based on 23S rRNA gene amplicon sequencing and cyanobacterial qPCR. Initial activated sludge is shown in orange and final morphotypes in green. Untreated control is represented by a black arrow. Increasing cyanobacterial additions are indicated by colored arrows. We used the same color for replicates on the same image (n=5 for sludge 3; n=3-5 for sludge 4; n=2-3 for sludge 5) and for additions with the same order of magnitude between images.

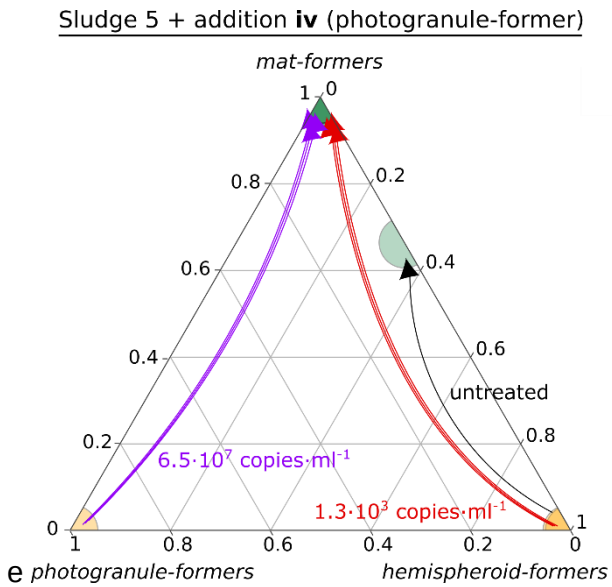

Figure S4. Continued.

Growth of cyanobacterial strains in culture medium

We cultivated the cyanobacterial strains on BG-11 and Z8 medium and measured their dry weight after three months to assess how well they grow on the culture media (**Table S3**).

Table S3. Dry weight of cyanobacterial strains cultivated in BG-11 or Z8 medium over 82 days.

	Dry weight (g) BG-11	**Dry weight (g) Z8**
Planktothrix-like strain	0.027±0.014	0.008±0.001
Kamptonema-like strain	0.006±0.006	0.012±0.001
Nodosilinea-like strain	0.033±0.006	0.036±0.004
Unclassified cyanobacterium strain	0.030±0.005	0.020±0.003
Oscillatoria lutea SAG 1459-3	0.054±0.008	0.046±0.057

Scientific outreach

Journal articles

Joosten, E. D., Hamelin, J., & Milferstedt, K. (2020). Simple Time-lapse Imaging for Quantifying the Hydrostatic Production of Oxygenic Photogranules. *Bio-protocol*, *10*(19), e3784-e3784.

Selected oral presentations

Esmee D. Joosten, Jérôme Hamelin, Kim Milferstedt (2018) Cyanobacterial abundance drives photogranulation, *International Water Association Biofilms: Granular Sludge Conference*, Delft, the Netherlands

Esmee D. Joosten, Jérôme Hamelin, Kim Milferstedt (2019) Naturally occurring cyanobacteria can form oxygenic photogranules to treat wastewater, *11th International Conference on Toxic Cyanobacteria*, Cracow, Poland

Flash poster presentations

Esmee D. Joosten, Jérôme Hamelin, Kim Milferstedt (2018) Exploring minimal conditions allowing photogranulation, *International workshop: Bridging theory and practice in ecological engineering*, Narbonne, France

Esmee D. Joosten, Jérôme Hamelin, Kim Milferstedt (2018) Relationship between microbial community and photogranulation*, Journée filière APAB ED GAIA*, Montpellier, France

Wikipedia

Hicham Ouazaite and I created the Wikipedia page on oxygenic photogranules: en.wikipedia.org/wiki/Oxygenic_photogranules